$B_s \rightarrow D_s^+ D_s^-$ decays at LHCb.

Thesis submitted in accordance with the requirements of
the University of Liverpool for the degree of Doctor in Philosophy

by

James Mylroie-Smith

September 2011

for Nick

Away seeking giants

On one last great adventure

Abstract

Collisions of two proton beams, with energies of 3.5 TeV each, from the LHC have been reconstructed using the LHCb detector. A total integrated luminosity of (36.5±3.7)pb^{-1} was used to study of the branching fraction of the decay $B_s \rightarrow D_s^+ D_s^-$ giving a value of (7.8±2.3(stat.)±3.2(syst.))×10^{-3}. Measurements of the branching ratios of $B_s \rightarrow D_s^* D_s$ were also made and found to be (7.9±3.2(stat.)±4.7(syst.))×10^{-3}. Additionally this measurement was made for $B_s \rightarrow D_s^* D_s^*$ and found to be (28±14(stat.)±15(syst.))×10^{-3}. $\Delta\Gamma_s/\Gamma_s$ was measured to be (8.1±2.5(stat.)± 3.4(syst.))×10^{-2} and is in agreement with current results. Studies of the performance of the vertex detector have also been presented.

Declaration

This dissertation is the result of my own work, except where explicit reference is made to the work of others, and has not been submitted for another qualification to this or any other university. This dissertation does not exceed the word limit for the respective Degree Committee.

Acknowledgements

First and foremost I wish to thank my supervisor, Dr. David Hutchcroft. He has been supportive in helping and guiding me during writing up of this thesis. In particular, helping me understanding bugs in my code, and problems I had with my analysis. His fast responses when editing this thesis, was greatly appreciated. Secondly, I would like to thank Professor Themis Bowcock for the great experience I had working at CERN.

My colleagues at CERN, Kurt Rinnert and Karol Hennessey, thank you for your time helping me with problems I had with work, for the many great dinners at Restaurant 11B and coffee breaks, where various interesting discussions took place. My experience at CERN would have been incomplete without you both. For my fellow PhD students, Abdi Noor, thank you for your help in getting me integrated with life at CERN and later back in Liverpool after all the fun we had in Geneva. All those welcome breaks from writing up my thesis, were often very much needed. To Emma Hicks for all the home-baked cakes and providing a delicious form of social elements to an otherwise empty office.

Last but not least, Torkjell Huse, thank you for the regular coffee breaks back in Liverpool which also helped to lighten the difficulty of writing up my thesis.

I would like to give special thanks to my family who have been there for me over the years. Especially Sylvia for the time she spent proof reading my final draft. To Judith, Jonathan, Michael, Ellen, Bryony, Jon, Josh and Aishah your support and encouragement has made the load much lighter, Thank you.

Contents

List of Figures

List of Tables

Chapter 1

Introduction

High energy physics (HEP) is the study of the fundamental laws of the universe. The standard model, which describes the way that fundamental forces and particles interact, has been exceptionally successful. It has successfully described most fundamental particles and is able to predict the existence of W^+, W^- and Z^0 bosons, which are responsible for the mediation of the weak force. A relation between the masses is also predicted from this model and has been measured successfully [5, 6, 7, 8, 9]. Over the years particle physics experiments have continued to test the standard model using cutting edge machines which have collided different particle types together. The large electron and positron collider (LEP) at CERN collided electrons and positrons together at energies up to 209 GeV until the year 2000. Using these collisions it was possible precisely to measure the properties of the W and Z bosons and infer information about the number of generations of leptons that exist.

To supplement the physics studies made at LEP, additional experiments were

also required. One such was HERA, which collided electrons or positrons with protons and was used better to understand the parton distribution and gluon interactions inside the proton.

Other experiments were BaBar and Belle, which used $e^+ - e^-$ collisions to understand the decay of B mesons and which gave precise measurements of parts of the CKM matrix. BaBar and Belle made the first observation of CP-violation in the neutral B-mesons system [10, 11].

The other large particle physics collider operating at this time was the Tevatron. That collider used protons and anti-protons at energies up to 1.96 TeV. Performing precision physics at hadron colliders is challenging, because of the composite nature of the colliding particles.

The Large Hadron Collider (LHC) [12], based in Geneva, Switzerland, has been designed to test the standard model and search for the Higgs boson. The LHC is designed to collide two beams of protons with centre-of-mass energies of up to 14 TeV. There are four major experiments at the LHC which use these collisions to search for new physics. There are two general purpose detectors, ATLAS and CMS, with the main goal of finding the Higgs boson and searching for beyond standard model physics. The other two experiments are designed to look at specific areas of physics which. These experiments are ALICE and LHCb. They look at quark-gluon plasma and B-meson measurements, respectively.

This thesis uses data taken from LHCb during 2010 and is split into the following sections:

Chapter 2 discusses the LHCb experiment and the sub-detectors used to analyse decays from collisions in the LHC;

Chapter 3 discusses the theoretical structure used in particle physics to describe observed particles and their interactions. It then goes on to discuss the theory involved in describing the properties of B mesons and their decays;

Chapter 4 describes the VELO sub-detector in greater detail and discusses the way that energy is deposited in the silicon sensors. It also considers how the simulation of this process has changed and the effect that this has on the shape of the energy deposition peak. Signal changes relative to the position of the sensor in relation to the interaction point and also as a function of radial position ,is also discussed. Noise in the sensors is also considered, as well as plots of the signal-to-noise for different parts of sensors;

Chapter 5 focuses on the decay of $B_s^0 \rightarrow D_s^+ D_s^-$, looking at the selection used, backgrounds, Monte Carlo and data comparisons and goes on to estimate systematic errors from the MC and the fit procedure. This is all combined to measure the branching ratio of the decay and the additional decays which involve $D_s^{*\pm}$ particles. The branching ratio is then used to measure $\Delta\Gamma_s/\Gamma_s$ and is compared to current results.

Chapter 2

LHCb Detector

2.1 Introduction

This chapter discusses the Large Hadron Collider (LHC) and Large Hadron Collider beauty (LHCb) detector. LHCb is one of four large experiments which uses the LHC beams to probe new physics. It is a single arm forward spectrometer designed to measure precisely the properties of the b hadrons. This chapter describes the key components of the detector and explains the importance of these in understanding b mesons.

2.2 The LHC

The LHC [12] is the world's most powerful particle accelerator and is located at CERN on the outskirts of Geneva, Switzerland. It is constructed in a 27 km tunnel

which was the former site of the Large Electron Positron (LEP) collider. When fully operational it will accelerate 2802 bunches of 1.15×10^{11} protons to 7 TeV. The LHC uses superconducting magnets to circulate two beams of protons in opposite directions. There are four points where these beams are brought together and collide. At each of these points are detectors designed to look at physics in this higher energy range. There are two general purpose detectors ATLAS and CMS. These are designed to look for new physics decaying in any direction from the proton-proton collisions. Each detector provides independent confirmation of any discoveries the made by other. The third detector ALICE, is specifically designed to look at special runs of the LHC when Lead ions are circulated. LHCb is the fourth detector and has the specific aim of looking at the b meson decays. This will be discussed further in Section 2.3.

In order to perform the precision physics that LHCb aims to do, one interaction per bunch crossing is preferred, but not required. Pile-up interactions create additional tracks and vertices which can cause fake signals. Additional tracks also add to the bandwidth consumed by the trigger system. Higher luminosities increase the radiation damage to the detectors and reduce the lifetime of the its components.

LHCb runs with operating conditions with a ~30% chance of one and only one collision in a crossing. Figure 2.1 shows the probability of zero or one or more than one collision as a function of luminosity. It shows that, for the maximum probability of one and only one collision, there is also a ~ 25% chance of more than one collision.

Difficulties during the start-up of the LHC, in September 2009, meant that, when restarting in 2010, a lower energy beam had to be used. This ran at $\sqrt{s}$ =

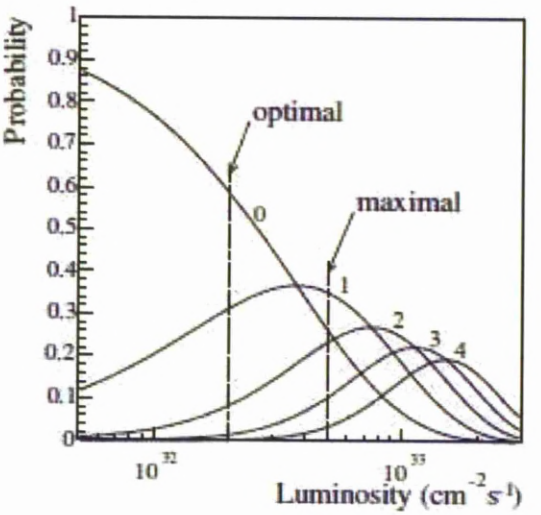

Figure 2.1: The probability of a number of collisions per event at the LHC, as a function of luminosity [1].

7 TeV in 2010, with only a limited number of bunches. Over the course of 2010 and 2011 the number of bunches increased to over 1000 in each direction and the LHC delivered ~36 pb^{-1} to LHCb in 2010. Using a larger number of bunches during 2011, more than 1 fb^{-1} was recorded at LHCb.

2.3 LHCb

The main goal of LHCb is to perform precision measurements of b mesons. Any differences found at higher energy regimes can provide a window into possible new physics. To achieve this, the detector is required to provide high track recon-

struction efficiency, good π-K separation to ~100 GeV/c, a very good proper time resolution ~40 fs and high trigger efficiencies for both leptons and hadrons [4].

Simulations using the PYTHIA[13] Monte Carlo package, show an enhanced production of $b\bar{b}$ pairs in the forward and backwards directions, coming from the momentum difference of the colliding partons. There is a boost in the direction of the parton with the highest momentum. This can be seen in Figure 2.2.

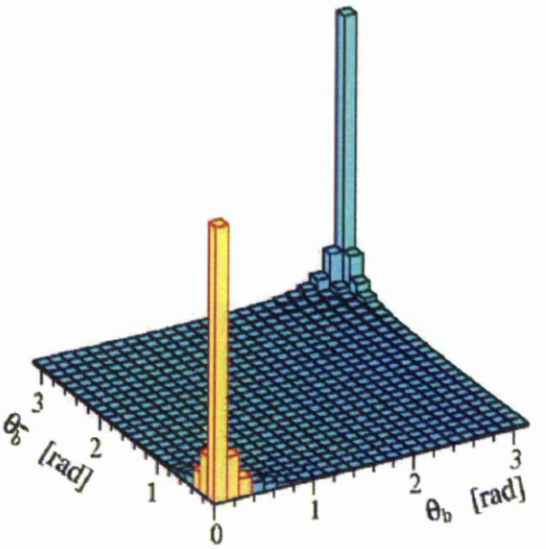

Figure 2.2: Correlation of polar angles between $b\bar{b}$ quarks at $\sqrt{s} = 14$ TeV. The yellow highlights the LHCb acceptance [2].

The production of $b\bar{b}$ pairs from proton-proton collisions can occur in several ways. Figure 2.3 shows some of the allowed production diagrams. The primary production mechanism is gluon-gluon fusion, where the colliding protons create two gluons which interact to create a $b\bar{b}$ pair. Quark anti-quark annihilation is also possible as are higher order processes, such as flavour excitation and gluon splitting, examples of which can be seen in figure 2.4.

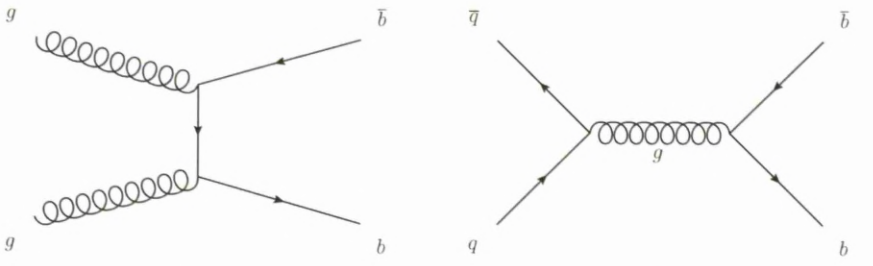

Figure 2.3: Leading order Feynman processes for $b\bar{b}$ production, showing possible gluon fusion (a) and pair creation from $q\bar{q}$ (b).

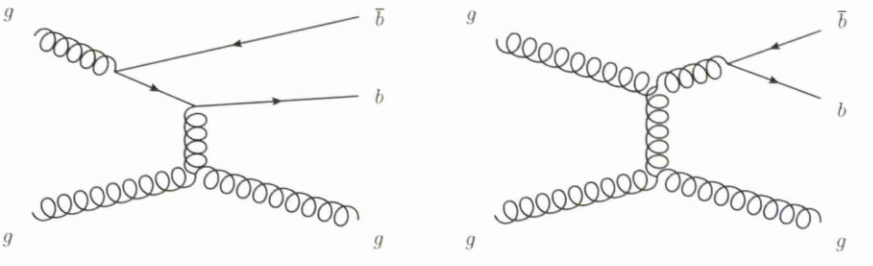

Figure 2.4: Next to leading order Feynman processes for $b\bar{b}$ production. Examples of flavour excitation (a) and gluon splitting (b) are shown.

Due to the higher order contributions, and their non-negligible contributions, theoretical predictions for the $b\bar{b}$ production cross-section have a larger uncertainty (~10%) [14, 15].

LHCb has been designed to exploit this angular effect and can reconstruct more b mesons than ATLAS and CMS. The LHCb detector has coverage in the forward direction, going from 10–300 mrad in the horizontal to 10–250 mrad in the vertical. The LHCb coordinate system is defined, starting with the origin at the interaction point and with z continuing along the direction of the beam line towards the majority of the detector. The y axis is vertical and the x axis is horizontal. In

figure 2.5 the interaction point is on the left and positive z goes from left to right, which is also referred to as downstream in the detector.

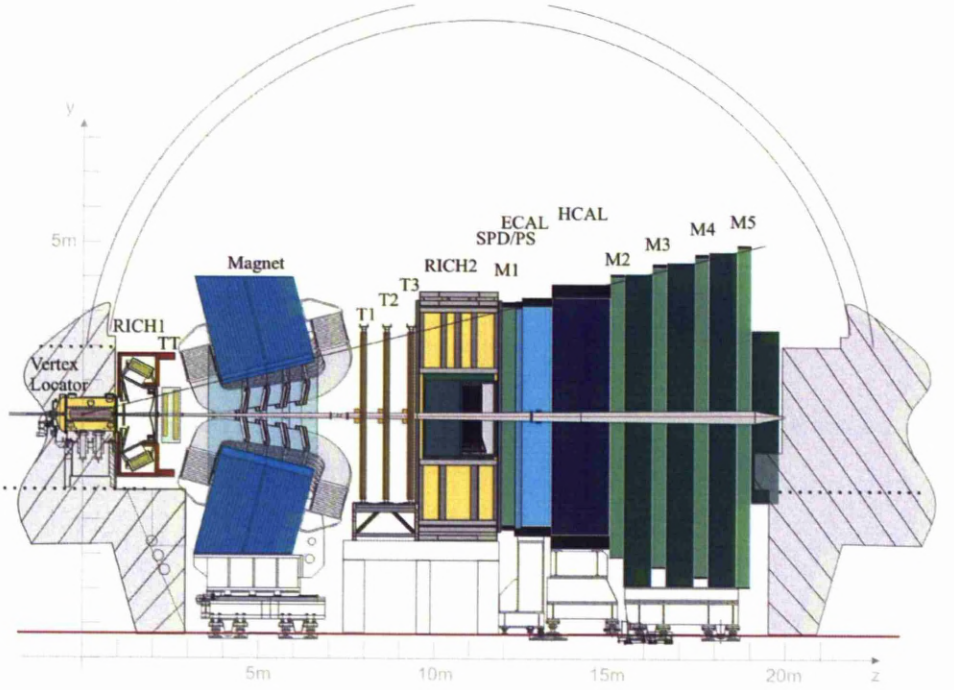

Figure 2.5: The layout of the LHCb detector in the y-z plane [4].

The LHCb sub-detectors can be split into two main categories, those for Tracking and those for Particle Identification (PID):

- **Tracking and Vertexing**; good tracking near the interaction region and good vertexing with the ability to separate between primary and secondary verities of long lived particles, is provided by the Vertex Locator. The Silicon Tracker and Outer Tracker provide efficient tracking and precise momentum measurements for charged particles.

- **PID system**; PID is crucial to the operation of B experiments and the separation of K and π mesons is key [4]. In LHCb this is performed by two

Cherenkov detectors (RICH1 and RICH2), each covering complementary momentum ranges. The electromagnetic calorimeter, hadronic calorimeter, pre-shower detector, scintillator pad detector and muon detector, provide detection and separation of e, γ, hadrons and muons.

2.4 Tracking system

The tracking system provides precise reconstruction of the primary and secondary vertices and momentum information for particles. This is done by a group of subsystems in LHCb, Vertex Locator (VELO), Tracker Turicensis (TT) and three tracking stations (T1, T2 and T3). An overview of the whole LHCb detector can be seen in Figure 2.5 and shows their respective positions, and sizes. The TT and T1 are separated by a distance of about 5 m. In this space there is a magnet to provide bending of charged tracks and give momentum measurements.

2.4.1 VELO (Vertex Locator)

The VELO is a silicon micro-strip detector, consisting of 23 planes perpendicular to the beam. Each plane has two stations on each side of the beam with each station having two silicon sensors. The two most upstream planes are solely used by L0 as part of the pile-up veto. Their purpose is to identify collisions with multiple interactions, as these contain complex backgrounds, making precision measurements difficult. The remaining planes are used for tracking and vertexing.

The VELO is positioned around the interaction point and has a first active region at a radius of 8.2 mm. To survive the harsh radiation environment close to

the beam, all but one of the VELO modules has been constructed using n-in-n type silicon. The remaining module is constructed using n-in-p type silicon, which is expected to be more radiation hard and is used for radiation damage studies. The VELO is discussed in further detail in Chapter 4.

2.4.2 Silicon Tracker

The silicon tracker makes up the next part of LHCb's tracking system. It comprises two separate parts the tracker turicensis (TT) and the inner tracker (IT). These two sub-detectors both comprise silicon micro-strip detectors and provide precision measurements of the momentum of the traversing particles. Each silicon tracker station consists of four layers, are arranged in a (x,u,v,x) configuration. The x stations are aligned with strips in a vertical position. The u and v stations have a +5° and -5° rotation, with respect to the vertical y-axis.

Tracker Turicensis (TT)

Formerly called the Trigger Tracker, this tracking detector is located between RICH1 and the magnet. The TT is 150 cm wide and 130 cm high. It covers the entire acceptance region of LHCb. It consists of silicon sensors with dimensions of 9.44 cm (length), 9.64 cm (width) and a thickness of 500 μm. Each sensor has 512 readout strips with a pitch of 183 μm. These provide a single hit resolution of close to 50 μm [16, 17]. There are four layers in the TT. These can be again subdivided into two pairs, separated by 27 cm in the beam axis(z), with configurations (x,u) and (v,x), where u and v denote the stereo angles specified earlier.

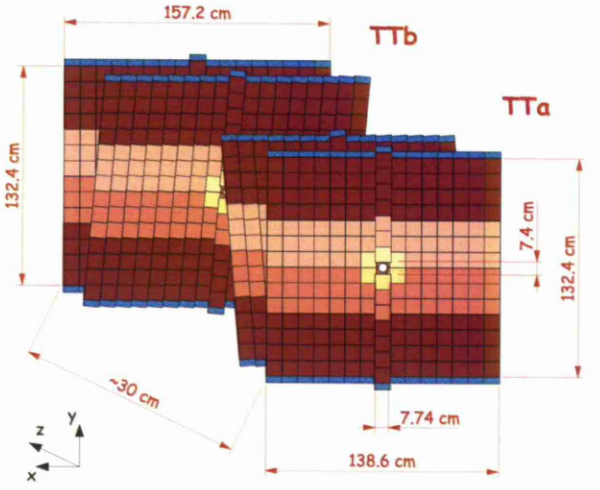

Figure 2.6: The Tracker Turicensis detector layout showing layers with different stereo angles [17].

The TT is made up of modules consisting of 7 sensors readout at their ends. There are either two or three readout sectors, as indicated by the shading in Figure 2.6. The modules with sensors closest to the beam and therefore with the highest occupancy, use three readout lines.

Inner Tracker (IT)

The inner tracker is a silicon strip detector which occupies the central region of the tracking stations T1-T3. The IT combines layers of 7 modules. Figure (2.7) shows two examples of the IT, one with its x alignment and the other in a u alignment with a +5° offset. For each T station there are four planes of IT, aligned with the same (x,u,v,x) configuration as the TT.

A module can consist of one or two sensors with a thickness of 320 μm or 410 μm respectively. These thicknesses were chosen to provide sufficient signal-

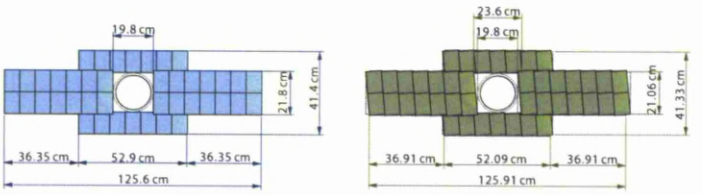

(a) In the x alignment (b) With a stereo angle of +5°

Figure 2.7: The Inner tracker detector layout [4].

to-noise ratios for each module type. Each sensor has 384 readout strips with a pitch of 198 μm. The two sensor modules are located either side of the beam pipe, while the single sensor modules are located above and below the beam pipe. Four layers overlap by 3 mm in x to prevent gaps in the acceptance.

2.4.3 Outer Tracker (OT)

The outer tracker is the final part of the tracking system and is composed of multi-wire proportional gas chambers. These are mounted on the same T stations as the IT and have the same angular configuration of (x,u,v,x) in each station. Each plane consists of two staggered 'monolayers' of straws with a 5 mm diameter. Figure 2.8(b) shows the configuration of the cells. The OT is designed to reconstruct tracks efficiently, with momentum's between 2 and 100 GeV and to give precise measurements of the momentum, with a resolution better than 0.5 %. This translates to a spatial resolution of ≥ 200 μm [18].

The chambers use a gas mixture aimed to give both high efficiency and a short drift time, whilst also keeping ageing effects to a minimum. The gas mixture chosen is Argon (70 %) and CO_2 (30 %). A voltage of ~1600V is applied to the cathode wires. This gas mixture was shown to have a maximum drift time of 42 ns

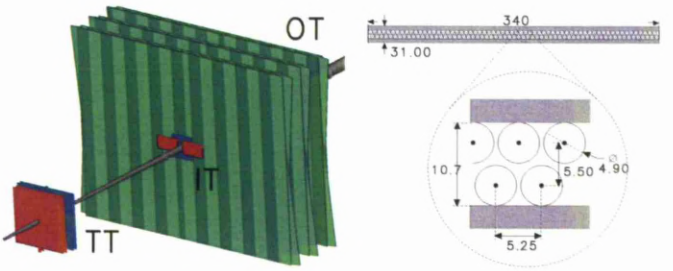

(a) (b)

Figure 2.8: The Outer tracker detector layout. a) The TT, IT and OT together around the beam line. The stereo angle of the layers in each can be seen. b) Close up view showing the cells that make OT. Distances are in mm [18].

in testbeam measurements [18].

2.4.4 Magnet

LHCb contains a warm dipole magnet which curves charged particle trajectories to allow precise momentum reconstruction. The LHCb magnet design was constrained by the requirement that tracks of 10 m length experienced an integrated field of 4 Tm. This field needed to be applied without exposing the RICH to a field greater than 2 mT [4]. Figure 2.9 shows the strength of the main magnetic field component as a function of position along the z axis.

The magnet will run in two opposite polarities over the lifetime of the experiment. Changes in polarity are done regularly throughout the year. The changes in polarity are important as they help to reduce the systematic errors introduced by asymmetries in the detector and magnet. After the installation of the magnet, a detailed study of the field was conducted which showed agreement with simulation to within 1% across most of the detector region. The only area of discrepancy was in the upstream region which was found to have a 3.5% effect. This was at-

tributed to the precision of the model used and the location of the massive iron reinforcements embedded in the concrete of the hall.

2.5 Track and Vertex Reconstruction

The tracking software combines hits in the tracking stations and constructs tracks. There are five different types of tracks defined in the LHCb tracking. These are VELO, Upstream, Downstream, Long and T tracks. They can all be seen in Figure 2.9.

2.5.1 VELO Tracks

To create VELO tracks, clusters from the R and Phi sensors can be combined to create 3D space points or hits. Alternatively VELO R or Phi hits can be combined to form R or Phi tracks. These hits, consistent with a straight line, are then combined to form tracks. A minimum of three stations is required to create a track and if the track cannot be matched to any hits found in the TT or T stations, it is classed as a VELO track. VELO tracks are often out of the LHCb tracking acceptance in the forward direction, or in the backward direction. These trajectories mean particles leave no hits in the other stations. Although they have a limited use for physics, they help with primary vertex reconstruction.

2.5.2 Upstream Tracks

Upstream tracks only have hits in the VELO and the TT. They are usually tracks with low momentum, which are then bent out of the acceptance by the magnet. They have poor momentum resolution but do have some uses, such as helping to understand the background in the RICH1 particle identification algorithms. They can also help with b hadron decay reconstruction and flavour tagging.

2.5.3 Long Tracks

Long tracks traverse the whole detector and have the most precise momentum information. They can have hits in all tracking stations but this is not a strict requirement. These tracks are important in most physics' studies and are the sole track type used for the studies presented in Chapter 5. The reconstruction of these tracks is discussed in greater detail later in this section.

2.5.4 Downstream Tracks

Downstream tracks have hits in the TT and T tracking stations. It is probable that these come from decay products of longer lived particles, such as K_s^0 and Λ, which have decayed outside the acceptance of the VELO. In the case of the reconstructable K_s^0 about 25% decay inside the active region of the VELO and 50% outside. Those decaying outside the VELO can be reconstructed by using two oppositely charged downstream tracks.

2.5.5 T Track

T-Tracks only have hits in the T seeding stations. These can come from secondary interactions or low angle tracks bent into the acceptance by the magnetic field.

2.5.6 Reconstruction of Long Tracks

Long tracks have been used exclusively for the physics' studies presented in Chapter 5. Due to their importance, a full description of the reconstruction process is provided in this section. The reconstruction uses several algorithms to find these tracks.

Reconstruction begins by creating VELO seed tracks, which are constructed using VELO hits and fitting them with a straight line through three or more stations. These VELO tracks serve as seeds for the subsequent algorithms.

The forward tracking algorithm starts with the VELO tracks and, assuming no multiple scattering, combines these with the hits from the TT. It begins by extrapolating the VELO tracks forward to a z position of 8520 mm. The T tracks are also extended to the same z reference point. If there are intersecting tracks within the uncertainties, these are combined to form a long track. The tracks are refitted using the Kalman filter which adds corrections for multiple scattering and energy loss. Additional algorithms are used to make searches starting from T seed tracks.

Using the hits from the T stations which have no associated tracks, T seed tracks are made. T tracks are exposed to a magnetic field of $\sim$ 0.5 Tm. This

introduces a bend of a few centimetres over the T stations. T tracks are therefore fitted using a parabola. A matching algorithm, the reverse of the forward tracking, is then used to search for tracks which match in the VELO or TT.

The performance of the long track reconstruction has been examined and long tracks have, when looking at particles with momentum greater than 10 GeV, been found to be reconstructed with an efficiency of ~94%. These typically produce about ~9% ghost tracks. Ghost tracks are tracks which cannot be associated to any Monte Carlo particle.

The quality of tracks is measured using parameters such as χ^2, probability chi squared ($P\chi^2$) and number of degrees of freedom (n.d.f.) of the Kalman filter. These, along with some additional parameters, are combined in a neural net (NN) and are used to help distinguish between real and ghost tracks. It is possible to reduce the typical ghost rate from 18.5% to 8% with a loss of only 4% in efficiency [19]. Ghost tracks provide one of the backgrounds to the physics studies which follow in Chapter 5.

2.6 Track and Vertex Resolution

This section discusses the performance of the track and vertex reconstruction. Reconstructed tracks can be used to calculate the momentum of the particles causing them. By using the curviture of the track the momentum can be measured. Figure 2.10 shows the relative resolution($\delta p/p$) for long tracks. δp is defined as the RMS of the residual distribution between the reconstructed and true track momentum. The momentum spectrum for generic B decays is shown below.

Figure 2.10 also shows the ompact parameter resolution as a function of inverse transvers momentum. The impact parameter is the shortest distance in three dimentional space between a track and the primary vertex. It is used by the trigger to select B candidates.

From Monte Carlo simulations a primary vertex resolution of 8, 10 and 59 μm for the x, y and z directions respectively [20]. Using data taken in 2011 values of 13, 13 and 69 μm for events with one reconstructed PV were found [21].

2.7 Particle Identification System

Particle Identification is done primarily by the RICH system but information from the calorimeters is combined with this, to improve the separation for some particles.

RICH

The RICH detector is a ring imaging Cherenkov detector. Its main aim is to separate pions and kaons. It employs two separate detectors to do this. The RICH uses the principal of Cherenkov radiation, where a particle emits light when it passes through an insulator at a speed greater than the macroscopic speed of light in that medium. The angle of the emitted light is known as the Cherenkov angle (θ_c) and varies as a function of the particle's velocity. In the RICH, rings from the light are reconstructed to give the Cherenkov angle and allows separation of particles with different masses. Using the velocity(v) from the Cherenkov angle and combining with the momentum measurement, a mass can be assigned to the

particle. As v approaches the speed of light, the angle of emission is maximal and particle identification is no longer possible. The momentum range for which the separation of particles is possible, depends on the material which is used as a radiator. Figure 2.11 shows the Cherenkov angle as a function of momentum for different particle types in the three different radiators used in the RICH detectors.

The Cherenkov light emitted is reflected out of the detectors, using a combination of spherical and flat mirrors. The light is focused onto Hybrid Photon Detectors (HPDs) where the photons are converted to electrons and accelerated, under high voltage, onto a silicon pixel detector. The silicon sensors contain 1024 pixels each 500 μm $\times$ 500 μm. Measurements from the HPDs are combined and used to reconstruct rings. The radii of the rings give a measure of the Cherenkov angle. Figure 2.12 shows the reconstruction of these rings from data.

The RICH system is made up of two separate Cherenkov detectors (RICH1 and RICH2). Schematics of both can be seen in Figure 2.13. RICH1 is located between the VELO and the TT and covers the full acceptance of LHCb. It contains two radiators, aerogel and fluorobutane (C_4F_{10}), which allow it to separate kaons and pions with momentum between 1 and 60 GeV/c. RICH2 uses CF_4 and allows separation in a higher momentum range, going from about 15 GeV/c up to and beyond 100 GeV/c. RICH2 is situated downstream of the magnet and is located between the last tracking station and the first muon station.

2.7.1 Calorimeters

The four calorimeters are located between M1 and M2. These are the electromagnetic calorimeter (ECAL), the hadron calorimeter (HCAL), the preshower detec-

tor (PS) and the scintillator pad detector (SPD). All the calorimeters use two or three types of square cells separated into different regions. The PS, SPD and ECAL all share the same segmentation, which is shown in Figure 2.14(a). There are three different regions with sizes 40.4, 60.6 and 121.2 mm. The HCAL has a different segmentation having just two regions, the inner with cells of 131.3 mm and the outer with cells of 262.6 mm. This can be seen in Figure 2.14(b)

The preshower detector (PS) and the scintillator pad detector (SPD) are the calorimeter stations closest to the interaction point. They have been specifically designed to enable separation of electrons, pions and photons. Both the PS and SPS use scintillator pads which readout using wavelength shifting (WLS) fibres coupled to multi-anode photomultiplier tubes (MAPMT). The PS and SPS are highly segmented to provide good granularity in the X-Y plane.

The SPD is used to detect the passage of charged particles and the separation of electrons and photons. The PS is separated from the SPD by a 15 mm layer of lead, which creates a shower of particles. Pions deposit more energy than electrons as they pass through and this allows their separation. Figure 2.15 shows this.

After the PS, is the ECAL, followed by the HCAL. The ECAL and HCAL work in similar ways, with an absorber (lead in ECAL, iron in HCAL) creating a shower of particles, which then pass through a scintillator. The light is then collected by a photomultiplier tube and the amount of light collected is proportional to the energy of the incident particle. The ECAL collects the full shower for all electrons and photons and the HCAL absorbs the energy from all the hadrons.

The energy resolution for both the ECAL and HCAL follows the following

relationship for the ECAL [4, 22]:

$$\frac{\sigma(E)}{E} = \frac{\mathrm{a}}{\sqrt{E}} \oplus \mathrm{b} \oplus \frac{\mathrm{c}}{\mathrm{E}} \tag{2.1}$$

where E is expressed in GeV and $\oplus$ means addition in quadrature and 8.5% < a < 9.5% , b ~ 0.8% and c is the noise ~ 0.1. For the HCAL [4, 23] the resolution is:

$$\frac{\sigma(E)}{E} = \frac{(69 \pm 5)\%}{\sqrt{E}} \oplus (9 \pm 2)\% \tag{2.2}$$

Both ECAL and HCAL meet their design requirements. In the case of the ECAL this corresponds to a B mass resolution in the region of 70 MeV/c^2 which is dependent on the exact decay being reconstructed.

2.7.2 Muon Identification

The muon system is used to identify and track muons. It is required to give a momentum resolution of 20% for use in the triggers search for muons with transverse momentum (p_T) greater than 1 GeV. The muon system uses five stations of multi-wire proportional chambers (MWPC). A gas mixture of $Ar/CO_2/CF_4$(40:55:5) is used and gives a time resolution of about 5 ns. The first of these, called M1, is situated in front of the calorimeters, to reduce the effects of multiple scattering as the muon passes through the calorimeters. This is important, as the momentum is calculated by first assuming that the muon originated from the nominal interaction point and then by using the deflection, as measured by M1 and M2, to give the momentum.

Due to its positioning, the central region of M1 has a higher particle flux. To

prevent the ageing of the MWPCs in that area, Gas Electron Multipliers (GEMs) are used in the innermost region. M1-M3 are designed with greater spatial resolution in the x axis, to allow better determination of the bending, and therefore momentum, of the muons. M4 and M5 have worse spatial resolution and are used to detect the presence of particles. Between stations M2-M5 and behind M5 are 80 cm thick iron absorbers. These remove hadronic backgrounds and shield the detectors from particles that stray from the LHC beam.

The muon chambers adopt a similar structure, as seen in many of LHCb's detectors, with a greater segmentation closer to the beam. A schematic can be seen in Figure 2.16, in the case of the muon chambers different pad sizes are used at some of the stations. The stations are grouped: (M1); (M2-M3); and (M4-M5), with number of pads scaling as 2:4:1. As well as the number of pads changing, the size of the pads also changes.

2.7.3 Particle Identification Methods and Performance

The RICH detector provides most of the information used for PID in LHCb. Other detectors also contribute information to help make the best decision possible. The RICH uses a log likelihood method approach [24], to match the observed pixel hits in the RICH to those expected from reconstructed tracks. The likelihood is maximised by varying the particle hypothesis of each track in turn through electron, muon, pion, kaon, and proton. Figure 2.17 shows the efficiency for Kaon identification and of Pions identified as Kaons as a function of momentum in Monte Carlo. The efficiency is high for particles with momentums in the range ~20 to ~40 MeV/c. At high momentums the Kaon efficiency drops off as the Pion mis-id rate rises. A large improvement in the purity of the sample is made by

applying a tighter cut on the delta log likelihood.

Methods have also been developed to find rings without the use of tracks. This provides an alternative method of assessing the performance of the RICH and this is discussed further in Reference [25].

2.7.4 Trigger System

The aim of the trigger is to reduce the data written to file from the bunch crossing rate (40 MHz), to about 2 kHz, which is needed for offline storage. Two levels of trigger are used to achieve this: Level 0 (L0) and High Level Trigger (HLT).

Level 0

The Level 0 trigger uses custom electronics to make decisions on the suitability of events. The system has an inbuilt latency of 4 μs, after including time of flight of particles, cable delays and front end electronics. This leaves only 2 μs to process and make a decision [4]. It takes input from three sub detectors: Pile-Up, Calorimeters and Muon Systems. Each of these will now be discussed.

The pile-up system aims to distinguish between single and multiple interactions. It provides primary vertices candidates along the beam line and a total backward track multiplicity.

The calorimeter trigger system looks for particles with large transverse energy (E_T). It also identifies them as electron, photon or hadrons, based on information from the SPD, PS, ECAL and HCAL. The total E_T of the HCAL is used to reject

crossings without visible interactions and muons from the halo. The number of SPD cells hit is used to provide a measure of multiplicity.

The muon trigger selects the two muons with the highest p_T from each quadrant, assuming the track is from the interaction point, to estimate the momentum.

All this information is then passed to the Level 0 decision unit which combines all the information and provides a decision for all crossings.

HLT

The HLT is implemented in software, making it flexible and allowing changes to be made as the LHCb physics programme evolves. The HLT can also be subdivided into two stages, HLT1 and HLT2. Figure 2.19 shows the flow of information through the different trigger levels. HLT1 starts by taking information from the VELO and Tracking stations which correspond to the Level-0 objects. It also is able to discriminate against photons and π^0 candidates, by attempting to match charged tracks to their hits in the SPD. The reduction in rate from HLT1 gives a rate of about 30 kHz to HLT2. At this rate, these events can be fully reconstructed and further filtered, to give an output rate of about 2 kHz.

For the analysis presented in chapter 5 the decay investigated is $B_s^0 \rightarrow D_s^+ D_s^-$. At Level 0 the important trigger is the hadron alley as all decay products in the analysis are hadrons. The trigger line used in the analysis is AllB2DDLineLoose, which gives an efficiency of ~15%.

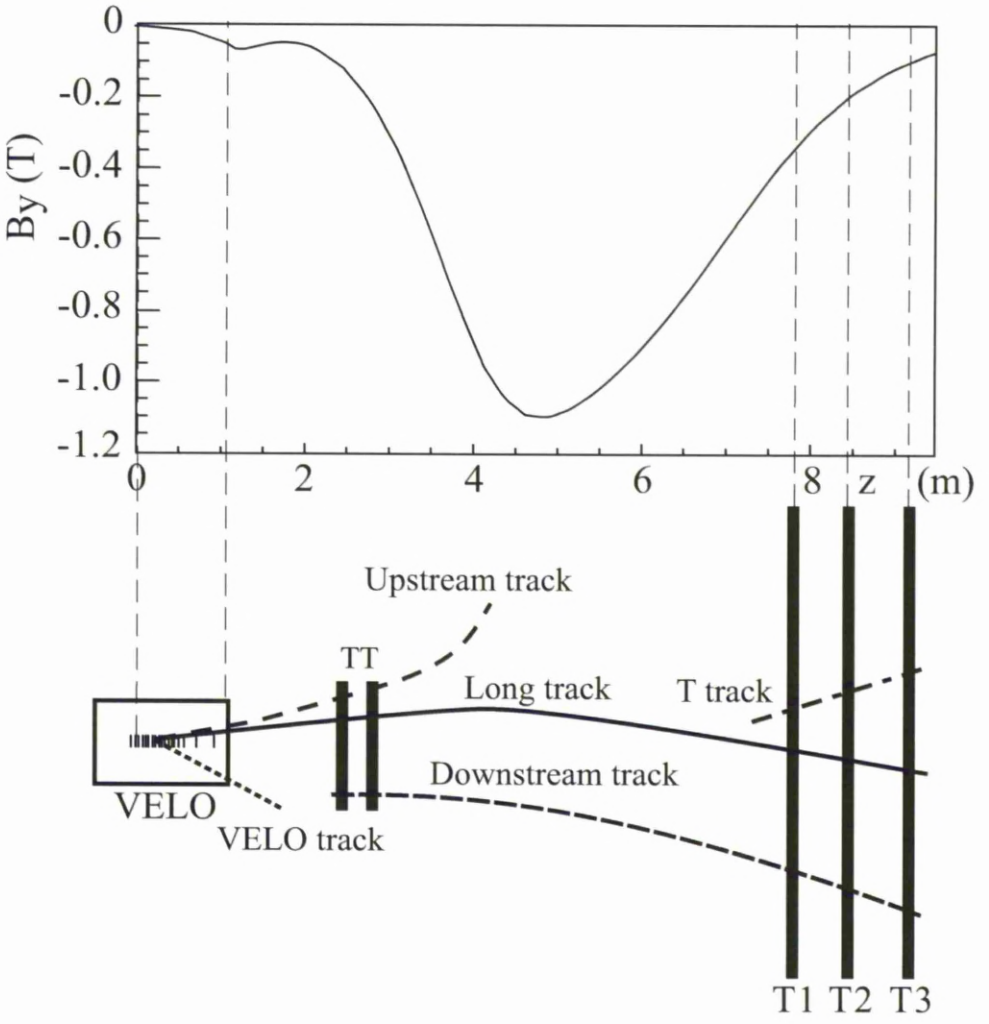

Figure 2.9: Magnet field strength as a function of z and schematic of track types [4].

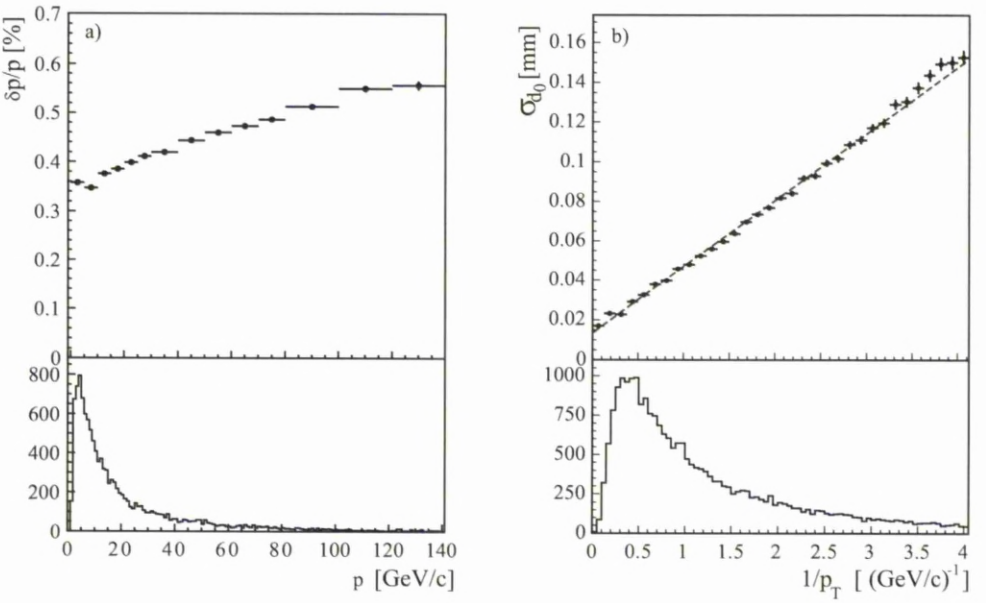

Figure 2.10: a) Relative momentum resolution of long tracks as a function of momentum from simulation. The momentum spectrum for B decays is shown below. b) Impact parameter resolution(σ_{d0} as a function of inverse transverse momentum from simulation. The dashed line shows a linear fit to the data. Below is the $1/P_t$ spectrum for B decays. [4]

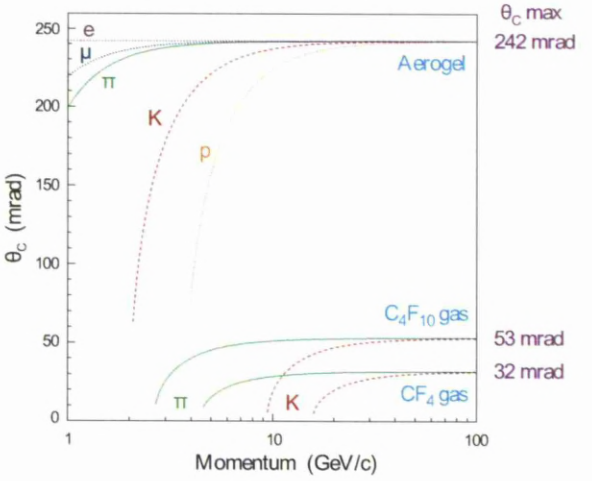

Figure 2.11: The Cherenkov angle for each of the RICH radiators used. By using a combination of the three gels a distinction between kaons and pions is possible over a larger range of momentum's [4].

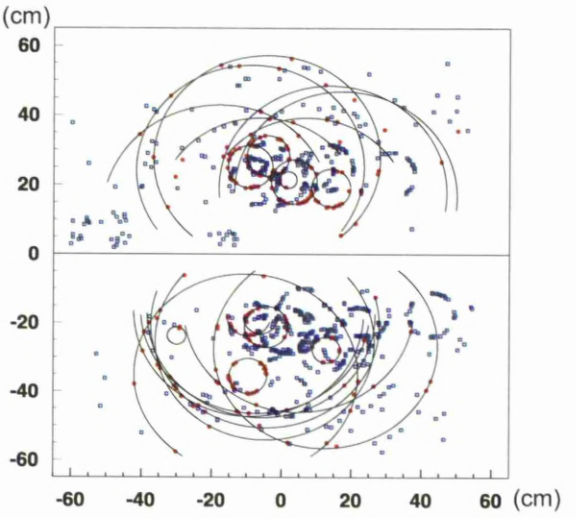

Figure 2.12: RICH1 rings reconstructed from a simulated event [4].

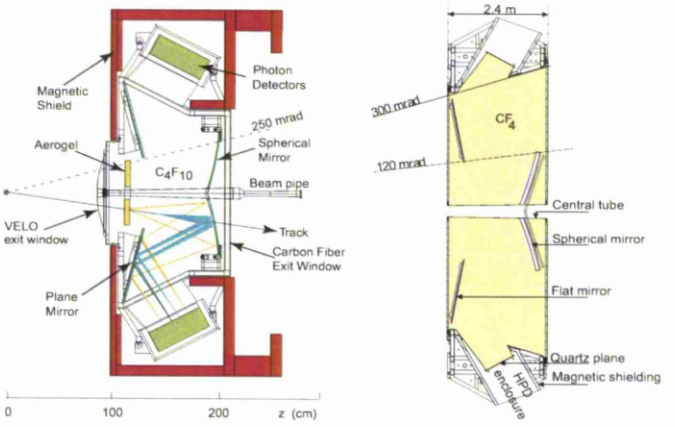

(a) (b)

Figure 2.13: Side views of the RICH detectors. a) RICH1 b) RICH2. Note the scales are different [4].

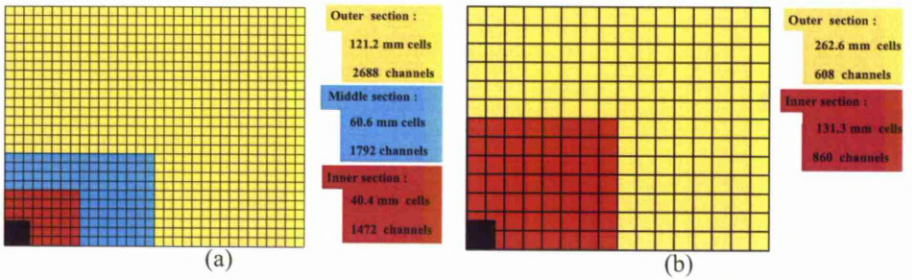

Figure 2.14: A schematic showing the segmentation of the calorimeters. a) SPD, PS and ECAL b) HCAL [4].

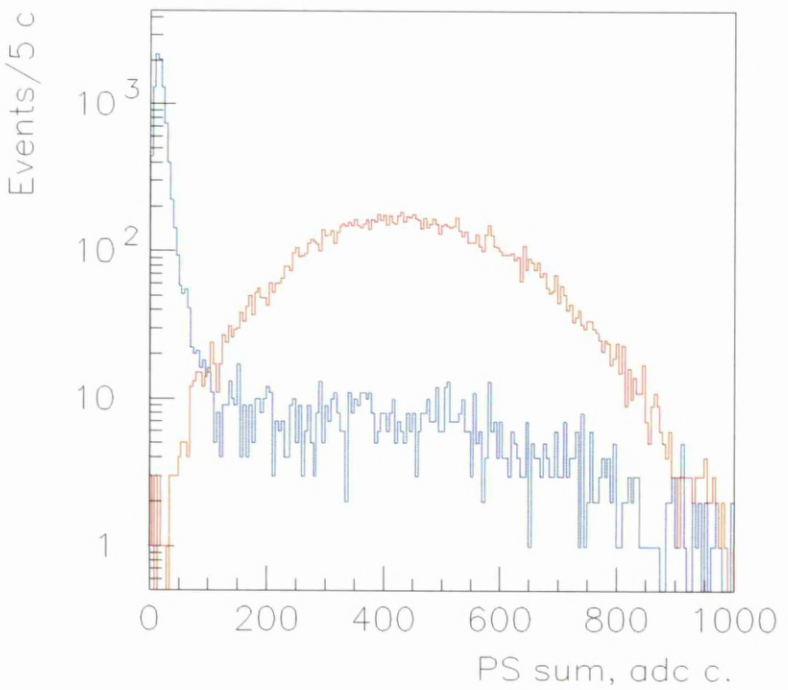

Figure 2.15: The energy deposited by 50 MeV electrons (red) and pions (blue) in the preshower detector [4].

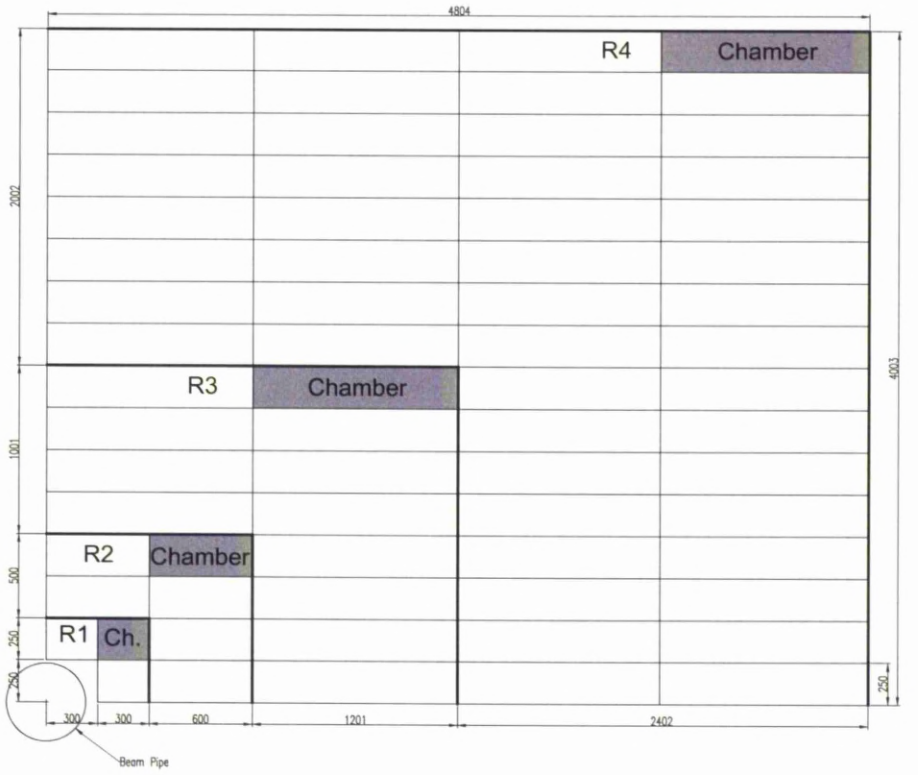

Figure 2.16: The layout of the one part of a muon chamber showing the four segmented areas. This forms a quarter of one of the muon stations with the beam line passing through the bottom left corner of this segment [4].

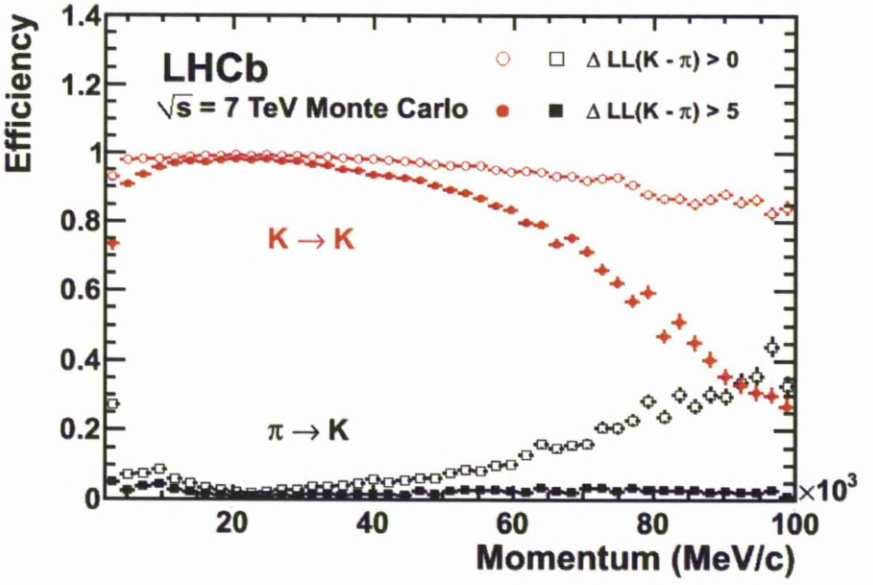

Figure 2.17: K efficiency and pion mis-id as a function of momentum from simulation. The different points show this fractions when using different constraints on the delta log likelihood.

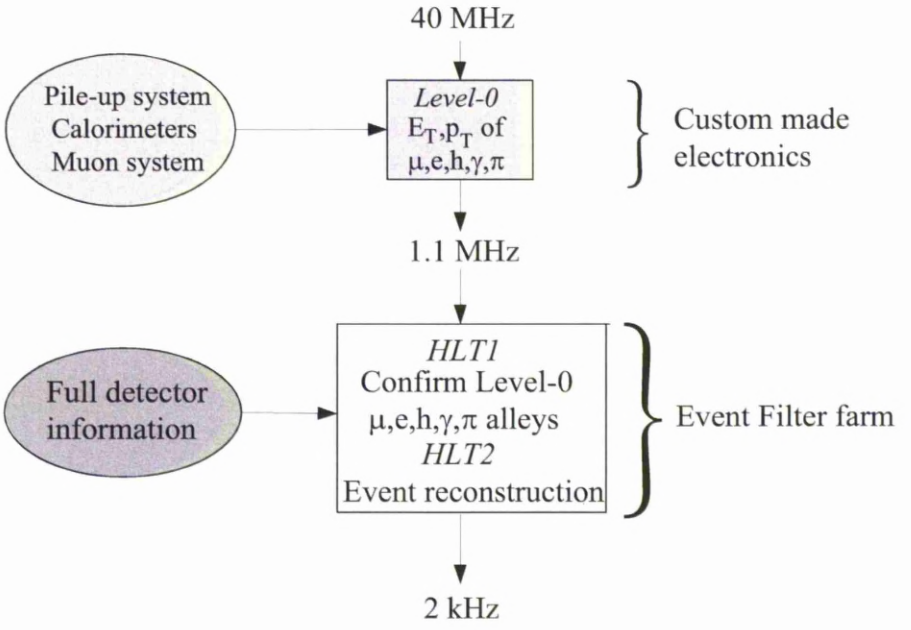

Figure 2.18: A schematic overview of the Trigger system [4].

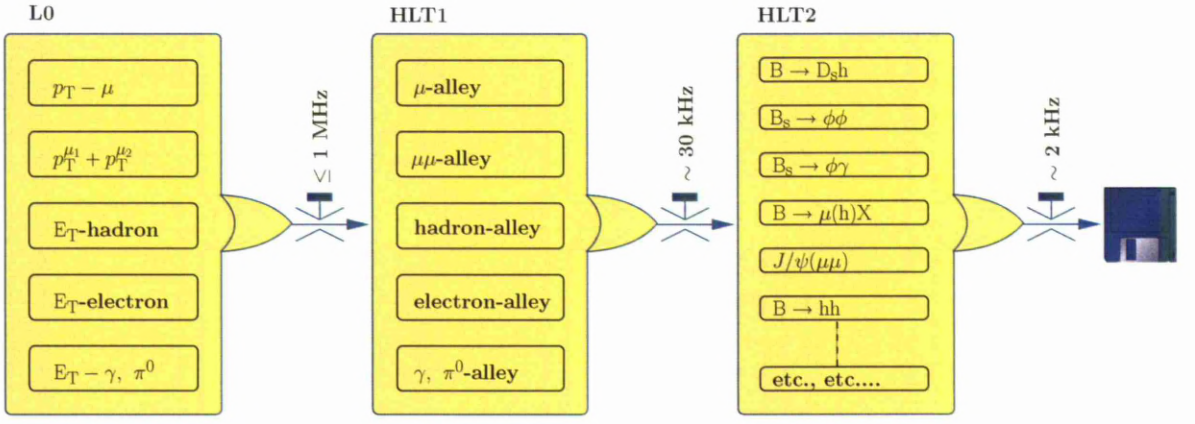

Figure 2.19: A flow diagram showing the Trigger sequences [4].

Chapter 3

Theory

Particle physics aims to explain how the fundamental constituents of matter interact with each other. Physicists have constructed a mathematical model to explain what is seen in experiment. This model is known as the Standard Model and has proved very successful in describing and predicting certain properties of the universe. This section will discuss the properties of particles in the Standard Model. It will start in general terms and then cover the formalism used to describe particles. For greater details see [26, 27, 28, 29].

3.1 Introduction

The Standard Model is used to describe particles and their interactions. It has been used very successfully in describing and predicting the properties of particles. Particles fall into two basic groups, fermions and boson based on their spin.

3.1.1 Fermions

Fermions are point-like particles with half integer spin. They can be subdivided further into leptons and quarks. There are three different flavours of leptons: electron (e), muon (μ) and tau (τ). Each of these flavours consists of a charged particle, an opposite charge anti-particle and a neutral particle antiparticle neutrino pair.

Quarks, like leptons, also have three generations which are grouped in pairs relating to their mass. Each generation has a quark with charge $+\frac{2}{3}$ and $-\frac{1}{3}$. The quarks are known as up (u), down (d), charm (c), strange (s), top (t) and bottom (b). A summary of their properties is given in Table 3.1.1.

In the Standard Model, quarks carry a colour charge which can be either red, green or blue. This colour charge provides a mechanism that prevents the observation of quarks except in pairs or triplets. The overall colour of an object is must be white, this can be obtained from a colour and anti-colour pair or from the combination of three colours or anti colours. This will be explained further in Section 3.2.2.

Fermion	Generation			Charge
	I	II	III	
Leptons	e	μ	τ	-1
	ν_e	ν_μ	ν_τ	0
Quarks	u	c	t	$+\frac{2}{3}$
	d	s	b	$-\frac{1}{3}$

Table 3.1: Fermions in the Standard Model

3.1.2 Bosons

There are four fundamental forces of nature: Electromagnetic, Weak, Strong and Gravity. Three are described by the Standard Model and are mediated by bosons. The fourth fundamental force, gravity, is still not described by the Standard Model.

Bosons are integer spin particles, which describe the mediation of electro-weak and strong forces. The electro-weak force is the combination of electromagnetic and weak forces, carried by the massless photon and the massive $W^{\pm}$ and Z^0 bosons. The strong force is carried by eight massless gluons, which also carry a colour charge.

The biggest failing of the Standard Model is that all particles are generated with no mass. The Higgs boson is a theoretical prediction, used as a way to give mass to the particle terms.

Boson	Charge	Force
Photon	0	Electromagnetic
$W^{\pm}$	± 1	Weak
Z^0	0	Weak
Gluon	0	Strong

Table 3.2: Bosons in the Standard Model

3.2 The Mathematical Framework

This section describes the way a mathematical framework has been developed to describe the particles found and the force with which they interact. It explains the theory used to describe the particle and observable effects such as CP violation.

3.2.1 Quantum Electrondynamics (QED)

QED is the quantum field theory used to describe the electromagnetic force. This comes from the Dirac equation for a free fermion field with spin $\frac{1}{2}$ and mass m. This gives:

$$L_{free} = \bar{\psi}(x)(i\gamma^{\mu}\partial_{\mu} - m)\psi(x) \tag{3.1}$$

This Lagrangian is invariant under global transformations but not under local phase transformations. To enable this to become invariant, an additional term is required to cancel the the phase term introduced with the transformation. To achieve this, a vector field term is introduced, $A_{\mu}(x)$. Under local gauge transformation it transforms to:

$$A_{\mu}(x) \rightarrow A_{\mu}(x) - \frac{1}{e}\partial_{\mu}\theta(x) \tag{3.2}$$

The propagation of this field is described by the addition of a kinetic term, $\frac{1}{4}F_{\mu\nu}F^{\mu\nu}$, which is also required not to break the invariance of the Lagrangian under gauge transformation. The field strength tensor $F_{\mu\nu}$ is given as:

$$F_{\mu\nu} \equiv \partial_{\mu}A_{\nu} - \partial_{\nu}A_{\mu} \tag{3.3}$$

By defining the covarient derivative, D_{μ} as:

$$D_{\mu} \equiv \partial_{\mu} + ieA_{\mu} \tag{3.4}$$

The resulting QED Lagrangian density is given by:

$$L = \bar{\psi}(x)(i\gamma^{\mu}D_{\mu} - m)\psi(x) - \frac{1}{4}F_{\mu\nu}F^{\mu\nu} \tag{3.5}$$

Applying a U(1) gauge transformation to equation 3.5, gives the vector field A_{μ}, which gives the propagator of the electromagnetic force, the photon.

3.2.2 Quantum Chromodynamics (QCD)

QCD is a non-abelian gauge theory that describes strong interactions. It uses a $SU(3)_c$ symmetry, giving rise to 8 massless vector fields which propagate the field. These vector fields are known as gluons and, unlike in the case of the U(1), the $SU(3)_c$ is non-Abelian. This allows the gluons to carry an additional colour charge and to couple with each other.

$$L = \sum_{f} \bar{q}_f(x)(i\gamma_{\mu}D^{\mu} - m_f)q_f(x) - \frac{1}{4}F^{a}_{\mu\nu}(x)F^{\mu\nu}_{a}(x) \tag{3.6}$$

where f is the quark flavours and the covariant derivative D^{μ} is:

$$D^{\mu} = \left(\partial_{\mu} - ig_s\left(\frac{\lambda_a}{2}\right)A_{\mu}\right) \tag{3.7}$$

with g_s the gauge coupling constant, A^{μ} the gluon fields and $\frac{\lambda_a}{2}$ the SU(3) generators. $F^{a}_{\mu\nu}(x)$ is defined as:

$$F^{a}_{\mu\nu}(x) = \partial_{\mu}A^{a}_{\nu} - \partial_{\nu}A^{a}_{\mu} - \sqrt{4\pi\alpha_s} \cdot f^{abc}A^{b}_{\mu}A^{c}_{\nu} \tag{3.8}$$

where f^{abc} is the structure function of the $SU(3)_c$ group and each of the indices run from one to eight. α_s is the strong coupling constant and is given by:

$$\alpha_s = \frac{g_s^2}{4\pi} \tag{3.9}$$

α_s is referred to as a constant but varies as a function the energy, known as the running of the coupling constant. At low energies, or small distances, the strong force reduces and quarks can be considered free particles. As quarks are pulled apart, the binding energy between them increases until the point when it is energetically favourable to create a quark-anitquark pair.

3.2.3 Electro-Weak Theory

The electro-weak theory is a unified theory combining electro magnetic and weak interactions. It uses $SU(2)\otimes U(1)_Y$ group to describe the interactions. Hyper-charge, Y, is related to the charge, Q, and the third component of isospin, I_3, by:

$$Q = I_3 + \frac{Y}{2} \tag{3.10}$$

Electro-weak interactions propagated using four gauge fields B_μ, W_μ^1, W_μ^2 and W_μ^3. B_μ are required to maintain invariance under electromagnetic transformations. The W_μ^1, W_μ^2 and W_μ^3 are required to maintain invariance under weak transformations.

Weak interactions violate parity, meaning that there is no symmetry between left-handed and right-handed fermions. By separating the Dirac field of a fermion,

it can be separated into left and right haded components. This representation is shown for the first generation in equation 3.11

$$q_L \equiv \begin{pmatrix} u_L \\ d_L \end{pmatrix}; u_R, d_R \qquad l \equiv \begin{pmatrix} e_L \\ \nu_L \end{pmatrix}; e_R \tag{3.11}$$

Here the subscript L and R refer to left-handed and right-handed fermions, respectively. It should be noted that there is no right-handed neutrino present in the Standard Model and that neutrinos are also considered massless. Though neutrinos have been found to have mass, this is not contained in the traditional Standard Model. To explain the presence of only left-handed neutrinos, a number of theories are being tested [30].

3.2.4 The Higgs Mechanism

The Standard Model requires that gauge fields are massless. Experiment has been shown that both the W and Z bosons are massive. To introduce mass to these fields, and to fermions, a scalar field ϕ, known as the Higgs field has been postulated. This field breaks the electro-weak symmetry and in the process gives mass to the weak vector bosons and fermions. This mechanism is refered to as spontanious symmetry breaking. It is based on the Goldstone theorem [31] where a Lagrangian has a continuos global symmetry which is not the trivial symmetry assocciated with the vacuum then there exists one massless boson associated with each generator. The Higgs mechanism introduces a doublet of complex scalar fields $\phi^0(x)$ and $\phi^+(x)$ with hypercharge Y = +1 in $SU(2)_L \otimes U(1)_Y$ space:

$$\phi(x) \equiv \begin{pmatrix} \phi^{(0)}(x) \\ \phi^{(+)}(x) \end{pmatrix} = \frac{1}{\sqrt{2}} \begin{pmatrix} \phi_1(x) + i\phi_2(x) \\ \phi_3(x) + i\phi_4(x) \end{pmatrix} \tag{3.12}$$

These fields have an associated scalar potential V(ϕ) of the form:

$$V(\phi) = \mu^2\phi^\dagger\phi + \lambda(\phi^\dagger\phi)^2, \quad \lambda > 0 \tag{3.13}$$

If $\mu^2 > 0$ the potential has a trivial minimum at $\phi = 0$ which correspponds to the ground state of the system. It $\mu^2 > 0$ the potential is a given by:

$$| \langle 0 | \phi^{(0)} | 0 \rangle | = \sqrt{\frac{-\mu^2}{2\lambda}} = \frac{v}{\sqrt{2}} \tag{3.14}$$

Where v is the vacuum expectation value. This is non-trivial and has an infinite number of solutions corresponding to any point on a circle given by:

$$| \phi_0 |^2 = \frac{(\phi_1 + \phi_2 + \phi_3 + \phi_4)}{2} = \frac{v^2}{2} \tag{3.15}$$

This will result in four Goldstone bosons. Three will be massless and one will be massive and is known as the Higgs boson and will have a mass $M_H = \sqrt{2\lambda v^2}$. By perfroming a unitary guage transformation on the field $\phi(x)$ the three massless bosons can be removed and their degrees of freedom are used to give the weak vector bosons mass and a third, longitudinal, polerisation state.

The Higgs mechanism results in a physically observable mass being associated with the four fields. A combination of more than one of these fields can be seen in equations (3.16)(3.17)(3.18).

$$W_\mu^\pm = \frac{1}{\sqrt{2}}\left(W_\mu^1 \mp W_\mu^2\right) \tag{3.16}$$

$$\begin{pmatrix} Z_\mu \\ A_\mu \end{pmatrix} = \begin{pmatrix} \cos\theta_W & -\sin\theta_W \\ \sin\theta_W & \cos\theta_W \end{pmatrix} \begin{pmatrix} W_\mu^3 \\ B_\mu \end{pmatrix}$$

$$Z_\mu^0 = W_\mu^3 \cos\theta_W - B_\mu \sin\theta_W \tag{3.17}$$

$$A_\mu = W_\mu^3 \cos\theta_W + B_\mu \sin\theta_W \tag{3.18}$$

The full electro-weak Lagrangian contains three components describing fermion interactions ($L_{Fermions}$), boson interactions (L_{Bosons}) and the Higgs mechanism (L_{Higgs}):

$$L_{EW} = L_{Bosons} + L_{Fermions} + L_{Higgs} \tag{3.19}$$

The first term describes the interactions between the massless gauge bosons and is given below:

$$L_{Bosons} = -\frac{1}{4} W^i_{\mu\nu} W^{i\mu\nu} - \frac{1}{4} B_{\mu\nu} B^{\mu\nu} \tag{3.20}$$

with the $W^i_{\mu\nu}$ and $B^{\mu\nu}$ the field tensors given by:

$$W^i_{\mu\nu} = \partial_\nu W^i_\mu - \partial_\mu W^i_\nu - g_2 \epsilon^{ijk} W^j_\mu W^k_\nu$$

$$B_{\mu\nu} = \partial_\nu B_\mu - \partial_\mu B_\nu$$

where g_2 is the weak isospin coupling constant and the indices i, j, k run from 1 to 3.

The second term in equation 3.19 describes the coupling of fermions to the massless gauge boson mediators (W^1, W^2, W^3 and B).

$$L_{Fermions} = \overline{\Psi}_L \gamma_\mu D^L_\mu \Psi_L + \overline{\Psi}_R \gamma_\mu D^R_\mu \Psi_R \tag{3.21}$$

with the covariant derivatives defined by:

$$D_\mu^L = \left(\partial_\mu - ig_2\frac{\sigma^i}{2}W_\mu^i - ig_1\overline{Y}2B_\mu\right) \tag{3.22}$$

$$D_\mu^R = \left(\partial_\mu - ig_1\frac{Y}{2}B_\mu\right) \tag{3.23}$$

Here g_1 is the weak hypercharge coupling.

The final term in equation 3.19 comes from the addition of the Higgs field and has the form:

$$L_{Higgs} = \left(D_\mu^L\phi\right)^\dagger\left(D_\mu^L\phi\right) - V(\phi) - g_f\overline{\psi}\phi\psi \tag{3.24}$$

where $V(\phi)$ is the scalar potential of the Higgs field. The first term is the interaction between the Higgs field and the gauge boson mediators. The last term comes from the Yukawa coupling between the fermions and the Higgs field, giving rise to mass terms for the fermions.

3.3 Neutral B Meson Mixing

It has previously been observed that particles can change from particle (B^0or B_s^0) to antiparticle ($\overline{B}^0$ or $\overline{B}_s^0$) and vice-versa. This process is known as mixing. The leading Standard Model Feynman diagrams for this process are shown in figure 3.1. While it is possible for the transition to proceed with both up and charm quarks, the dominant role comes from the top quark, due to its greater mass. (The amplitude for this process is proportional to the mass of the exchange fermion.) The existence of mixing implies that the mass eigenstates of the B_s^0 meson are a

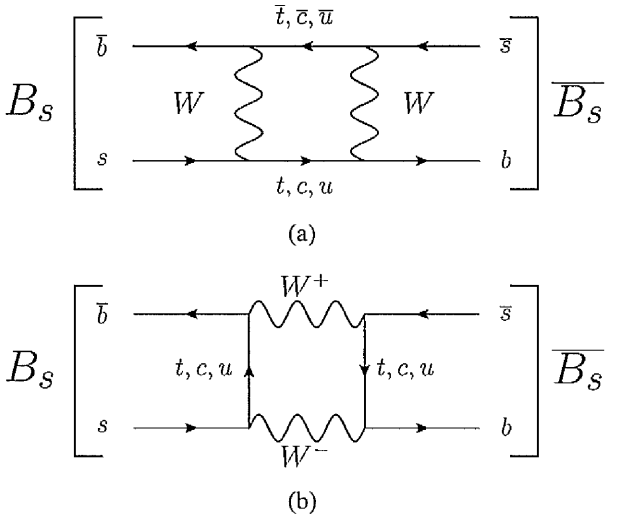

Figure 3.1: Feynman diagrams for mixing in B_s^0 system.

linear combination of B_s^0 and $\overline{B}_s^0$ states.

$$|B_{H,L}\rangle = p\,|B_s^0\rangle \mp q\,|\overline{B_s^0}\rangle \tag{3.25}$$

The time evolution is given by the solution to the time dependent Schrödinger equation:

$$i\frac{\mathrm{d}}{\mathrm{dt}}\begin{pmatrix} B_s^0(t) \\ \overline{B_s^0}(t) \end{pmatrix} = H\begin{pmatrix} B_s^0(t) \\ \overline{B_s^0}(t) \end{pmatrix} = \left(M - \frac{i}{2}\Gamma\right)\begin{pmatrix} B_s^0(t) \\ \overline{B_s^0}(t) \end{pmatrix} \tag{3.26}$$

where the mass and lifetime matrices M and Γ are Hermitian. The time dependence is expressed by equation 3.27.

$$|B_{H,L}(t)\rangle = e^{-\left(im_{H,L}+\frac{\Gamma_{H,L}}{2}\right)t}\,|B_{H,L}(0)\rangle \tag{3.27}$$

Solving equation 3.26 also gives the ratio q/p related to the mass and lifetime

matrix elements:

$$\frac{q}{p} = -\sqrt{\frac{M_{12}^{*} - i\Gamma_{12}^{*}/2}{M_{12} - i\Gamma_{12}/2}} \tag{3.28}$$

if there is CP violation in the oscillation of neutral B mesons $|q/p| \neq 1$

3.4 CP Violation

CP symmetry is the combination of charge conjugation (C), the transformation of a particle to its anti particle by changing the sign of its charge and Parity (P), which is the inversion of the space coordinates, creating a mirror of the physical system. With the conservation of CP, particles and anti particles are expected to behave in exactly the same way. As the universe demonstrates that there is an imbalance in the amount of matter and antimatter, CP violation (CPV) can be used to explain some of this imbalance. CPV has previously been observed in the neutral kaon system [32].

CP violation can occur through three mechanisms in the B meson system: in the mixing, in the decay and in the interference between mixing and decay.

3.4.1 CP violation in mixing

This requires that the oscillation probability of $B^0 \rightarrow \overline{B}^0$ and $\overline{B}^0 \rightarrow B^0$ is different. If this happens the CP eigenstates differ from the mass eigenstates, B_H and B_L. Experimentally, this can be measured in decays such as $B_s^0 \rightarrow D_s^- \pi^+$ and $\overline{B_s^0} \rightarrow D_s^+ \pi^-$ CPV in both the B_d^0 and B_s^0 systems is expected to be small [3] (¡10^{-3}) which implies that the mass states are almost exact CP eigenstates.

3.4.2 CP violation in decay

When there is a difference in the decay amplitude of a particle (B_s^0) to a final state f and an antiparticle ($\overline{B}_s^0$) to the equivalent state $\overline{f}$ it is known as CPV in decay. It can be expressed as $|A_f/\overline{A}_f| \neq 1$ This has been observed in the kaon and B systems [33, 34, 35].

3.4.3 CP violation in interference between mixing and decay

CP violation also occurs when there is interference between the decay and mixing. This arises when there is a phase between the mixing (q/p) and decay amplitudes ($\overline{A}_f/A_f$). This requires that there is a decay amplitude for both $B_s^0 \rightarrow f$ and $B_s^0 \rightarrow \overline{B}_s^0 \rightarrow f$.

3.4.4 Cabibbo-Kobayashi-Maskawa (CKM) Matrix

The CKM matrix is used to describe the relation between the weak eigenstates (d, s, b) and the mass eigenstates (d', s', b'). Each element corresponds to the possible transitions between quark flavours and the strength of the weak charged current coupling.

$$\begin{pmatrix} d' \\ s' \\ b' \end{pmatrix} = V_{CKM} \begin{pmatrix} d \\ s \\ b \end{pmatrix} \tag{3.29}$$

where

$$V_{CKM} = \begin{pmatrix} V_{ud} & V_{us} & V_{ub} \\ V_{cd} & V_{cs} & V_{cb} \\ V_{td} & V_{ts} & V_{tb} \end{pmatrix} \tag{3.30}$$

The CKM matrix is a 3×3 unitary matrix containing nine complex elements. This yields eighteen parameters: nine are constrained by the unitarity, six by orthogonality and three by normalisation. This leaves nine remaining free parameters, of which five are arbitrary phases associated with the quark fields and can be discarded. This results in four free independent parameters: these are three Euler angles associated with the rotation in 3-dimensional space and one complex phase, δ. It is through δ that CP violation enters the Standard Model.

3.4.5 Wolfenstein Parametrisation

The Wolfenstein parametrisation [36] of the CKM matrix is based on the hierarchy of the quark transition strengths, via charged current interactions. It uses a power series expansion in λ where:

$$\lambda \equiv \sin\theta_C \simeq |V_{us}| \sim 0.22 \tag{3.31}$$

and θ_C is the Cabibbo angle. The different orders of magnitude seen in the transitions between the different quarks relate to the orders of λ in the CKM terms.

$$V_{CKM} \approx V_{CKM}^{(3)} + \delta V_{CKM} + \mathcal{O}(\lambda^6) \tag{3.32}$$

where $V_{CKM}^{(3)}$ is give by:

$$\begin{pmatrix} 1-\frac{1}{2}\lambda & \lambda & A\lambda^3(\rho-i\eta) \\ -\lambda & 1-\frac{1}{2}\lambda^2 & A\lambda^2 \\ A\lambda^3(1-\rho-i\eta) & -A\lambda^2 & 1 \end{pmatrix} \tag{3.33}$$

3.4.6 The Unitary Triangle

The unitarity of the CKM matrix satisfies the condition that $V_{CKM}^{\dagger}V_{CKM} = \mathbb{1}$. This yields six orthogonality relations. The sum of the complex numbers in each of these is zero, this is usually represented by a triangle in the complex plane. Of the six triangles generated only, two have sides of comparable lengths. The relations for these triangles are given in equations 3.34 and 3.35

$$V_{ud}V_{ub}^{*} + V_{cd}V_{cb}^{*} + V_{td}V_{tb}^{*} = 0 \tag{3.34}$$

$$V_{ud}V_{td}^{*} + V_{us}V_{ts}^{*} + V_{ub}V_{tb}^{*} = 0 \tag{3.35}$$

From these equations, and dividing by $V_{cd}V_{cb}^{*}$, the unitarity triangles in figure 3.2 can be drawn.

From the triangles in figure 3.2 the angles can be defined as follows:

$$\alpha = arg\left(\frac{V_{td}V_{tb}^{*}}{V_{ud}V_{ub}^{*}}\right) \tag{3.36}$$

$$\beta = arg\left(\frac{V_{cd}V_{cb}^{*}}{V_{td}V_{tb}^{*}}\right) \tag{3.37}$$

$$\gamma = arg\left(\frac{V_{ud}V_{ub}^{*}}{V_{cd}V_{cb}^{*}}\right) \tag{3.38}$$

$$\beta' = arg\left(-\frac{V_{ts}V_{us}^*}{V_{td}V_{ud}^*}\right) \tag{3.39}$$

$$\gamma' = arg\left(-\frac{V_{tb}V_{ub}^*}{V_{ts}V_{us}^*}\right) \tag{3.40}$$

where β and γ are related by:

$$\beta' = \beta + \chi, \quad \gamma' = \gamma - \chi \tag{3.41}$$

and χ is defined as:

$$\chi = arg\left(-\frac{V_{cb}V_{cs}^*}{V_{tb}V_{ts}^*}\right) = -\frac{1}{2}\phi_s \tag{3.42}$$

where ϕ_s is the phase of the B_s oscillations.

3.5 Measurements from $B_s^0 \rightarrow D_s^{\pm} D_s^{\pm}$

This decay is of interest to study as it is possible to make measurements of the mass difference and the decay width difference between the two mass eigenstates of the B_s^0 system, B_s^L and B_s^H. The final decay state is CP even and it is possible to make measurements of $\Delta\Gamma_s/\Gamma_s$ [37, 38], which is the difference in the decay width between the two mass eigenstates B_L and B_H divided by the mass width. $\Delta\Gamma_s/\Gamma_s$ can be found using equation 5.1:

$$\frac{\Delta\Gamma_s}{\Gamma_s} \simeq \frac{2\mathrm{BR}(B_s \rightarrow D_s^{(*)+} D_s^{(*)-})}{1 - \mathrm{BR}(B_s \rightarrow D_s^{(*)+} D_s^{(*)-})} \tag{3.43}$$

Where $BR(B_s \rightarrow D_s^{(*)+} D_s^{(*)-})$ is the branching fraction for all of the decay modes; which can have one, two or zero $D_s^{*\pm}$particles. This requires the following conditions; using the heavy quark limit and requiring that the mass and CP-eigenstates coincide. For a more complete explanation see [39, 40] this has been used in several studies [38, 41, 42, 43].

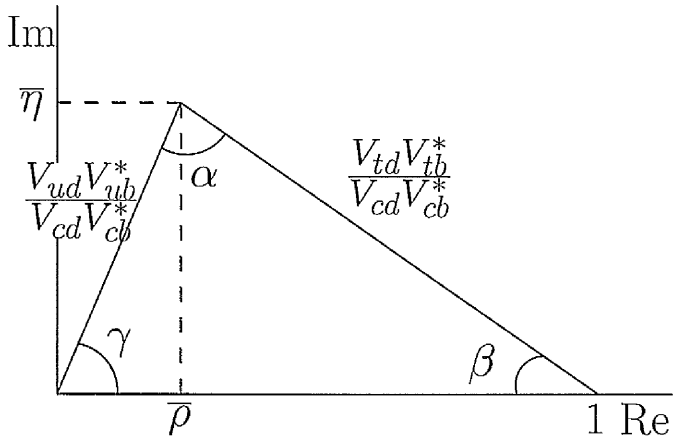

(a) Unitary triangle for Equation 3.34

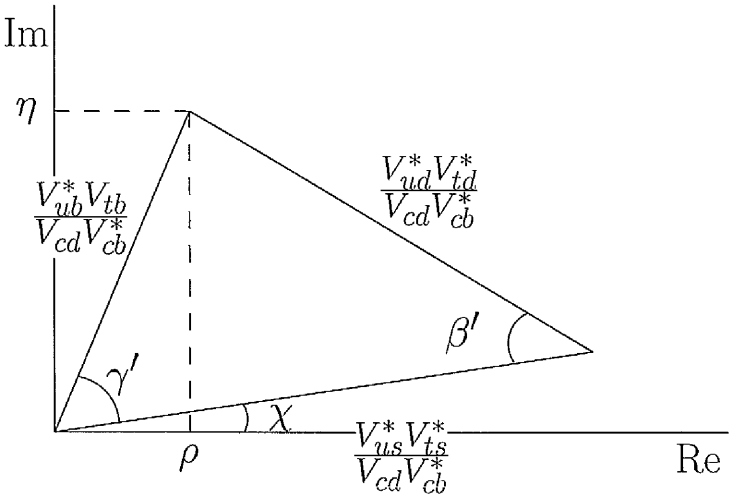

(b) Unitary triangle for Equation 3.35

Figure 3.2: Unitary triangles for equations (3.34 and 3.35)

Chapter 4

The VELO

4.1 Introduction

The VELO is the vertex detector in LHCb and is located around the interaction point. It covers the full acceptance of LHCb. The VELO comprises 84 silicon strip sensors of half disk shape, with a thickness of 300 μm, aligned edge on to the beam and positioned with their first active strip 8.2 mm from the beam, when closed. Being this close to the beam presented many challenges when designing the VELO. This chapter looks at the ways the VELO has been designed to enable it to operate in these conditions. It will also discuss the simulation of energy deposition in the VELO; how this has developed and the performance of the VELO during data taking in 2010.

4.2 Silicon Strip Detectors

This section describes the design considerations and operation of silicon strip detectors, and the way in which a signal is created and read out of the VELO sensors.

The key components in the design of silicon strip detector are the bulk, the implants and the backplane. Figure 4.1 shows a schematic of a VELO sensor and what happens as a charged particle passes through. When passing through material, a charged particle looses energy. In silicon this can create electron/hole pairs. A bias voltage is applied and creates an electric field under which the electrons drift towards the readout strips.

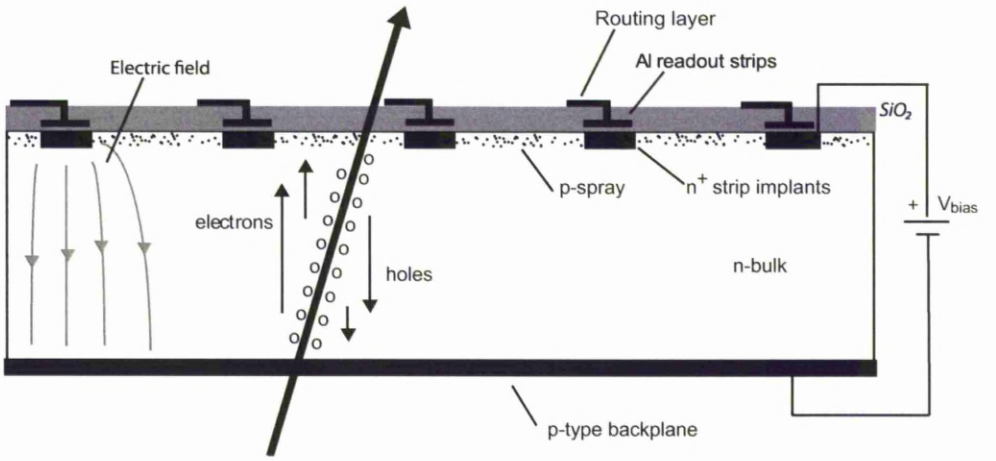

Figure 4.1: A schematic of a VELO sensor with a charged particle traversing, showing electric field lines from the implants and the drifting of electrons and holes through the bulk. There is also a layer of SiO_2 used to isolate the readout strips from the silicon. [2]

Silicon bulk can be categorised as either p or n type. This name comes from the addition of dopants to the pure silicon. By adding donor atoms, from group 5 in the periodic table, an extra electron is given to the silicon lattice. This is known

as n type silicon. The extra electrons give rise to a new discrete energy level just below the conduction band. For p type silicon the bulk is doped with an acceptor from group 3 atoms. In this case, the additional atoms create a hole, which acts as an electron in the conduction band.

Silicon is often refered to by its bulk and inplant properties. For example, n-in-p has a silicon bulk of p-type silicon and implants of type n.

The VELO detector consists of 21 stations, with both an R and Phi sensor at each point. The sensors are made with 300 μm n-in-n sensors. There is one station of 300 μm n-in-p, which is being used to study radiation damage.

Silicon strip detectors are used to detect the passage of charged particles. They are segmented into strips to enable precise position information to be collected. The VELO uses two different strip layouts (R and Phi) to create the 3D VELO hits, used for tracking and vertexing of particles. Figure 4.2 shows the strip layout of the R and Phi sensors.

4.2.1 Energy Loss in Silicon Detectors

For simulation and readout, it is important to know how energy is lost as particles pass through a material. The mean rate of energy loss, as particles pass through materials, is described by the Bethe-Block equation, shown in equation 4.1. This describes the mean energy loss from particles of a certain momentum, traversing a chosen material. The different terms in the Bethe-Block equation have greater influence in different momentum ranges. Figure 4.3 shows how the mean energy loss changes as a function of incident particle energy. The region of greatest

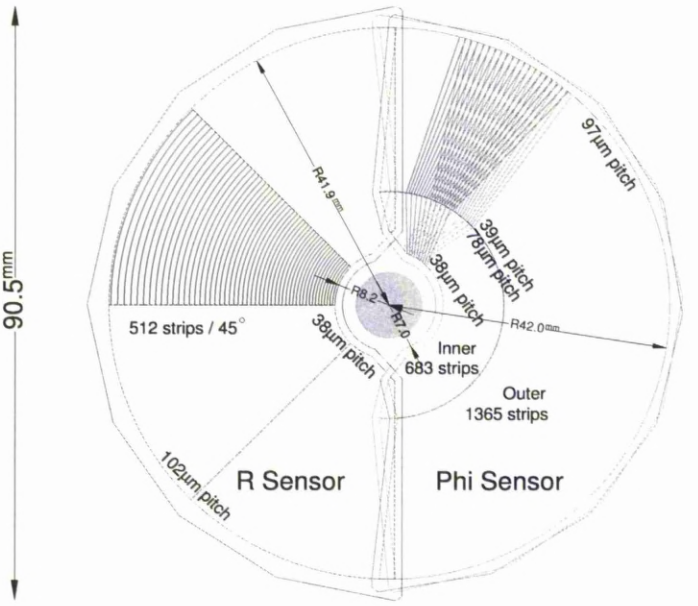

Figure 4.2: Strip layout for R and Phi sensors. The R sensors are split into four regions with pitch increasing from 38 μm to 102 μm. The Phi sensors are split into two regions, inner and outer, with pitch going from 38 μm to 78 μm in the inner and 39 μm to 97 μm in the outer. In moving from the inner to the outer region there is a 'dog leg' effect, as the angle of the strips changes. The diagram also shows the stereo angle introduced by changing the way which the Phi sensor faces [2].

interest for LHCb lies between a $\beta\gamma$ of 1 and 100.

$$-\frac{dE}{dx} = 2\pi N_A r_e^2 m_e c^2 \frac{Z}{A}\frac{z^2}{\beta^2}\left[\ln\left(\frac{2\mathrm{m_e c^2}\beta^2\gamma^2\mathrm{T_{max}}}{\mathrm{I^2}}\right) - 2\beta^2 - \delta(\beta\gamma) - 2\frac{C}{Z}\right] \qquad (4.1)$$

where Z is the atomic number of the absorber; A is the atomic mass of the absorber; z is the charge of the incident particle; $2\pi N_A r_e^2 m_e c^2 = 0.1535$ MeVcm^2/g; with N_A Avogadro's number (6.022×10^{23}mol^{-1}); r_e is the classical electron radius ($= 2.817 \times 10^{-13}$ cm); $m_e c^2$ is the electron rest mass (0.511 MeV); I is the logarithmic mean excitation energy (174 eV); β is the particle speed as a fraction of the speed of light; γ is the Lorentz factor $\left(= \frac{1}{\sqrt{1-\beta^2}}\right)$; δ is the density correction and takes into account the shielding; T_{max} is the maximum kinetic energy, which

can be imparted to a free electron in a single collision and C is a shell correction.

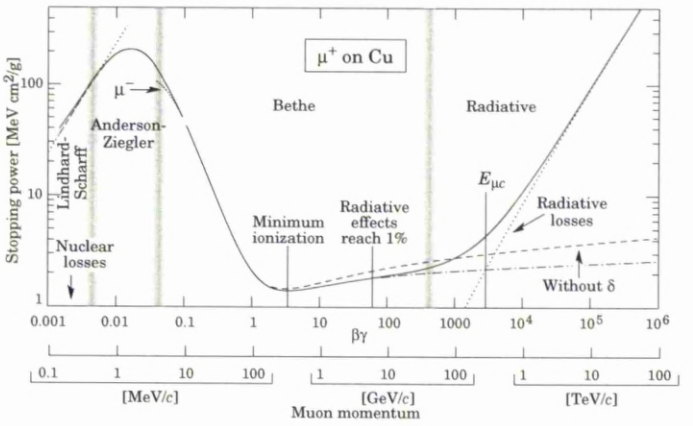

Figure 4.3: Expected energy loss from Bethe-Bloch equation for Muons in copper [3]. Where the stopping power is $\frac{(dE/dx)}{\rho}$.

Whilst the mean energy deposited is of interest, it is important to note that the mean is not the the most likely energy deposited by a particle. This is because the distribution describing the energy deposited has an asymmetric shape, with a long high-side tail, because of the possibility of large energy transfers from a single collision. This is described by the Landau distribution shown in figure 4.4(a). The Landau function was first calculated by Lev Landau [44], with the following assumptions:

- the non-relativistic Rutherford cross section can be used, meaning that the maximum energy transfer possible is infinite;
- electrons can be treated as free, therefore neglecting the binding energy of the atomic electrons to the nucleus;
- the particles' velocity is unchanged by the interactions.

The Landau distribution gives a reasonable approximation of the peak of the

distribution but consistently underestimates the width. Vavilov proposed improvements which generalise Landaus approach, by using the relativistic Rutherford cross-section and including a cut off in the maximum energy transfer allowed. However, this method still underestimates the width, as it doesn't take into account the binding energy of atomic electrons. The practical way that this problem is solved, is by the convolution of a Landau and Gaussian function. For a detailed discussion of this see [45, 46]. This has proved successful and Figure 4.4 shows a typical energy deposition distribution from the VELO, which has been fitted first with a Landau and then with a Landau convollved with a Gaussian.

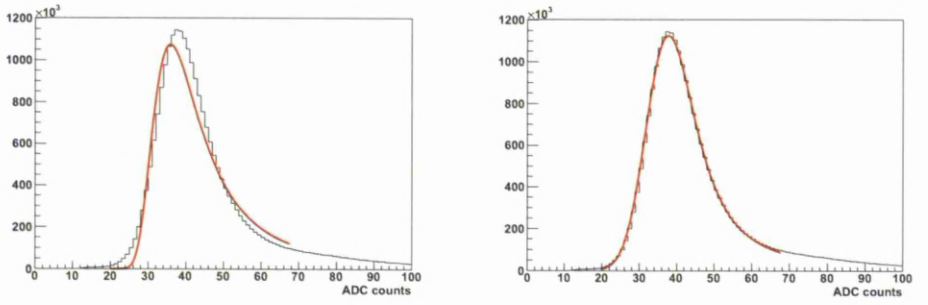

(a) (b)

Figure 4.4: Two fits to the ADC counts, recorded in the VELO, proportional to the energy deposited in the silicon. a) A Landau distribution has been fitted. b) A Landau⊗Gaussian has been fitted. From inspection, it is possible to see that the convolution fits the data better.

The most probable value(MPV) of a Landau is given by [45]:

$$\Delta_p = \xi \left[ln\left(\frac{2m_e c^2 \beta^2 \gamma^2}{I}\right) + ln\frac{\xi}{I} + 0.2 - \beta^2 - \delta \right] \tag{4.2}$$

where ξ is the scale of the Landau distribution and is given by:

$$\xi = \frac{0.017825t}{\beta^2} \tag{4.3}$$

with: I, t, $m_e c^2$, β, γ and δ as defined earlier. The width of the distribution is the second parameter used to characterise the shape of the Landau. By definition, the full width half maximum (FWHM) of a Landau is given by 4.018 ξ [45] but this does not effectively describe the data. From equations 4.2 and 4.3, it can be seen that the width and MPV depend only on the $\beta\gamma$ of the incident particle. By plotting MPV as a function of momentum, it is possible to separate out different particle types.

When using a Landau $\otimes$ Gaussian, this gives three separate measures of the width: the FWHM of the full function; the Landau width and the Gaussian smearing.

4.3 VELO detector

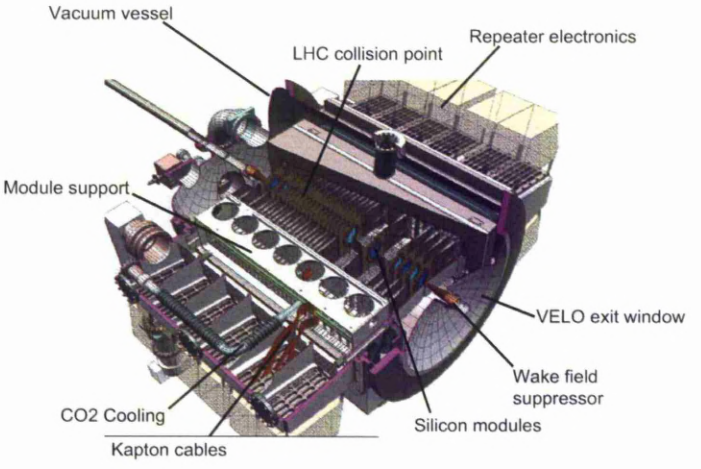

Figure 4.5: Overview of the VELO Detector, showing the VELO modules and surrounding structure used in the readout and operation of the VELO [4].

4.3.1 Detector Overview

The VELO consists of 21 stations each with 2 modules, with each module containing an R and Phi silicon sensor. All but one station is made of n-in-n type silicon. The other station is made with p-in-n type silicon and is identical in all other respects to the other modules. This module was added to provide a study case to confirm the radiation hardness of the p-in-n type silicon. The VELO is designed to be movable from an x = 0.0 mm to ±29 mm, so that during the injection and ramping of the beam it can remain at a distance unstable beams will not reach. VELO modules in their open and closed positions can be seen in Figure 4.6. That also shows the overlapping of the R and Phi sensors in the closed position.

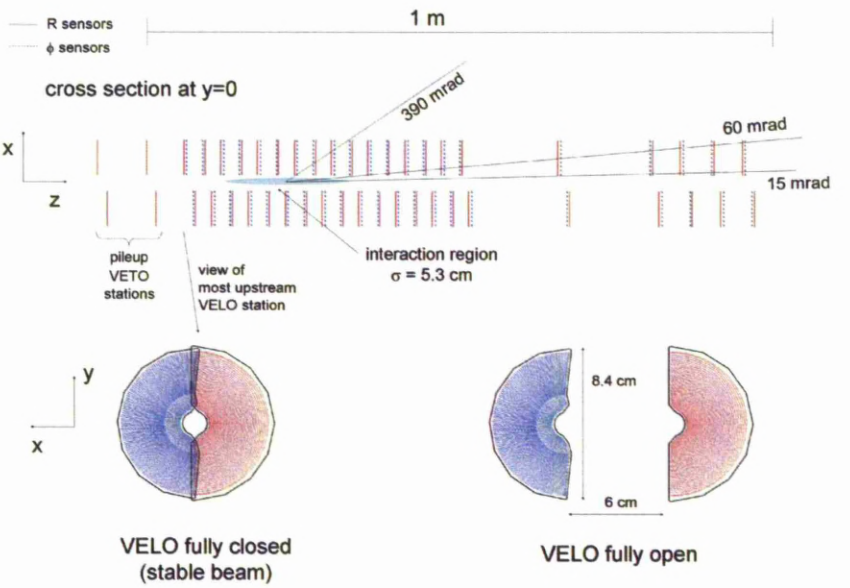

Figure 4.6: Overview of VELO station position relative to beam axis(top) and in the x-y plane when closed(bottom-left) and open(bottom-right) [4].

The sensors are isolated from the LHC vacuum by the RF-box. This is made

from aluminium foil and designed to reduce the effect of pickup in the VELO sensors from the proton beam fields. The box has been hand-ground to reduce the quantity of material. Its surface has been corrugated to add rigidity to the box and to allow sensors to overlap when fully closed. The RF-box is the single biggest contribution to the material budget of the VELOfor tracks within the acceptance.

4.3.2 Sensors

The VELO uses two types of strip layout R and Phi. These both use 300 μm silicon and each has 2048 strips. The strip layouts can be seen in Figure 4.2. They have been designed to have a finer pitch at smaller radii, so as to allow comparable occupancy across the whole sensor. Each of the strips is read out along routing lines on top of the silicon. These lines carry signals to Beetle chips where pre-amplification and signal shaping occur.The Beetle chips are mounted onto the hybrid, which is connected to a carbon fibre stand.

The cooling uses a two phase CO_2 flow system [47] and has to satisfy the requirement of maintaining a sensor temperature below -10 °C in full operational conditions.

4.3.3 Readout Chip

The analogue signal from the silicon is readout using a custom designed chip. The chip used is known as the Beetle chip [48]. The chip was designed to meet strict requirements imposed by both the VELO group and LHCb project. It was required to have a pulse rise time less than 25 ns and a spill over less than 30% of

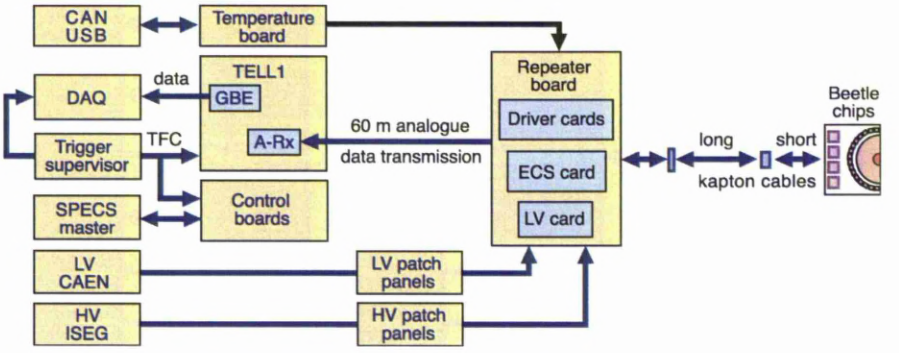

Figure 4.7: Overview of the VELO electronics readout chain [2].

the peak value. It needs to be radiation hard as it will have to operate in the harsh environment close to the beam.

The properties and performance of the beetle chip has been tested at several test beams [49]. From these studies it was found that the chip satisfied all requirements.

4.3.4 Data Acquisition

The readout of the VELO sensors uses TELL1 boards [50] to translate the analogue signal to digital. These boards are used by all of LHCbs sub detectors except the RICH. For the VELO, the TELL1s process the raw data and output zero suppressed(ZS) data, so that only strips with clusters are readout. The processing of data requires several stages performed by FPGAs on the TELL1 boards. The whole process has been emulated in bit perfectness to enable offline verification and development of the algorithms. The VELO also uses the TELL1s to output the non zero suppressed(NZS) data, which is done at a small rate to keep data size low. This is done so that noise calculations can be made and improvements to

algorithms tested.

Pedestal calculation

The ARx cards convert the analogue signal of each Beetle channel to a value in the range 0 - 1023 ADC counts. Pedestal values are subtracted on a per strip basis and these values may vary according to factors such as external temperature.

Header Cross Talk

The last two header bits are used to encode the pipeline column number, which is the position of the event in the Beetle pipeline buffer. Due to cross-talk, a fraction of the signal from the last header bit spills into the first Beetle channel of a link. A link is 32 channels. Because both the level of cross-talk and the pulse height of the header bit are known, the spill over effect can be corrected for. If no correction is applied the first channel in each link will appear noisy.

Channel Reordering

The way channels are ordered in readout does not always correspond to the strip order. This is prominent in the Phi sensors, as the channel order and strip order is mixed. Before making clusters, channels need to be reordered to the physical strip position, so that these can be used by the clusterisation.

Mean Common Mode Subtraction(MCMS)

Noise can come into the sensors in different ways. To reduce its effects two algorithms have been developed. These remove the noise from links MCMS and LCMS. The MCMS algorithm calculates the mean of a link with and without 'real' clusters and removes the calculated mean from the full link.

Linear Common Mode Suppression(LCMS)

The LCMS process is described briefly here and is described in greater detail in [51]. The LCMS algorithm starts by calculating a mean, then looks for a slope across the length of the link and tries to compensate for it. Using the slope, corrected values hit detection and removal is performed and the hit value is replaced with zero. Then another mean subtraction and slope removal is performed, after which the clusterisation is performed.

A bug was found with this algorithm. In the case of large signals at the ends of links, an incorrect slope was asigned in the correction. For much of the data taking in 2010, this algorithm was switched off when testing of a corrected algorithm was undertaken. This has been corrected for by removing hits when calculating the mean.

Clustering

Clustering refers to the way in which the ADC counts on strips are added together to form groups or clusters. In the VELO, clustering starts by looking for seed strips. These are strips with an ADC count greater than 10. Adjacent strips are

then considered for possible inclusion. There is an inclusion threshold which is dependant on the noise levels in each strip. Clusters can contain a maximum of 4 strips, each with a maximum ADC of 127. By combining information from more than one strip, it is possible to reconstruct the position of a hit more precisely and give a better than binary hit resolution.

4.4 VELO Simulation

When the VELO runs, there are a variety of plots used to monitor its performance. It is essential that, as radiation damage of sensors increases, optimal performance is maintained. This section looks at a group of software packages used to monitor different aspects of the detector. Plots from these are then compared with data and Monte Carlo (MC). It is important that differences in the data and simulation are well understood. A brief explanation of the simulation process and an example of how this has developed is given.

4.4.1 Software Structure

Simulation of the VELO is done using the LHCb core software packages. There are several stages to the simulation process. These can be seen in Figure 4.8. The first phase of the simulation uses Gauss [52]. Gauss is used to simulate the detector and its condition. Using GEANT4 [53], Gauss is able to simulate the particle interactions as they pass through materials inside the detector. Section 4.4.2 makes a comparison of the way this is done for different particles and different versions of Gauss and GEANT4. The simulation is then tuned to give the same

performance as the real detector.

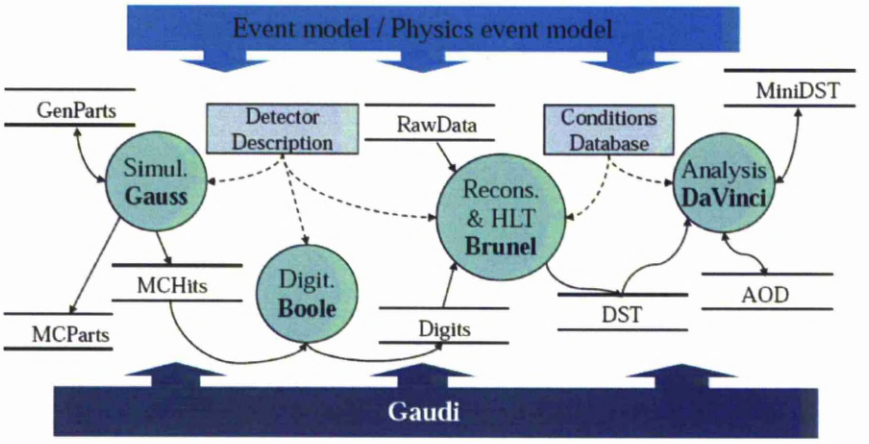

Figure 4.8: Layout of the LHCb software going from simulation to analysis phase [4].

Boole is the program that does the digitisation of the detector. This is where the emulation of the TELL1 algorithms is done and the MC is expected to match the data. From Boole, the next step is the reconstruction, which can be the same for both data and MC, the only difference being the addition of truth information for the MC.

4.4.2 Energy Deposition Simulation

Different versions of GEANT4 have been used in different versions of Gauss. It is important to check that different versions of software produce the correct theoretical results and after processing with Brunel agree with the data taken. This section discusses the changes found when using different versions of Gauss, specifically in energy deposition and its agreement with the theory from Section 4.2.1. Understanding the energy deposition in simulation and how this compairs to data is

important because it plays an important role in tracking studies. It is also important for understanding the effects that radiation damage is having and how this will later effect the performance of the Velo. Modifications are currently being made to apply radiation damage to sensors in the simulation.

To study the reliability of GEANT4 versions, a selection of particle types have been chosen. These are electrons, protons, pions, kaons and muons. They give a variety of masses and particle types i.e. leptons, baryons and meson. The following plots show the results for each of the following GEANT4 versions:

- v25r9 - This was used for the Monte Carlo production MC06;
- v30r2 - This version had a known bug which was corrected for later versions and has only been included to demonstrate the evolution of the software;
- v30r5 - This version included the correction and a smearing correction used to improve the width;
- v35r5 - This version was used for production of the MC09 Monte Carlo.

All Particle Types

A comparison of the energy deposition for all particle types of all energies has been made. This is shown in figure 4.9 where a clear difference can be seen between v25r9 and the others. Although there is only a very small difference when going between v30r5 and v35r5, the effect is the result of an improved simulation model compared to the previous simulation with additional smearing as in v30r5. For v30r2 the simulation requires smearing and scaling.

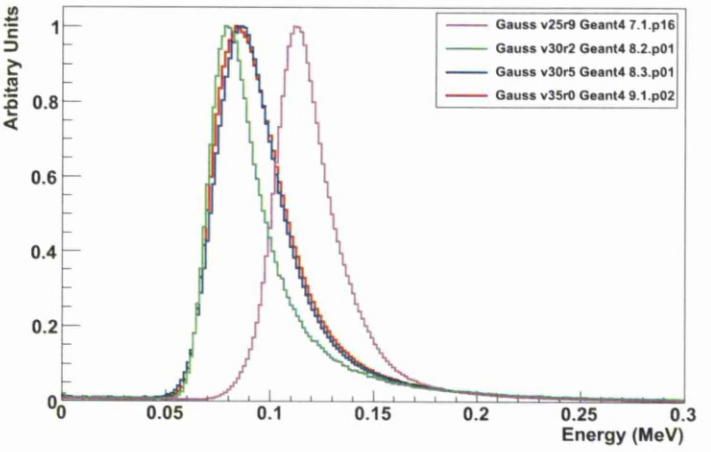

Figure 4.9: Energy deposited by all particle types in the VELO sensors. Four versions of Gauss are shown: v25r9, v30r2, v30r5 and v35r0. The plots are normalised so that their peaks are at 1.

For comparison figure 4.4.2 shows the energy deposition, in ADC counts, from data and simulation (v35r0). These show good agreement in their shape with a small shift in the peak.

The plot of individual particle types, as a function of $\beta\gamma$ is discussed in the next few sections. These will be compared to the data and theoretical calculations taken from [45, 54, 55, 56]. The theoretical calculations used involved the process of convolution of the Landau for a specific energy with a Gaussian. This is discussed in most detail in [45] and will be referd to as the Landau model from now on.

Pions

Figure 4.11 shows the results of the energy deposited by pions as a function of $\beta\gamma$. A comparison of these results is made with the experimental and theoretical val-

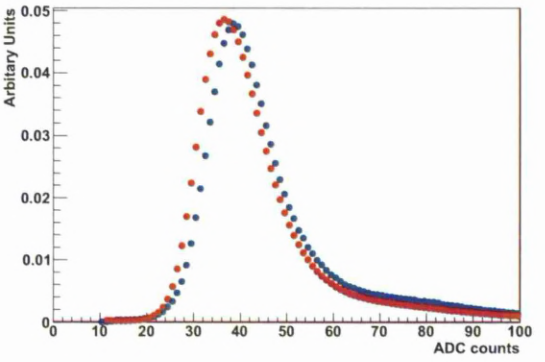

Figure 4.10: The energy deposition (in ADC counts) from Velo sensors for data (blue) and Monte Carlo (red). Using v35r0 of the simulation.

ues, from the Landau model mentioned eariler. For Gauss v25r9, the MPV values are overestimated and the shape is incorrect. Initially ($\beta\gamma < 50$), the distribution has a gradient steeper than the theoretical one. At higher $\beta\gamma$ (~ 100), the gradient is decreasing. The decrease seen is not as rapid as for the theoretical values, which are close to flat.

Their widths are underestimated but seem to be consistently, Gauss v30r5 is closer to the expected values of MPV and FWHM. The MPV values are bigger at $\beta\gamma$ less than 50 and smaller at $\beta\gamma$ greater than 60.

For Gauss v35r0, the situation is similar to v30r5, except that now the MPV values below a $\beta\gamma$ of 40 are consistent with theory. Above this point there is not a large enough gradient. The result is MPVs which are low. The widths of the Landaus are indistinguishable from those for Gauss v30r5.

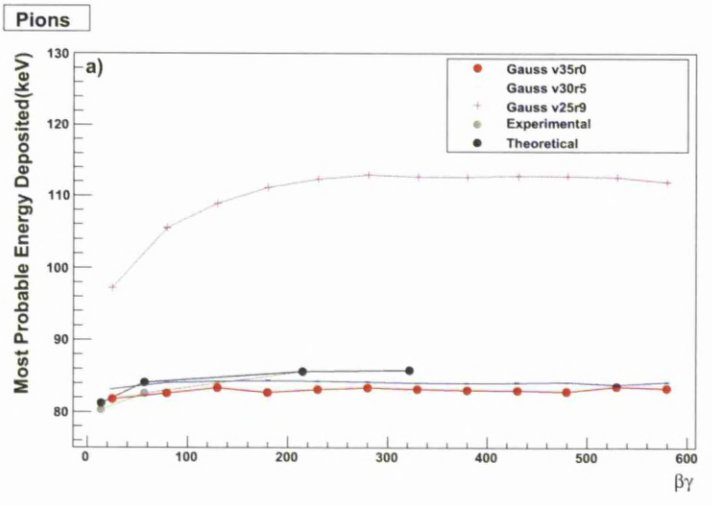

(a)

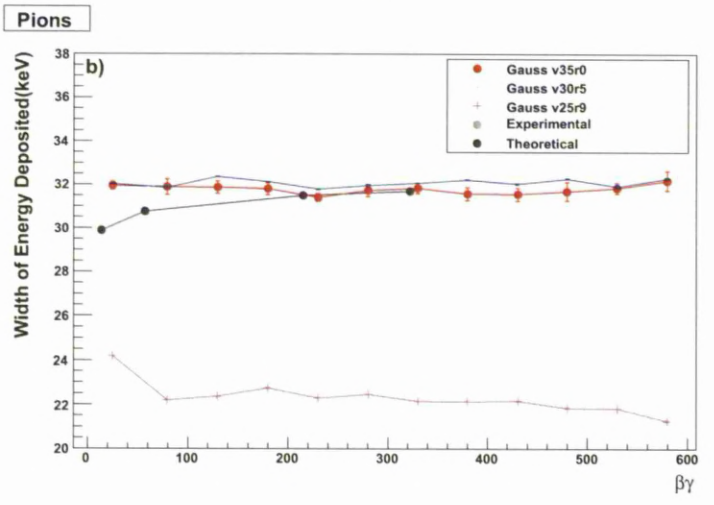

(b)

Figure 4.11: Results from fits to energy deposition in silicon for a range of $\beta\gamma$ for pions and anti-pions. a) MPV of the energy deposited b) FWHM of the energy deposited.

Protons

For protons plots of the MPV and FWHM are shown in Figure 4.12. Gauss v25r9 again has an overestimated MPV which has gradient larger than experimental val-

ues. The FWHM value is again underestimated, though the shape is consistent.

For Gauss v30r5 there is again improvement compared to Gauss v25r9. For $\beta\gamma$ less than 100 results are consistent with the Landau model theory and experiment. The values begin to fall below theory and experimental reults at higher $\beta\gamma$ though this is a small effect.

Gauss v35r0 shows an improvement, over Gauss v30r5, in the width of the Landaus and is positioned between v30r5 and theory. The MPVs have moved further from the theory than v30r5, though only by a small amount.

Muons

Plots for the muons are shown in Figure 4.13. For muons there is again greater agreement with the data in the version v30r5. The difference between v30r5 and v35r0 is a small reduction in the MPVs, The FWHM remain the same. The resulting MPVs have better agreement with the theoretical and experimental results. The FWHM remains the same for v30r5 and v35r0.

Electrons

Figure 4.14 shows how the electrons behave. For the theoretical and experimental values the agreement is not as good as for the other particle types. The electrons also show the least improvement in changing from v25r9 to v30r5. The MPVs show a change from v30r5 to v35r0. For $\beta\gamma$ less than 500 there is an improvement. At larger $\beta\gamma$, the MPVs follow show the same effects as v30r5. Thought there is improvement with regard to the shape for both MPV and FWHM. The MPVs and

FWHM values are overestimated.

Conclusion

By comparing the different versions of GEANT4, it can be seen that moving from v25r9 to v35r0 in Gauss, the energy deposition description has improved and is in better agreement with both theory and experiment. The distributions width and MPV have improved significantly and this is true for a range of particle types of different momentum. However, for electrons there are still improvements to be made for both the width and MPV.

4.5 Cluster Monitoring Software

This section discusses the monitoring of clusters found on VELO sensors and the performance over 2010. Cluster monitoring contains several sub sections. Some are to used to describe the raw clusters and some to look at clusters from tracks. Raw clusters are those strips which pass the seed threshold and include more noise clusters. Clusters from tracks are cleaner, as they must meet the minimum requirements to form a track and are therefor less likely to include noise clusters.

4.5.1 Energy Deposition in VELO Sensors

Fits to the cluster ADC, using a convolution of a Landau and Gaussian function described in Section 4.2.1, will be used to describe the shape of the ADC distributions. This has been done for each sensor to see how position relative to interaction

point affects distribution. Figures 4.15 and 4.16 compare the parameters of the fit for data and MC, looking at the MPV and FWHM. These plots use tracks reconstructed from data taken in 2010. There is an angular correction applied to scale the energy deposited. This is done by multiplying by cosine of the angle from the track relative, to the sensor.

Figure 4.15 shows the MPV for all sensors; for MC(blue) and data(red). The ratio between MC and data is in figure 4.15(b). These plots all have suppressed zeros and the difference is at the ~5% level for the R sensors and closer to 10% in the Phi sensors. This discrepancy is due to the differences in the way that the capacitance and noise values are calculated for the simulation. For the both the Phi and R sensors, the capacitance is given as a constant value in the simulation. This is known to be incorrect and increases as a function of strip length [57]. The Phi sensors have multiple sensors with MPVs which fall below the general trend. This effect was investigated and the differences in MPV is a result of a shift in the distribution. The reasons for this are unknown but as the effect a limited number of the MC data sets it is most likely an error in the generation of these particular files.

Figure 4.16 shows the FWHM, for each sensor again showing the MC(blue) and data(red). Again there is agreement at the 5% level between the data and MC. The difference in the bump which occurs in both R and Phi sensors is at the interaction point and can be explained by the different angular distribution of particles at this region. Even though an angular correction is applied to the tracks, because there is a larger proportion of 2 strip clusters, this has the effect of broadening the Landau distribution, because MPV of two strip clusters is 5% higher.

Different Cluster selections

This section looks at the MPVs in sensors for three different types of clusters:

- Raw: These are all the clusters found by the clusterisation algorithm;
- On Track: These are clusters which have been used to match to tracks;
- Angle Corrected: These use the on track clusters and apply a scaling to the energy deposited, so that it corresponds to a 300μm crossing of the silicon.

Figure 4.17 shows the MPV and FWHM from raw clusters, in both R and Phi sensors. The MPV in R is flat, whilest the Phi sensors have a bump around the interaction point, potentially from particles crossing with large angles which do not form tracks. There is a difference in MPV for the R and Phi sensors because of the strip layouts. When a charged particle crosses the R sensor at large angles the charge is deposited across more strips than in the Phi sensor.

The position of the interaction point can be clearly seen by the bump in the FWHM coming from the difference in the proportion of one and two strip clusters at this point, and the angle of tracks passing through strips.

For Monte Carlo and data the basic shape is correct. There is a shift in the MPV of the Phi sensors due to simplifications made in the simulation. There is a clearer dip in the MPVs for the MC For the FWHM there is a flat top in the data where there is a clear peak in the data. This could be due to the differences in the thresholds placed on MC and data. In data the thresholds are determined as a function of the noise of a strip. For simulation these thresholds are the same for all strips. It may also be related to the way that energy is spread through the

sensors but needs further investigation.

Figure 4.18 shows the same, but for clusters on tracks. Comparing this with figure 4.17, it can be seen that the FWHM is reduced in both R and Phi and that the MPV of the Phi sensor is also reduced. This comes from the reduction in the number particles which cross at large angles. This is reduced by the condition that tracks are required to have hits in three stations, which means that there are also less multiple strip clusters.

The MPVs for data and Monte Carlo shapes agree and have similar shapes. The FWHM agrees very well for both R and Phi.

Figure 4.19 shows MPV and FWHM for clusters on tracks and also applies an angular correction, so that the energy deposition is scaled to a 300μm crossing. The effect that this has, is to lower the MPV and to reduce the size of the FWHM by an even smaller amount. There is still a bump in the R and Phi widths, which comes from the fact that there is a difference in the MPV of one and two strip clusters, which has not been accounted for.

The shape of the Monte Carlo and data agree well but are shifted slightly. The FWHM is well simulated for both R and Phi.

Conclusion

By comparing the MPV and FWHM for MC and data, it has been shown that there is an agreement at the level of ~5%, which has been improved for MC2011. When looking at the way that the signal varies with station number and particle selection, the VELO gives a stable performance for all sensors. Over the course of

running, by monitoring how this performance varies, it is possible to assess how radiation damage is affecting the VELO sensors. With higher radiation doses, signals from strips are reduced. As the dose is not uniform across the whole sensor, it is possible to look for an increase in the width as a sign that radiation is having an effect. This is later seen with a reduction of the MPV in a sensor. This effect should be seen first in the sensor around the interaction point and later in the other sensors.

4.5.2 Most Probable Energy Deposit as a Function of Radial Position

Noise varies as a function of radial position in R in VELO sensors [2]. This section looks at how the MPV varies with R in both R and Phi sensors. The plots in this section show the variation of signal size as a function of radius for clusters formed from one and two strips. Figures 4.20(a) and 4.20(b) show the variation for R sensors and figures 4.22(b) and 4.21(b) show the Phi sensors. These plots look at station 20 only and use data(figures 4.20(a) and 4.22(b)) and MC (figures 4.20(b) and 4.21(b))

From figure 4.20(a), R sensors can be seen to have a small variation as a function of R at about the 1 ADC count level. All clusters fall in the middle of the one and two strip clusters and follow the same pattern. This is to be expected as the signal is dominated by one and two strip clusters. When comparing this to the simulation, the shapes are different. For simulation there is a small rise in the MPV at the level of ~0.5 ADC counts. There also seems to be none of the rise and fall which is seen in the data.

The same plots have been made for Phi sensors, using hits with matching R positions. In the data plots, there appears to be structure which is not present in the simulation to the same degree. In the data plot it is possible to distinguish the inner and outer regions easily. There is a small kink in the MC it is not as clear. Looking at the position of the all cluster points in relation to the one and two strip, both data and MC show a larger influence of one strip clusters than two. This agrees with the proportions of one and two strip clusters observed in R and Phi sensors.

Due to the design of the strips in the Phi sensor, there are a couple of additional plots that should be considered. Phi sensors have two distinct regions, inner and outer. The outer region has two types of strips, one with routing lines running over them and ones that are clear. Earlier test beams have found that there is a difference in both signal and noise levels in these two outer categories. Therefore their individual responses have been examined and the same plots are shown for both data and MC. For the simulation, Phi sensors used constant values for the noise and the same values for each of the three categories. There is a clear difference in the phi data and MC plots, where the simulation does not compensate for the difference in noise levels of the outer even and odd strips.

Conclusion

Section 4.5.2 shows the change in MPV for R and Phi sensors at different radii and for clusters formed with one and two strips. It shows that there are differences between MC and data, though these differences are small and come largely from the description of capacitance in the simulation. The changes in the R sensor are at the right level but show none of the structure that data does. The Phi sensors

show the correct scaling but fail to describe the effect of the routing line in the Phi sensors. All these effect are at a small level and do not represent significant deficiencies with the simulation.

4.5.3 Noise Monitoring

Noise can be classified as the ADC counts induced when there is no particle passing through the sensor. There are many ways that noise can enter the VELO system as specified in Section 4.3.4. With optimally functioning algorithms, the only remaining noise will be from the silicon itsself. This noise increases as a function of capacitance, which relates to the pitch, strip width and strip length. The full relation can be found in [57]. For VELO sensors, the noise is also affected by the readout lines, as they are not identical. This gives rise to larger variations in the noise.

To monitor the noise there are two different conditions from which data is taken;

- with no beam and a consecutive set of forced triggers to the TELL1;
- during normal operation one sensor in every few thousand events is read out in NZS mode and used for noise analysis.

For the purpose of the following analyses, only noise runs taken with no beam are used. This has the obvious benefit that the number of strips containing hits from particles traversing the sensors should be negligible and should therefore give a better measure of the noise of the system.

This is not always the case for data taken during collisions, even once the algorithm was improved [58].

From data taken for specific noise runs, the noise can be plotted for each of the strips in a sensor. Figure 4.23 shows the noise in both the R and Phi sensors as a function of strip number. In the R sensors the noise increases as with strip number in sections of 512 strips. This corresponds to the four regions of the R sensors, going from small radius to large and small strip lengths to larger.

4.5.4 Signal to Noise

Signal to noise is used as a measure for the reliability of the working of a sensor.. Noise is defined as ADC counts, induced in a sensor with no particle passing through. Signal to noise is defined as the MPV of a strip, using one strip clusters, divided by the RMS noise in that strip. Noise is calculated on a strip by strip basis for each sensor. To calculate the noise, NZS data is required. This is obtained in two different ways:

- from special NZS runs with 5000 triggers sent to the TELL1s when there is no beam;
- using the round robin data, this is when a trigger is randomly sent to one of the VELO sensors to dump its NZS data while there is normal data taking conditions with beam and collisions.

In the case of round robin data, it is harder to assess weather ADC counts come form signal or noise. To try to reduce this effect, a cut on the ADC counts is put on the strips used to measure the noise.

Although this should remove most of the noise in strips, it is not 100% effective, as it is difficult to account for strips which have below threshold signals.

Therefore, for the signal to noise analysis, strip noise is taken to be the noise from the dedicated NZS runs. The noise values are used for one strip and, because of this, the signal used is for one strip clusters only. An angular correction to these tracks has also been applied as described in section 4.5.1.

To measure signal to noise, the signal in individual strips is divided by the noise in that strip. Only single strip clusters have been used, as it gives a simpler definition of the signal-to-noise. Tracks with low angles have been used as there will be less charge sharing with the adjacent strips. Figure 4.5.4 shows the signal-to-noise for R and Phi sensors. The Phi sensors have been split into three different regions. This is because the routing lines that run along the odd strips in the outer region of the Phi sensors, have a larger amount of noise. This translates to a reduced signal-to-noise ratio in the odd phi strips. Table 4.1 shows the signal-to-noise for each of the four sections of sensors. It shows that Phi sensors have a larger signal-to-noise than the R sensors. It is clear that there is a difference in the three regions of the Phi sensor, where the inner lies between the outer odd and even.

Region	MPV
R	18.33
Phi Inner	21.23
Phi Odd	19.63
Phi Even	23.34

Table 4.1: The MPV for plots shown in figure 4.5.4.

Conclusion

The signal-to-noise has been measured in the R and Phi sensors looking at one strip clusters. Table 4.1 summarises the results for each of the different regions and confirms the previously measured effect, caused by the larger noise in the phi strips with routing lines. This is another parameter which needs to be considered in the running of the detector, because signal decreases with radiation damage and noise also increases with radiation damage.

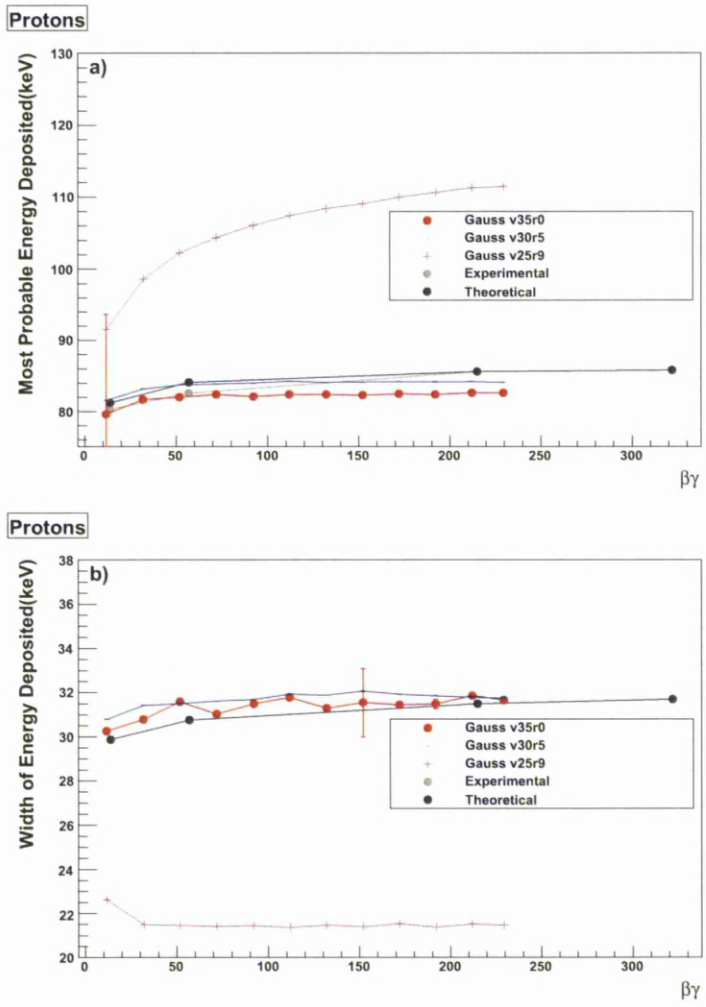

Figure 4.12: Results from fits to energy deposition in silicon for a range of $\beta\gamma$ containing protons and anti-protons. a) MPV of the energy deposited b) FWHM of the energy deposited.

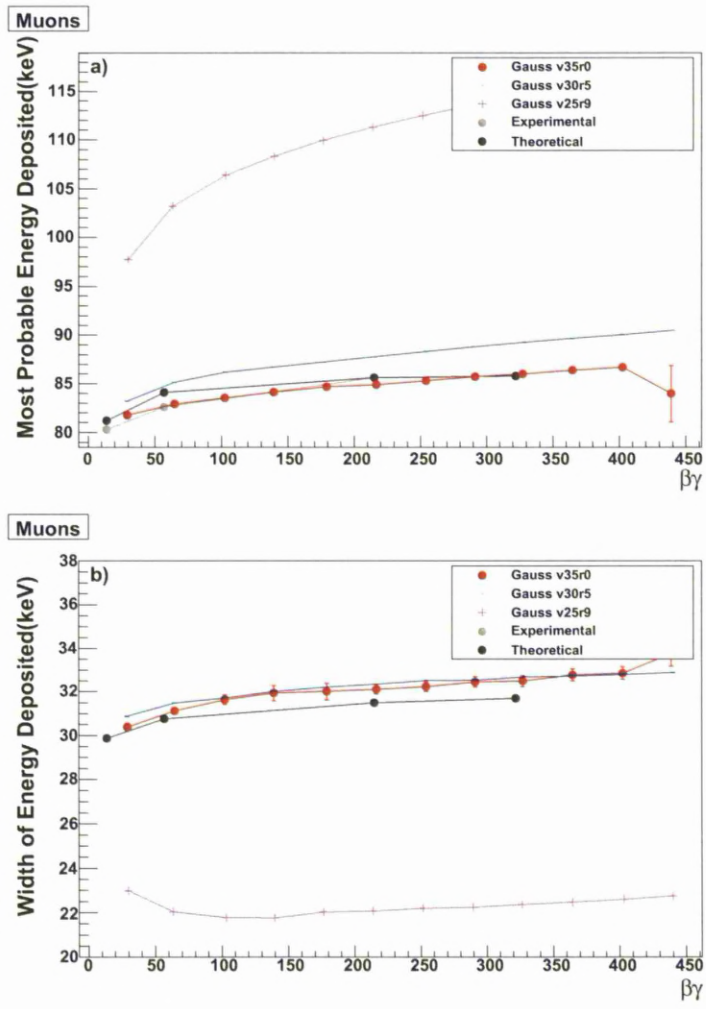

Figure 4.13: Results from fits to energy deposition in silicon for a range of $\beta\gamma$ containing muons and anti-muons. a) MPV of the energy deposited b) FWHM of the energy deposited.

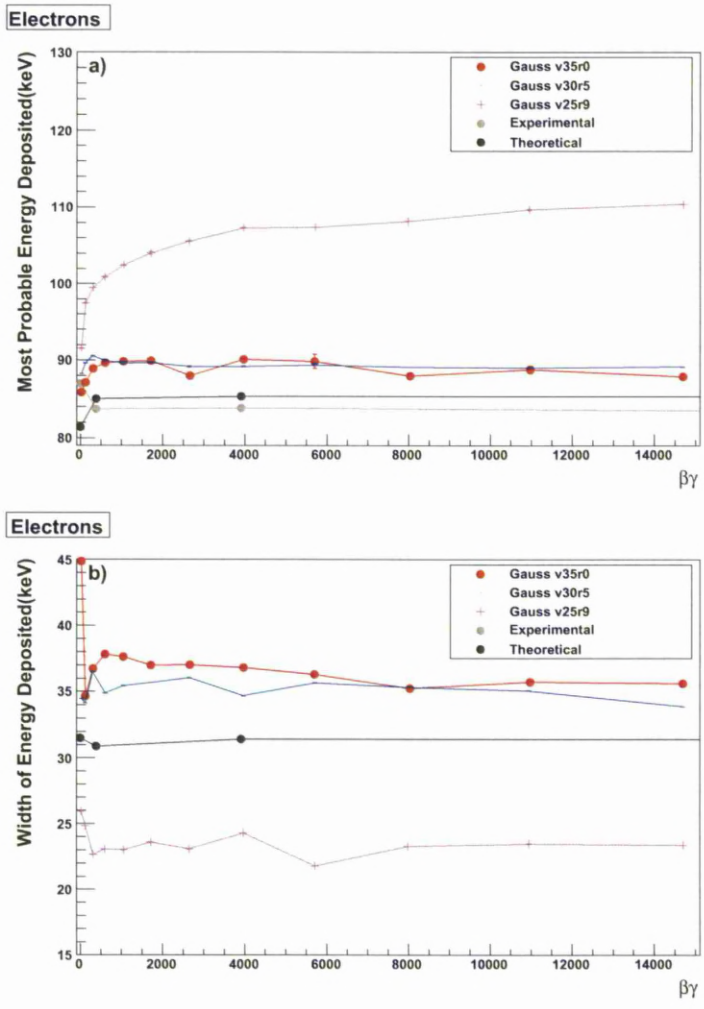

Figure 4.14: Results from fits to energy deposition in silicon for a range of $\beta\gamma$ containing all particle types. a) MPV of the energy deposited b) FWHM of the energy deposited.

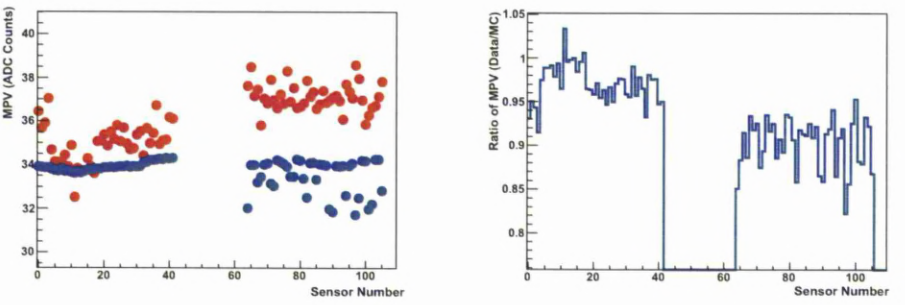

(a) (b)

Figure 4.15: MPV of Landaus fitted for each sensor in the VELO. 2010 data is plotted in red and 2010 MC is plotted in blue. Sensors 0-42 are R sensors and 64-103 are Phi sensors.

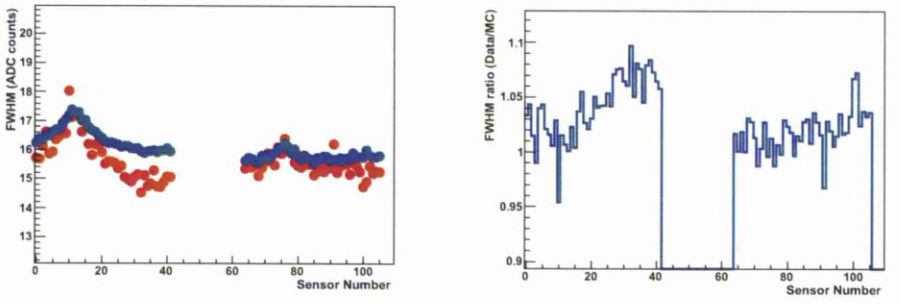

(a) (b)

Figure 4.16: FWHM of Landaus fitted for each senor in the VELO. 2010 data is plotted in red and 2010 MC is plotted in blue. Sensors 0-42 are R sensors and 64-103 are Phi sensors.

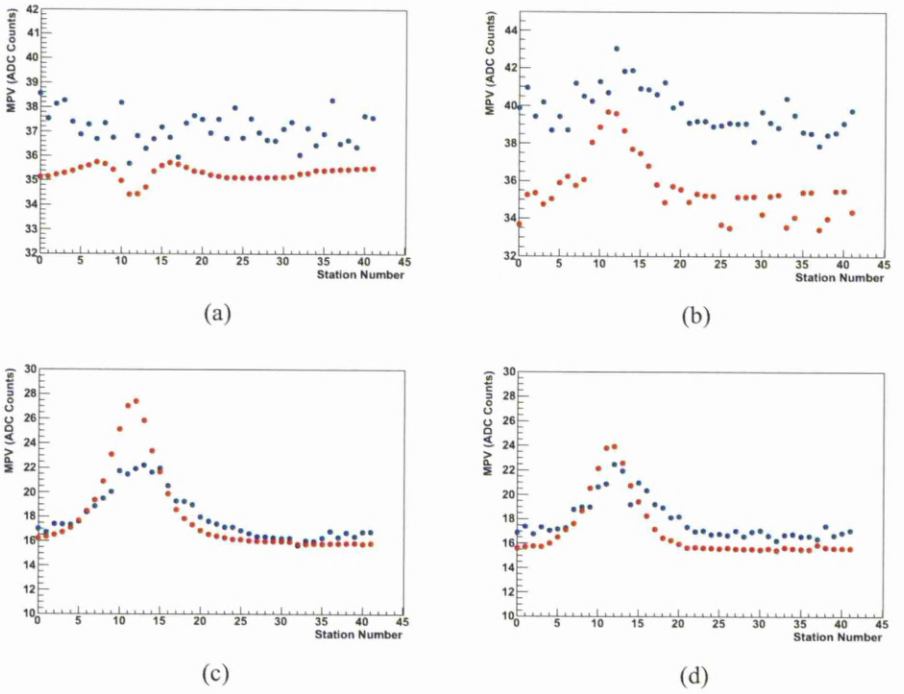

Figure 4.17: (a and b) MPV vs station number for R(a) and Phi(b) sensors using raw clusters. (c and d) FWHM vs Station number for raw clusters for R(c) and Phi(d) sensors. With MC in red and data in blue.

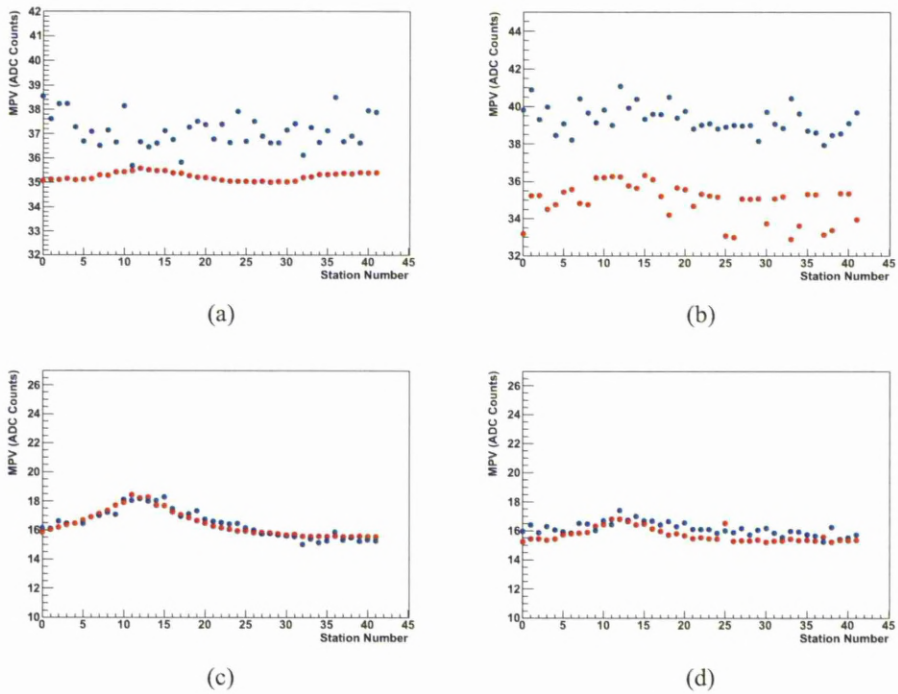

Figure 4.18: a and b) MPV vs station number for R(a) and Phi(b) sensors using tracks. c and d) FWHM vs Station number for tracks for R(c) and Phi(d) sensors. With MC in red and data in blue.

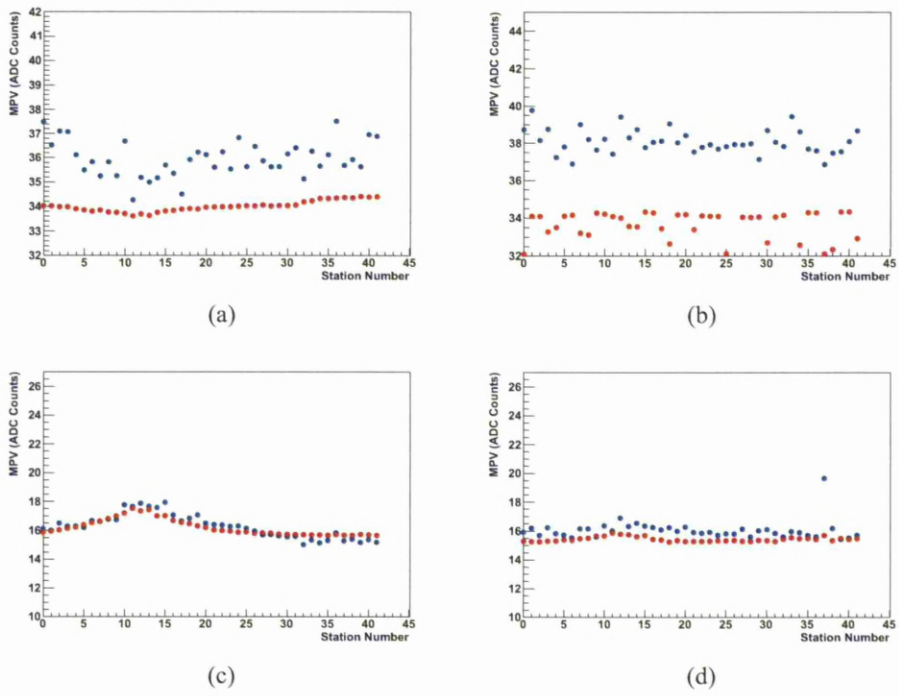

Figure 4.19: a and b) MPV vs station number for R(a) and Phi(b) sensors using angle corrected tracks. c and d) FWHM vs Station number for angle corrected tracks for R(c) and Phi(d) sensors. With MC in red and data in blue.

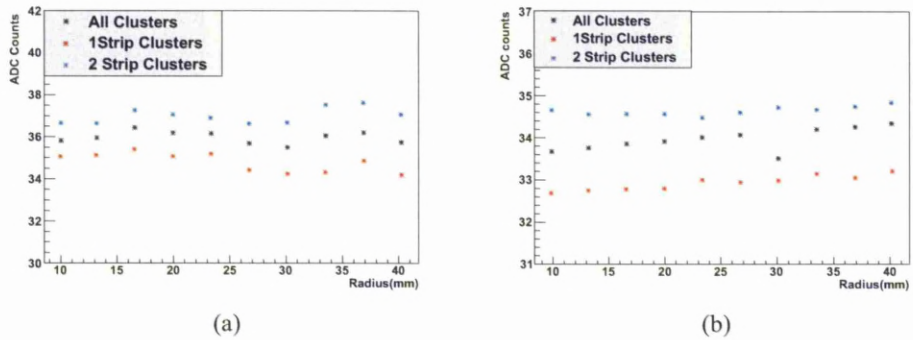

Figure 4.20: MPV vs radius for R sensors with 2010 data(a) and MC2010(b). Comparing for 1 and 2 strip clusters.

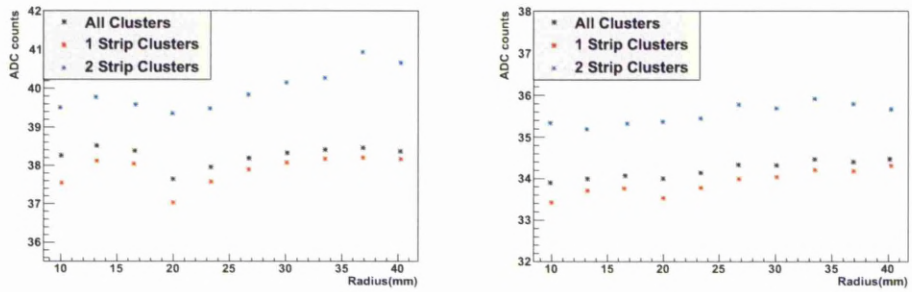

(a) (b)

Figure 4.21: MPV vs radius for Phi sensors with 2010 data(a) and MC2010(b). Comparing for 1 and 2 strip clusters.

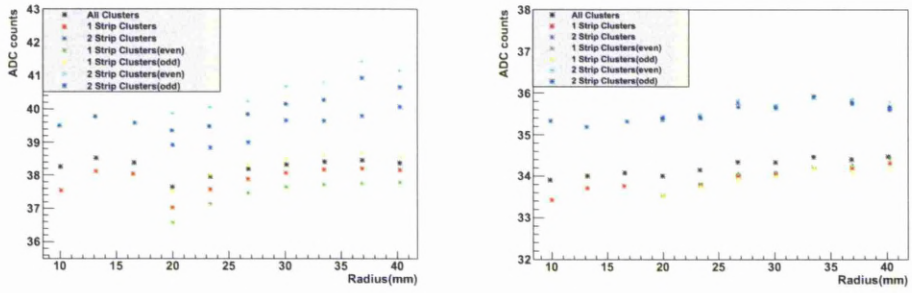

(a) (b)

Figure 4.22: MPV vs radius for Phi sensors with 2010 data. Comparison of 1 and 2 strip clusters, showing the difference in odd and even seed strips in these clusters.

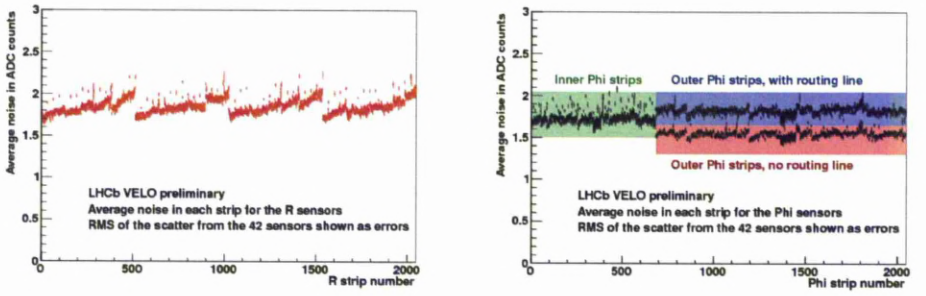

(a) (b)

Figure 4.23: Noise as a function of strip number for R(a) and Phi(b) sensors. Noise increases in the R sensors as a function of radius. In the Phi there are three different regions: inner, outer odd(with a routing line) and outer even(no routing line) [21].

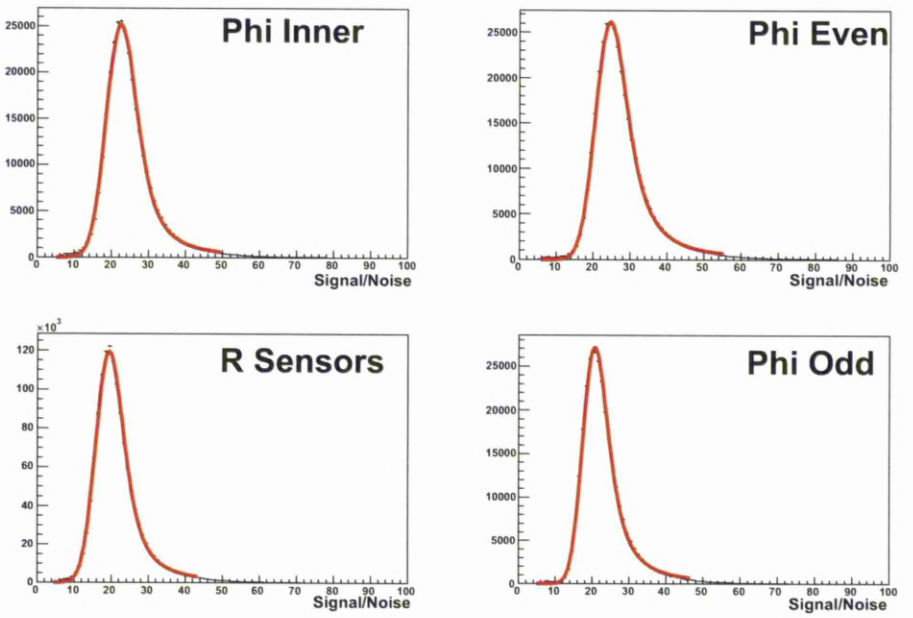

Figure 4.24: The MPV/noise for one strip clusters in the four different strip conditions.

Chapter 5

Analysis

5.1 Introduction

This chapter describes the reconstruction of B_s^0 mesons decaying to $D_s^+ D_s^-$ in LHCb. A summary of the decay is given, followed by a discussion of previous results. The reconstruction process in LHCb is then explained and its performance is compared to experiences with Monte Carlo. The cuts applied to data are discussed and the performance with 2010 data is shown.

5.2 $B_s^0 \rightarrow D_s^{\pm} D_s^{\pm}$

This section looks at the decay of B_s^0 mesons to D_s^+ and D_s^-. The main Feynman diagram for $B_s^0 \rightarrow D_s^+ D_s^-$ is shown in Figure 5.1. Each of the D_s^+ particles can then decay to $K^+K^-\pi^+$ and with the charge conjugate decay. They can also decay

through resonant states. The Feynman diagrams for the most common of these decays are shown in Figure 5.2.

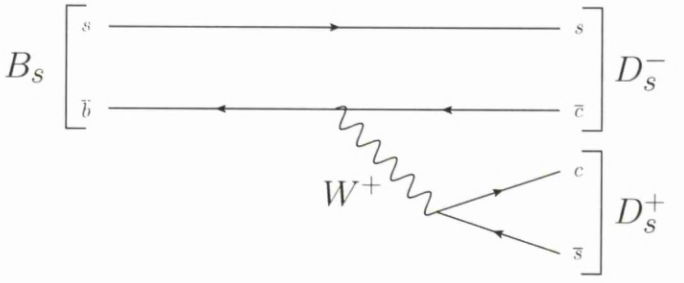

Figure 5.1: Feynman diagram for $B_s^0 \to D_s^+ D_s^-$

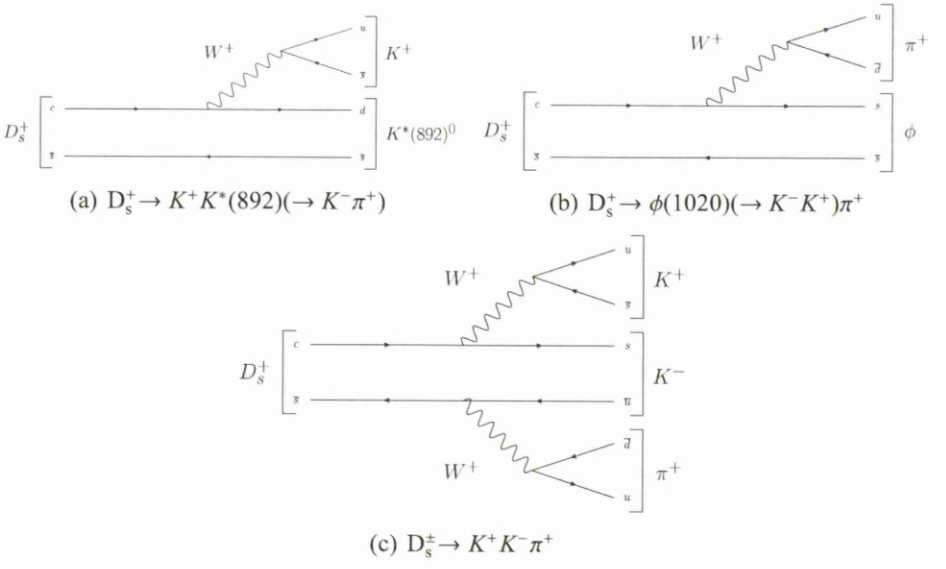

(a) $D_s^+ \to K^+ K^*(892)(\to K^-\pi^+)$

(b) $D_s^+ \to \phi(1020)(\to K^- K^+)\pi^+$

(c) $D_s^\pm \to K^+ K^- \pi^+$

Figure 5.2: Feynman diagram for the main modes of $D_s^\pm$decay.

This analysis discusses the way the decay of $B_s^0 \to D_s^\pm(KK\pi) D_s^\pm(KK\pi)$ is reconstructed and what results can be taken from the 2010 LHCb data. The B_s^0 meson can also decay through the excited $D_s^\pm$ meson, with either one or two $D_s^{*\pm}$ mesons replacing the $D_s^\pm$ meson. The $D_s^{*\pm}$ particle decays to either a $D_s^\pm \pi^0$ (6%) or $D_s^\pm \gamma$ (94%). It is possible to have decays containing one or two $D_s^{*\pm}$ particles and,

when these occur, the $D_s^{\pm}$ is reconstructed as usual. The additional π^0 or γ is not reconstructed as part of the decay.

5.3 Theory

This decay is of interest to study, as it is possible to make measurements of the mass difference and the decay width difference between the two mass eigenstates of the B_s^0 system, B_s^L and B_s^H. The $B_s^0 \to D_s^{\pm} D_s^{\pm}$ decay is a pure CP even state. The $D_s^{*\pm}$ states are also expected to be predominantly CP even. These three decay modes provide the largest contribution to $\Delta\Gamma_s/\Gamma_s$ [37, 38, 40], which is the difference in the decay width between the two mass eigenstates B_L and B_H, divided by the decay width. $\Delta\Gamma_s/\Gamma_s$ can be found using equation 5.1:

$$\frac{\Delta\Gamma_s}{\Gamma_s} \simeq \frac{2\mathrm{BR}(B_s \to D_s^{(*)+} D_s^{(*)-})}{1 - \mathrm{BR}(B_s \to D_s^{(*)+} D_s^{(*)-})} \tag{5.1}$$

$\mathrm{BR}(B_s \to D_s^{(*)+} D_s^{(*)-})$ represents the branching fraction for all three of the decay modes. The current values are shown in table 5.13. Equation 5.1 comes from using the heavy quark limit and requires that the mass and CP-eigenstates coincide. For a more complete explanation see [39, 40]. Equation 5.1 has been used in previous measurements [38, 41, 42, 43].

5.4 Previous Measurements

Since the B_s^0 mass was first measured in 1993 [59] there has been great interest in studying other properties such as decay modes, mixing and CP violations similar

to those of the B^0, which had been measured. In 2006 oscillations in the B_s^0 system were first observed by the CDF experiment[60].

B_s^0 decays to $D_s^+ D_s^-$ were first observed in 2008 by CDF [43]. This measurement did not consider the cases with $D_s^{*\pm}$ in the decays. It found an absolute branching ratio of $(0.94^{+0.44}_{-0.42})$ %. Since then, an additional measurement from Belle [61] has also been made and, when combined, a world average of $(1.04^{+0.29}_{-0.26})$ % has been found [3].

Belle was able to extract the photons from the $D_s^{*\pm}$ states. As such it was possible to make individual measurements of the branching ratios of both the $D_s^{*\pm} D_s^{\mp}$ and the $D_s^{*\pm} D_s^{*\mp}$. Belle found them to be $(2.8^{+0.8}_{-0.7}(\text{stat.}) \pm 0.7(\text{syst.}))$ % and $(3.1^{+1.2}_{-1.0}(\text{stat.}) \pm 0.8(\text{syst.}))$ % respectively [41].

The results from Belle, CDF and D0 have been used to make measurements of $\Delta\Gamma_s^{CP}/\Gamma_s$ giving $14.7^{0.036}_{-0.030}(stat.)^{+4.4}_{-4.2}(syst.)$%, (12^{+9}_{-10})% and (7.2 ± 3.0)% respectively [41, 42, 43].

5.5 Event Selection

This section explains the selection cuts that were applied to events. The selection process consists of:

- preselection: a loose selection to remove different signal modes and some backgrounds;
- selection: a tighter selection which further reduces the backgrounds.

These cuts are discussed in the later sections.

5.5.1 Preselection

For this analysis, an initial loose selection of events was made. This selection is intended to reduce the amount of data processed by the experiment. These cuts can be characterised as cuts on reconstructed particles and cuts applied to the final state particles. That is, cuts applied to the B_s^0 and $D_s^{\pm}$ particles or to the final state Kaons and Pions.

Kaon and Pion cuts

The common cuts on kaons and pions will now be discussed. These particles form the track used to reconstruct the B_s^0 and $D_s^{\pm}$. The cuts focus more on the properties of the tracks and the identification of the pion or kaon.

The kaons and pions are required to have a momentum greater than 2 MeV; a transverse momentum(P_T) greater than 0.2 MeV; an IP χ^2 relative to the $D_s^{\pm}$ less than 6.25 and the tracks must have a χ^2 less than 5.

There is an additional cut on the pion. This is on the PID, where a difference of the log likelihood between the assumption a particle is a pion, and the assumption a that same particle is a kaon, is less than 12.

$D_s^{\pm}$ Cuts

The cuts placed on the reconstructed $D_s^{\pm}$ will now be discussed. A candidate $D_s^{\pm}$ must have a reconstructed mass in the range from the mass of a D^+-100 MeV to the mass of the $D_s^{\pm}$ +100 MeV. The distance of closest approach (DOCA) between any pair of particles must be smaller than 0.4 mm. The $D_s^{\pm}$ will have a P_T greater than 1.1 MeV. The IP from the $D_s^{\pm}$ to the PV will be greater than 0.07 mm and a χ^2 greater than 10. The DIRA between the $D_s^{\pm}$ and the PV must be greater than 0.99. The $D_s^{\pm}$ must have a vertex χ^2 greater than 8. A vertex separation χ^2 between the PV and the $D_s^{\pm}$ must be greater than 36. The vertex separation χ^2, in the Z plane, between the PV and the $D_s^{\pm}$ must be greater than 2. The distance from the $D_s^{\pm}$ decay vertex to the related primary vertex must be greater than 0.1 mm. The cuts on the IP relative to the to PV reduces background from $D_s^{\pm}$ particles from the PV.

B_s^0 Cuts

A candidate B_s^0 must have a reconstructed mass in the range starting at 300 MeV below the B^0 mass and running to 300 MeV above the B_s^0 mass. This is used to reduce the number of events from backgrounds such as combinatorics which have a larger effect at lower energies. The impact parameter (IP) of the B_s^0 relative to the primary vertex (PV) must be smaller than 0.15 mm, with a χ^2 less than 16. The cosine of the angle between the momentum of the B_s^0 particle and the direction of flight from the best PV to the decay vertex (DIRA) must be greater than 0.99994. The reconstructed B_s^0 vertex must have a χ^2 less than 6. The B_s^0 and $D_s^{\pm}$ vertex separation has a χ^2 less than 2. The separation between the B_s^0 vertex and the PV in the Z plane must be less than 2 mm. The separation between the B_s^0 vertex and the $D_s^{\pm}$ vertex in the Z plane must be greater than -1 mm. A distance from the

decay vertex of the B_s to the PV must be greater than 0.1 mm.

For the B_s^0, the cuts on the vertex and IP ensure that the B_s^0 come from the PV and are distinct from the $D_s^{\pm}$. A Z separation greater than -1 mm between the B_s^0 and $D_s^{\pm}$ requires the $D_s^{\pm}$ to be produced in a forward direction.

All of these cuts are summarised in table 5.1. These cuts have been used as the baseline for much of this analysis.

5.5.2 Selection

The preselection described in section 5.5.1 is designed to provide a loose selection containing most of the desired signal. As a result it also contains a larger number of background events. Additional selection criteria are applied to enhance the signal. This selection will now be discussed, and is summarised in table 5.2.

The first column shows the variable which is cut on. The second is the condition of the cut and the third shows the values used in the selection. The fourth and fifth relate to a tightening of loosening of the cuts, which will be discussed later in section 5.10.2 to assess systematic errors. The ghost probability of a track comes from the output of a neural net and uses multiple variables to decide on the quality of the track.

The cosine of the angle between the momentum of the B_s^0 particle and the direction of flight from the best primary vertex (PV) to the decay vertex (DIRA) must be greater than 0.999975. The total number of candidate PV in an event must be less than 5, to reduce the effect from multiple interactions. The impact parameters χ^2 of the B_s^0 to the PV must be less than 20. The impact parameters

Cuts		Value
B_s Mass Window	=	300 MeV
B_s IP to PV	<	0.15 mm
B_s IP χ^2 to PV	<	16.0
B_s DIRA	<	0.99994
B_s Vertex χ^2	<	6
B_s Vertex Separation χ^2	<	2
B_s Z Vertex Separation	<	2 mm
B_s to D_s Vertex Separation	>	-1 mm
Distance from B_s end vertex to PV	>	0.1 mm
D_s Mass Window	=	100 MeV
D_s Distance of closest approach (DOCA)	<	0.4 mm
D_s PT	>	1.1 MeV
D_s IP to PV	>	0.07 mm
D_s IP χ^2 to PV	>	10.0
D_s DIRA	<	0.99
D_s Vertex χ^2	<	8
D_s Vertex Separation χ^2	<	36
D_s Z Vertex Separation χ^2	<	2
Distance from D_s end vertex to related primary vertex	>	0.1 mm
K and π P	>	2 MeV
K and π P	>	500 MeV
K and π PT	>	0.2 MeV
K and π IP χ^2	<	6.25
K and π Track χ^2	<	5
π ΔLL	<	12

Table 5.1: Table of the cuts used in the preselection. These relate to the trigger line B2DDLineLoose. Here PV stands for primary vertex, DIRA stands the direction angle, the cosine of the angle between the momentum of the particle and the direction of flight from the best PV to the decay vertex. PV stands for the primary vertex, P is the momentum and PT is the momentum in the transverse plane. DOCA is the distance of closest approach between two particles.

χ^2 of each of the $D_s^{\pm}$ candidates to the PV must be greater than 20. The pions and kaons have an impact parameter χ^2 to the PV greater than 16. All tracks will have a ghost probability less than 0.5 .

A selection of these variables are shown in figures 5.3, 5.4 and 5.5. They show

Cuts 1			Scaled 0.9	Scaled 1.1
Cut		Number	Number	Number
Bs DIRA PV	>	0.999975	0.9999775	0.9999725
total number of candidates	<=	4	3	5
Bs IPχ^2 PV	<	20.	18.0	22.0
Ds IPχ^2 PV	>	20.0	22.0	18.0
Kaon IPχ^2 PV	>	15.0	13.5	16.5
Pion IPχ^2 PV	>	15.0	13.5	16.5
Kaon Track Ghost Probability	<	0.5	0.45	0.55
Pion Track Ghost Probability	<	0.5	0.45	0.55

Table 5.2: Selection used to remove background and leave signal. The scaled values are used in section 5.10 to estimate the systematic errors.

the MC and data for some of the variables. They split the MC into signal and background, which has been used to demonstrate the effectiveness of the cuts. These are then combined into a MC sample to be compared with the data. This enables an assessment of the quality of the simulation and of how reliable a particular cut may be.

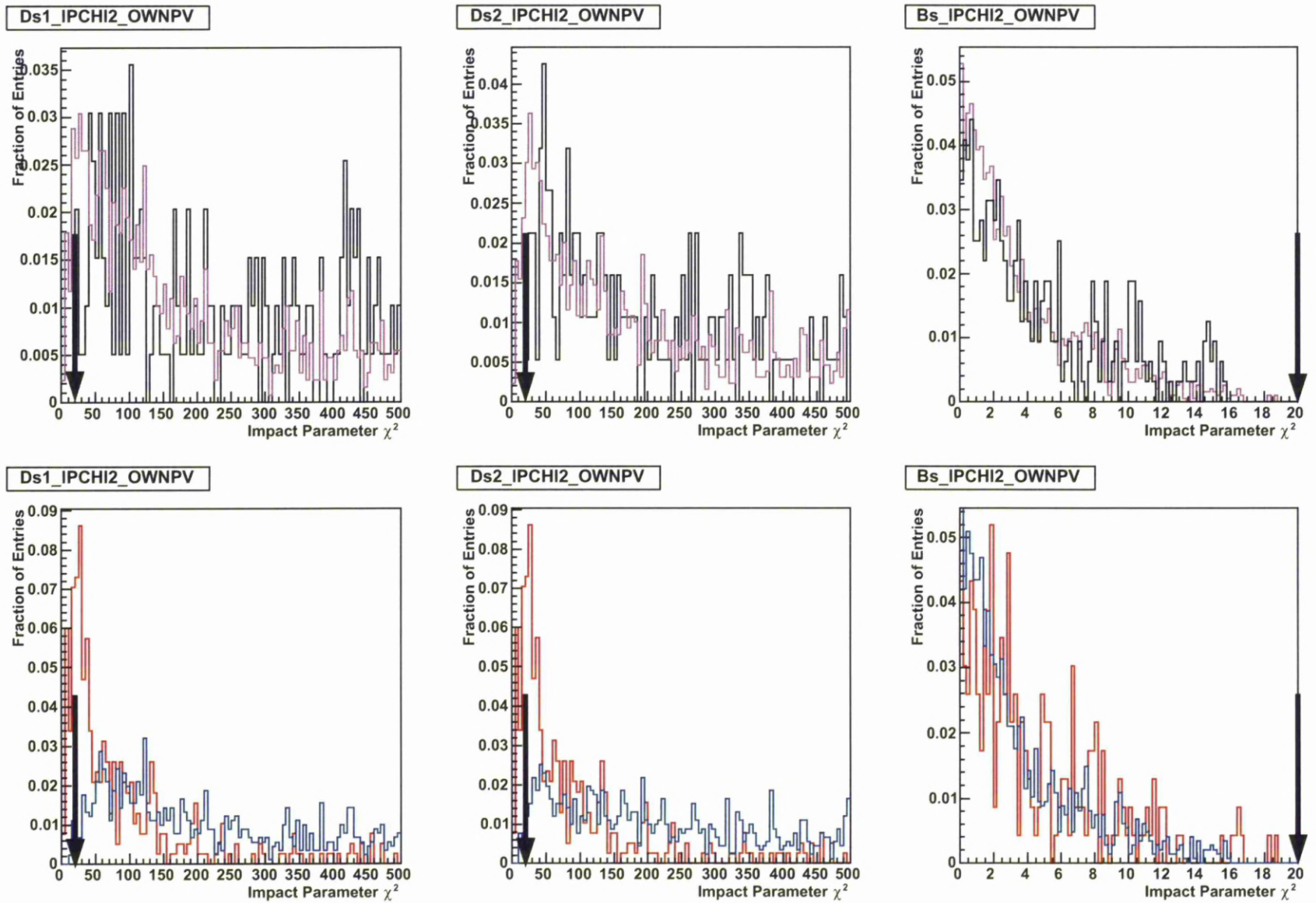

Figure 5.3: Impact parameter χ^2 for the B_s^0 and the two $D_s^{\pm}$ particles. Signal (Blue), Background (Red), MC2010 (Magenta) and Data (Black).

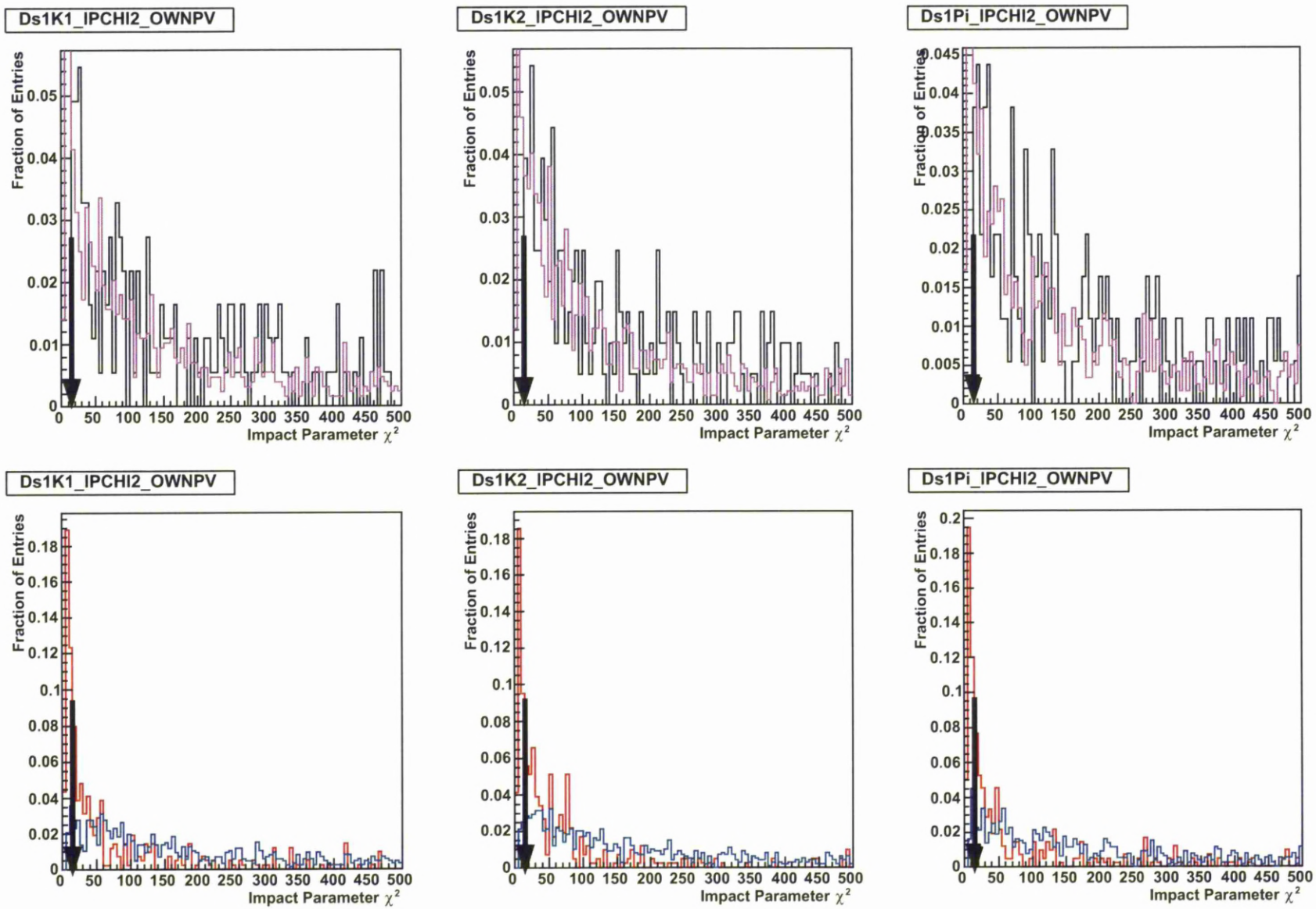

Figure 5.4: Impact parameter χ^2 for the daughters of the $D_s^{\pm}$ particle. Signal (Blue), Background (Red), MC2010 (Magenta) and Data (Black).

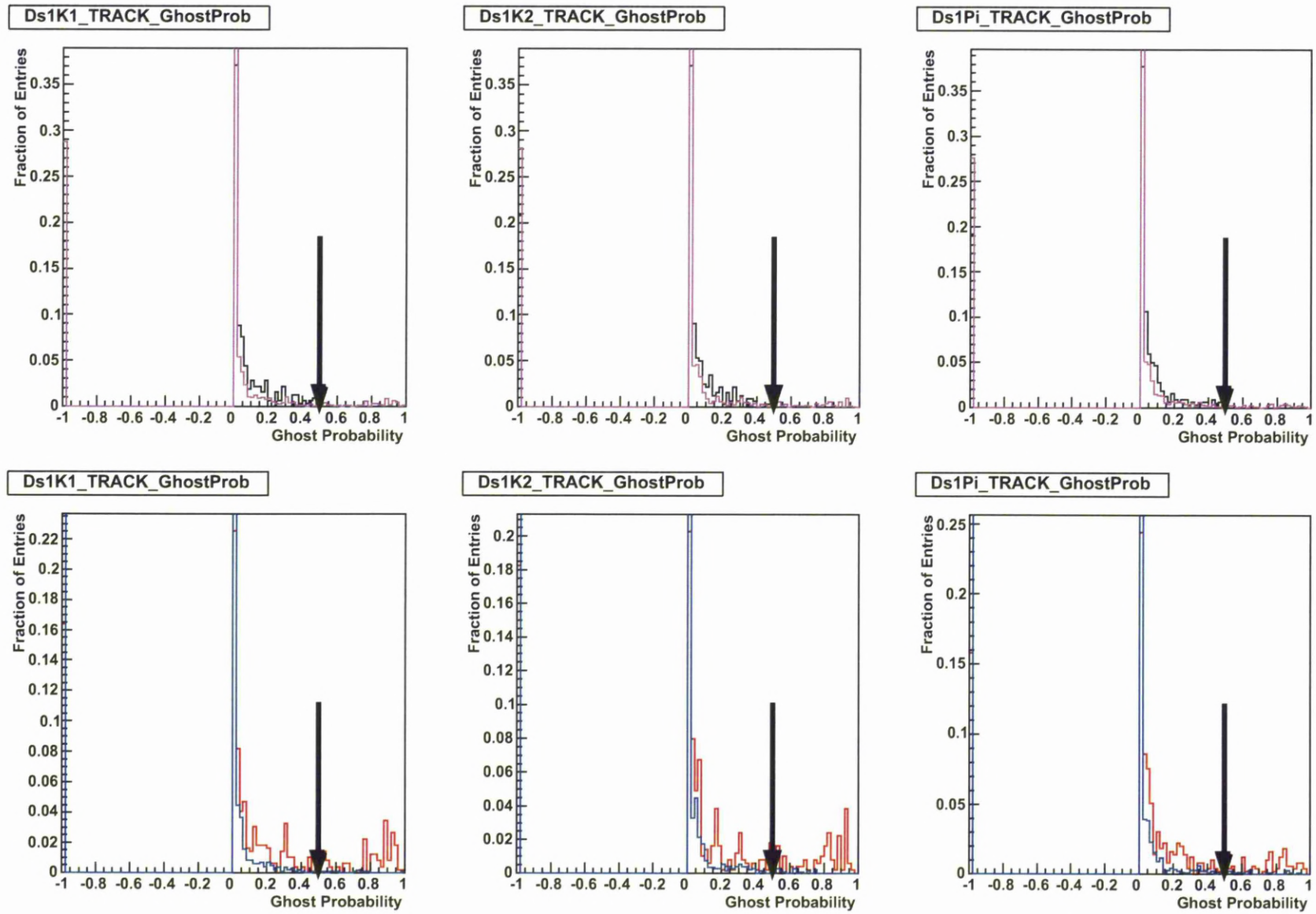

Figure 5.5: Ghost probability of a track calculated using a neural net, where a value of -1 was found this means that no decision was made. Plots for the Kaons and Pions from one $D_s^{\pm}$ particle are shown. Signal (Blue), Background (Red), MC2010 (Magenta) and Data (Black).

5.5.3 Cut Flow

Table 5.3 shows the effect that each of the cuts applied has on the different signal categories and the background in MC. The number of events passing through data is also shown. Figure 5.6 shows the efficiencies from table 5.3 . The response of the data to the cuts follows more closely the shape of the background MC. This suggests that the data is dominated by background events, particularly before the cuts on the $D_s^{\pm}$ mass. By comparing the slope in signal and background MC samples, the effectiveness of the cuts can be seen. The final efficiency for each from all the cuts can be seen in the final row table. The final efficiency, as estimated from MC, of the $B_s \to D_s^{(*)} D_s^{(*)}$ decays is ~74% and for the background about 9%. The first eight cuts provide the largest reduction in the background. These cuts consist of mass cuts on the B_s^0 and $D_s^{\pm}$ and the number of candidates in an event.

Figure 5.6 also suggests that the data is dominated by background in the early set of cuts.

		Data		Monte Carlo							
	Cuts	No. Data	Efficiency Data	No. DsDs	Efficiency DsDs	No. Ds*Ds	Efficiency Ds*Ds	No. Ds*Ds*	Efficiency Ds*Ds*	No. Bkg	Efficiency Bkg
	Uncut*	-	-	38250	-	30000	-	49998	-	32004320	-
	B2DDLineLoose	10030	-	6992	-	4306	-	8121	-	652	-
1	Bs Mass>4979	5574	1.000	428	1.000	404	1.000	331	1.000	652	1.000
2	Bs Mass<5667	5574	1.000	428	1.000	404	1.000	331	1.000	652	1.000
3	Bs DIRA PV>0.999975	4293	0.770	419	0.979	394	0.975	323	0.976	434	0.666
4	Ds1 MM>1900	3736	0.670	414	0.967	386	0.955	319	0.964	384	0.589
5	Ds1 MM<2020	2710	0.486	409	0.956	384	0.950	316	0.955	298	0.457
6	Ds2 MM>1900	2385	0.428	399	0.932	377	0.933	313	0.946	264	0.405
7	Ds2 MM<2020	1690	0.303	397	0.928	373	0.923	310	0.937	210	0.322
8	Total Candidates<=4	1582	0.284	397	0.928	373	0.923	310	0.937	120	0.184
9	Bs IPχ^2 PV<20	1582	0.284	397	0.928	373	0.923	310	0.937	114	0.175
10	Ds1 IPχ^2 PV>20	1504	0.270	393	0.918	370	0.916	306	0.924	114	0.175
11	Ds2 IPχ^2 PV>20	1429	0.256	391	0.914	367	0.908	305	0.921	114	0.175
12	Ds1K1 IPχ^2 PV>15	1230	0.221	379	0.886	359	0.889	293	0.885	104	0.160
13	Ds1K2 IPχ^2 PV>15	1057	0.190	370	0.864	352	0.871	283	0.855	98	0.150
14	Ds1Pi IPχ^2 PV>15	919	0.165	360	0.841	342	0.847	277	0.837	92	0.141
15	Ds2K1 IPχ^2 PV>15	838	0.150	347	0.811	331	0.819	265	0.801	84	0.129
16	Ds2K2 IPχ^2 PV>15	759	0.136	336	0.785	322	0.797	262	0.792	80	0.123
17	Ds2Pi IPχ^2 PV>15	715	0.128	330	0.771	315	0.780	254	0.767	74	0.113
18	Ds1K1 GP<0.5	669	0.120	328	0.766	312	0.772	253	0.764	72	0.110
19	Ds1K2 GP<0.5	627	0.112	328	0.766	308	0.762	251	0.758	70	0.107
20	Ds1Pi GP<0.5	597	0.107	327	0.764	304	0.752	249	0.752	66	0.101
21	Ds2K1 GP<0.5	555	0.100	324	0.757	300	0.743	246	0.743	64	0.098
22	Ds2K2 GP<0.5	523	0.094	321	0.750	295	0.730	244	0.737	62	0.095
23	Ds2Pi GP<0.5	501	0.090	315	0.736	293	0.725	244	0.737	58	0.089
24	clone_decision==0	456	0.082	301	0.703	259	0.641	236	0.713	58	0.089

Table 5.3: Shows the effectiveness of the cuts applied to each of the categories of the B_s^0 decays for both MC and data. Moving down the table, the cuts are added together to give the combined effect of all the cuts. The efficiencies are taken as relative to the stripping line AllB2DDLineLoose, with additional loose cuts on the $D_s^{\pm}$mass to improve speed. Clone decision is the removal of clones.

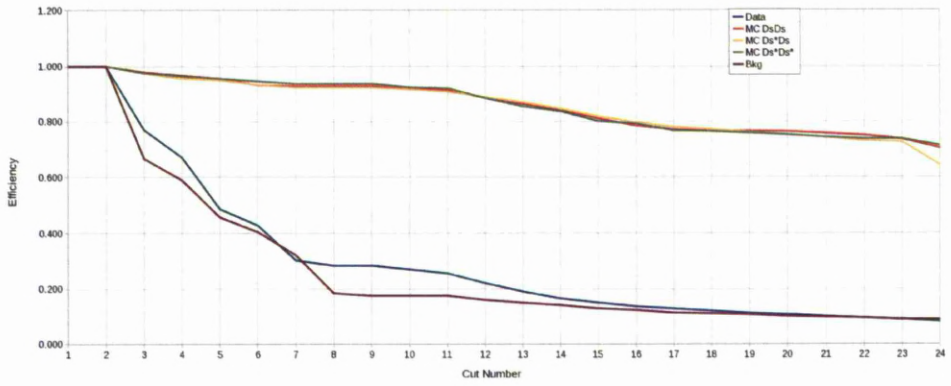

Figure 5.6: The remaining fraction of events present after each cut in the cut flow from table 5.3. Here the efficiencies have been scaled to the value at the first cut.

5.6 Backgrounds

The major backgrounds encountered are combinatorial and misidentification of pions or kaons. The first two backgrounds are reducible in several ways. For example, by adding stricter conditions on the tracks, one can reduce the number of acceptable tracks available for the combinatorial background. Tighter PID restrictions help to reduce both the miss ID fraction and the effect of clones.

5.7 D_s^* Decays

B_s^0 can also decay to $D_s D_s^*$ or $D_s^* D_s^*$. The D_s^* is tougher: the typical decay modes of the D_s^* are $D_s\gamma$ and $D_s\pi_0$ with a mass difference of 143.8 ± 0.4 MeV to the $D_s^{\pm}$. Therefore, the reconstructed $D_s^{\pm}$ is real but the B_s^0 found is missing energy. The result is that larger mass windows are required correctly to model the background

from these modes. It is possible to separate the B_s^0 to D_s^+ D_s^- decay from the different D_s^* cases. Separating events with one or two D_s^* is a much greater challenge, as the region of overlap is larger.

A fit model was constructed which fits each of the peaks from the $D_s^{*\pm}$ modes. Each part of the fit was tested on MC events and validated separately. These were then combined to one fit and assessed for biases.

5.7.1 Clones

Clones are classed as particles which have been used multiple times and are therefore double counted. LHCb has developed a common tool for removing these particles from analyses. This can arise from particles having more than one track associated with them. These could in many cases contain the same track hits. To supplement the clone tool, additional checks have been made. For each event checks have been made to ensure that the $D_s^{\pm}$ particles are not made from common tracks.

There are two cases where there can be additional clone particles and these are both treated differently:

1. a Kaon and pion are swapped. The ΔLog Likelihood(dLL) value for Kaon-Pion separation is used to choose the best candidate;
2. a different track is used, which has similar hits and trajectory. The track which has the smallest $\chi^2/n.d.o.f.$ for the track fit is chosen.

In the second case, the difference in the momentum of the track is often small.

5.8 Fit Procedure

This section discusses the process used to model and fit the data and the tests used to validate the fit. There are five main functions used in fitting to the different distributions. These are: Breit-Wigner, Voigtian, Gaussian and Chebychev polynomial. These are used to fit the $D_s^{\pm}$ mass and B_s^0 mass simultaneously.

5.8.1 Composition of the Fit

The fit combines information from the six final state charged tracks and performs an unbinned fit on the the reconstructed $D_s^{\pm}$ mass and the B_s^0 mass. A maximum likelihood fit is performed simultaneously on both the B_s^0 and $D_s^{\pm}$. First the fit model for the $D_s^{\pm}$ mass is discussed then the B_s^0 mass is discussed.

Reconstructing and Fitting the D_s mass

The $D_s^{\pm}$ mass is modelled with a peak and a polynomial background. A Breit-Wigner was chosen for the peak and a second order Chebychev polynomial for the background. The fitted model for the signal peak is described by:

$$\begin{aligned} S_{D_s}(M; p, g, a_1, a_2) &= \frac{s}{\mathcal{N}} \frac{1}{(M-p)^2 + \frac{1}{4}g^2} \\ &+ \frac{(1-s)}{\mathcal{N}} \left(1 + \sum_{i=0}^{2} a_i T_i(M)\right) \end{aligned} \tag{5.2}$$

where:

$$T_0(x) = 1 \tag{5.3}$$

$$T_1(x) = x \tag{5.4}$$

$$T_2(x) = 2x^2 - 1 \tag{5.5}$$

The first term is for the Breit-Wigner of the signal and the second is the Chebychev background model. $\mathcal{N}$ is a normalisation factor and s is the signal fraction. a_1 and a_2 are the parameters of the polynomial. Figure 5.7 shows this fit model used to fit data and MC. This fit is performed simultaneously with the fit to the B_s^0 which is discussed later in this section.

To be able to reconstruct the B_s^0 the starting point is to reconstruct the $D_s^{\pm}$ particles. The decay mode that has been chosen for this analysis is $D_s^{\pm} \rightarrow K^+K^-\pi^{\pm}$. This was chosen because of its relatively high branching ratio and because all the constituents of the $D_s^{\pm}$ are reconstructible. This decay can proceed through two main resonant states and the effect of these can be seen in figures 5.8 and 5.9 which show the Dalitz plot and the projection of this into the $K\pi$ and KK planes. These figures show the Dalitz and projection after the full selection has been applied for both data and MC.

Reconstructing and Fitting the B_s mass

The fit to the B_s^0 mass is more complex. It requires fits to decays with $D_s^{*\pm}$ particles as well as $D_s^{\pm}$. To understand the model that would best describe these decays the MC reconstruction distributions were used. Each of the following cases were considered; no $D_s^{*\pm}$, one $D_s^{*\pm}$ and two $D_s^{*\pm}$ particles. In each case a fit to the reconstructed true B_s^0 mass was made using four different peak models; Gaussian, Breit-Wigner, Crystal Ball and Voigtian. In each case the fit with the smallest χ^2 per degree of freedom was chosen. These fits were also used to set ranges for the fit parameters used and to provide some constraints on the fit for the two $D_s^{*\pm}$ case.

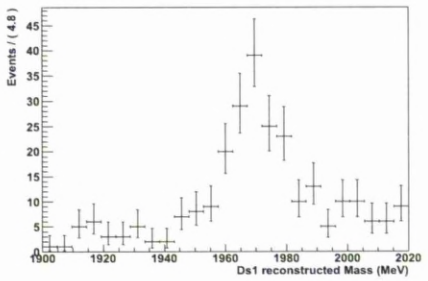

(a) Reconstructed D_s^+ mass peak from Data

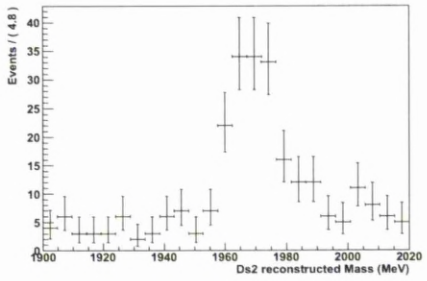

(b) Reconstructed D_s^- mass peak from Data

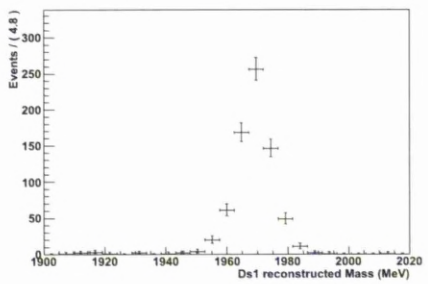

(c) Reconstructed D_s^+ mass peak from MC

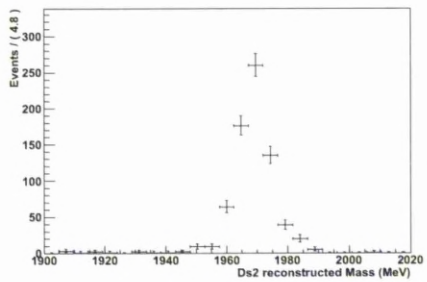

(d) Reconstructed D_s^- mass peak from MC

Figure 5.7: Reconstructed $D_s^\pm$ mass for Data and MC. There are two $D_s^\pm$ mass plots.

The final form of the fit was as follows:

$$\begin{aligned} S_{B_s}(M; p_1, s_1, g_1, p_2, s_2, p_3, s_3, a_i) &= \frac{n_1}{\mathcal{N}} \frac{1}{(M-p_1)^2+\frac{1}{4}g_1^2} \otimes \exp\left(-\frac{1}{2}\left(\frac{M-p_1}{s_1}\right)^2\right) \\ &+ \frac{n_2}{\mathcal{N}} \exp\left[-0.5\left(\frac{M-p_2}{s_2}\right)\right] \\ &+ \frac{n_3}{\mathcal{N}} \exp\left[-0.5\left(\frac{M-p_3}{s_3}\right)\right] \\ &+ \frac{n_4}{\mathcal{N}}\left(1 + \sum_{i=0}^{2} a_i T_i(M)\right) \end{aligned} \tag{5.6}$$

with:

$$n_1 + n_2 + n_3 = s \tag{5.7}$$

This uses a Gaussian to model the case of one $D_s^{*\pm}$ or two $D_s^{*\pm}$ particles in the decay. The peak of the $D_s^\pm$ only mode is modelled with a Voigtian and the back-

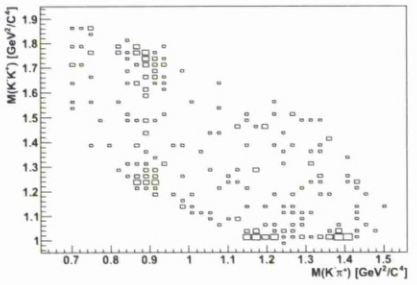

(a) Reconstructed $D_s^{\pm}$mass peak from Data

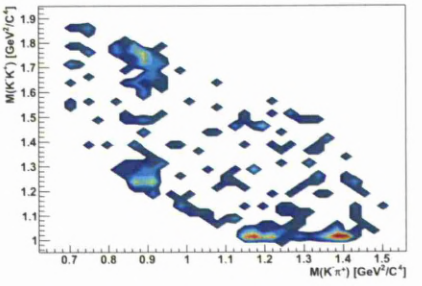

(b) Reconstructed $D_s^{\pm}$mass peak from Data

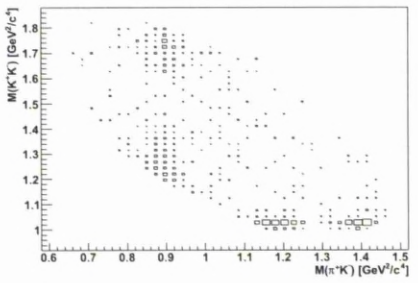

(c) Reconstructed $D_s^{\pm}$mass peak from MC

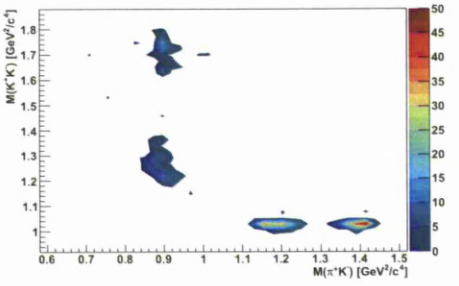

(d) Reconstructed $D_s^{\pm}$mass peak from MC

Figure 5.8: Dalitz plots of the $D_s^{\pm}$ for data and MC. Both plots are the same but use different styles. It is possible to see the resonant states which the $D_s^{\pm}$ can decay. The two main ones are the $K^*(892)$ (vertical band at ~892 MeV) and the $\phi(1020)$ (horizontal band at ~1020 MeV).

ground comes from an Chebychev polynomial, to account for the combinatoric background. The first term of equation 5.6 is the Voigtian, which describes the decay $B_s^0 \rightarrow D_s^{\pm} D_s^{\pm}$. The variables p_1, g_1 and s_1 are the parameters for the position of the peak Breit-Wigner and Gaussian; the width of the Breit-Wigner and the sigma of the Gaussian, which is convoluted with the Breit-Wigner. The second and third terms of the equation describe the Gaussian distributions fitted to the $B_s^0 \rightarrow D_s^{\pm} D_s^{*\mp}$and $B_s^0 \rightarrow D_s^{*\pm} D_s^{*\mp}$peaks. p_2 and p_3 are the variables for the peaks of the Gaussian distributions. s_2 and s_3 are the variables for the sigmas of the Gaussian distributions. The fourth parameter is the Chebychev polynomial, which describes the background, where T_i is described earlier, and a_i are the variables of

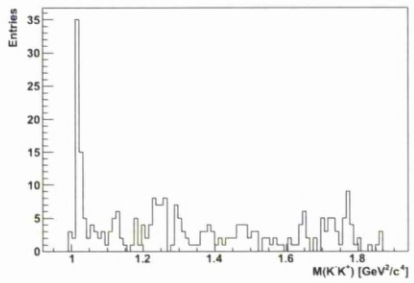

(a) Reconstructed mass of K^+K^- for data.

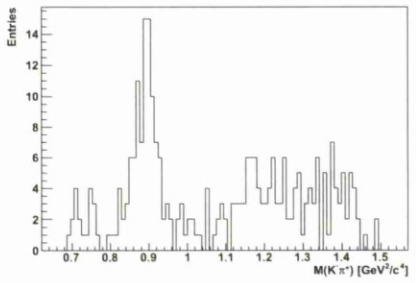

(b) Reconstructed mass of π^+K^- for data.

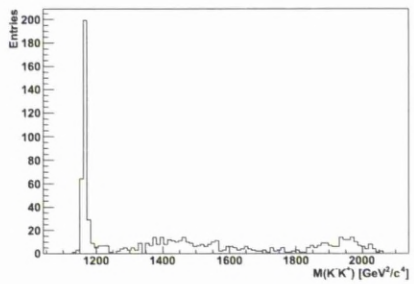

(c) Reconstructed mass of K^+ K^- for MC

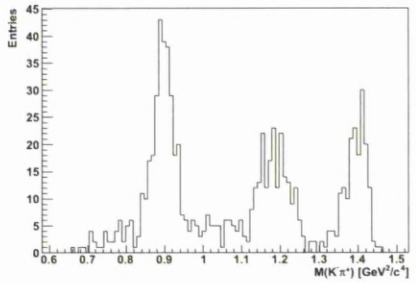

(d) Reconstructed mass of π^+ K^- for MC

Figure 5.9: Projections from the Dalitz plot for data and MC to show the $K^*(892)$ and $\phi(1020)$ resonances.

the polynomial. The n parameters are the fractions of the contribution from each component and s is the fraction of signal events from the $D_s^{\pm}$ fit.

The fit model for the B_s^0 mass is combined with the fit model for the $D_s^{\pm}$ mass, giving an 18 parameter fit. This number is reduced to 15 parameters by fixing the peak and width value of the two $D_s^{*\pm}$ decay mode. This is done because the preselection uses a mass window, which stops close to the peak of the two $D_s^{*\pm}$ mode. This causes problems when making approximations of the background shape and the position and shape of the $B_s^0 \to D_s^{*\pm} D_s^{*\mp}$ decays. The cut in the preselection has been changed for the 2011 data sample.

The peak of the two $D_s^{*\pm}$ Gaussian is set directly from MC. The width is calcu-

lated by adding a smear to the MC consistent with data. The size of the smearing was determined by looking at the difference in the FWHM in the data and MC for the $D_s^{\pm}D_s^{\pm}$ and the $D_s^{\pm}D_s^{*\mp}$ peaks. These were added in quadrature to give the FWHM of the $D_s^{*\pm}D_s^{*\mp}$ in data.

5.9 Fit Results

The fit described in the previous section has been applied to the data and MC, after all the selection cuts have been made. It is important to understand how well the data is described by the fit and to also ensure that the fit returns an accurate measure. This section will show the result of the fit for MC and data. The values that come from this, their errors and the correlation of the variables fitted, will also be discussed.

Figures 5.9.1 and 5.9.2 show, the fitted MC and data plots for each of the reconstructed masses.

5.9.1 MC Fit Results

When looking at the MC plots in figure 5.9.1, the fit model describes the peak from $B_s^0 \rightarrow D_s^{\pm}D_s^{-}$ decay well. The fit is less successful at describing the two other signal cases, where the ability to fit for the case with two $D_s^{*\pm}$ particles is less precise. Extending the B_s^0 mass window allows a more precise measurement.

Figure 5.11 shows the correlation matrix for the fit to MC. From this, the largest correlations are between the Gaussian functions for the one $D_s^{*\pm}$ and the Gaussian

for the two $D_s^{*\pm}$ case. There are strong correlations between the number of signal events in the $D_s^{*\pm}$ Gaussian and the width of the Gaussian. There is also a strong correlation between the number of signal events in the two $D_s^{*\pm}$and the mean of the Gaussian for the one $D_s^{*\pm}$. These arise because it is hard to separate the two variables in the fit.

Table 5.4 shows the values of all of the variables with their errors, from the fit to the MC. It shows that there is only a very small contribution to the background in the MC. This suggests that a larger sample needs to be used to model accurately the contribution. The $D_s^{\pm}$ plots have a good description of the events.

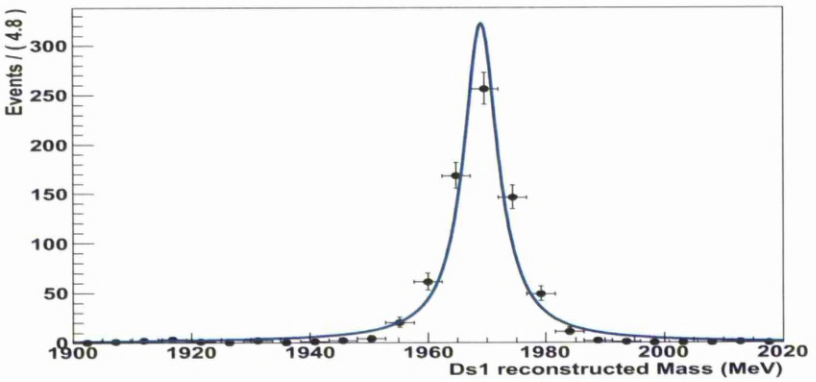

(a) Reconstructed D_s^+ mass peak from MC

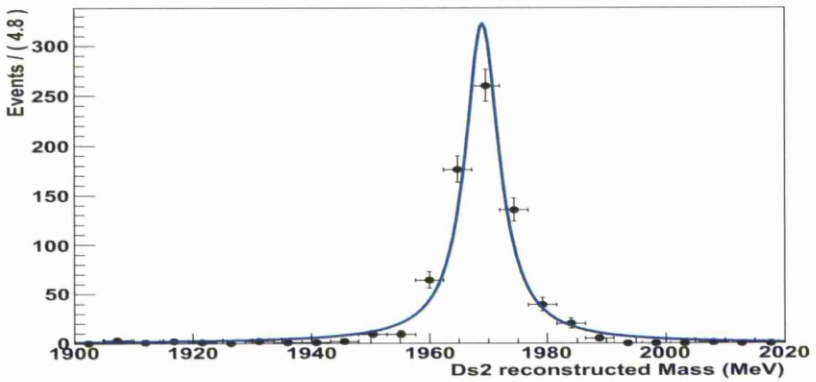

(b) Reconstructed D_s^- mass peak from MC

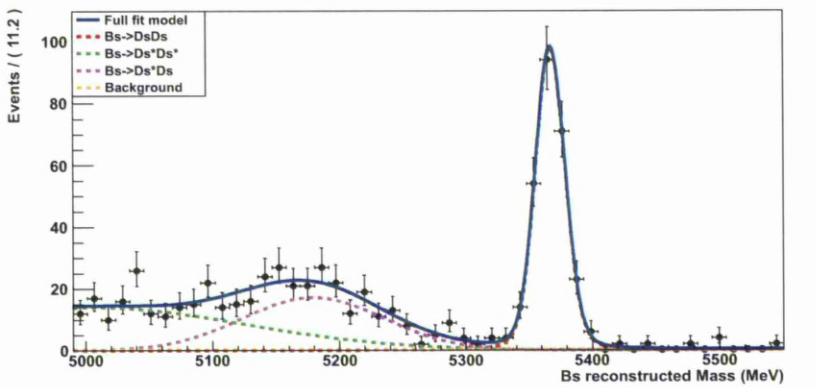

(c) Reconstructed $D_s^\pm$ mass peak from MC

Figure 5.10: Reconstructed B_s^0 and $D_s^\pm$ mass for MC.

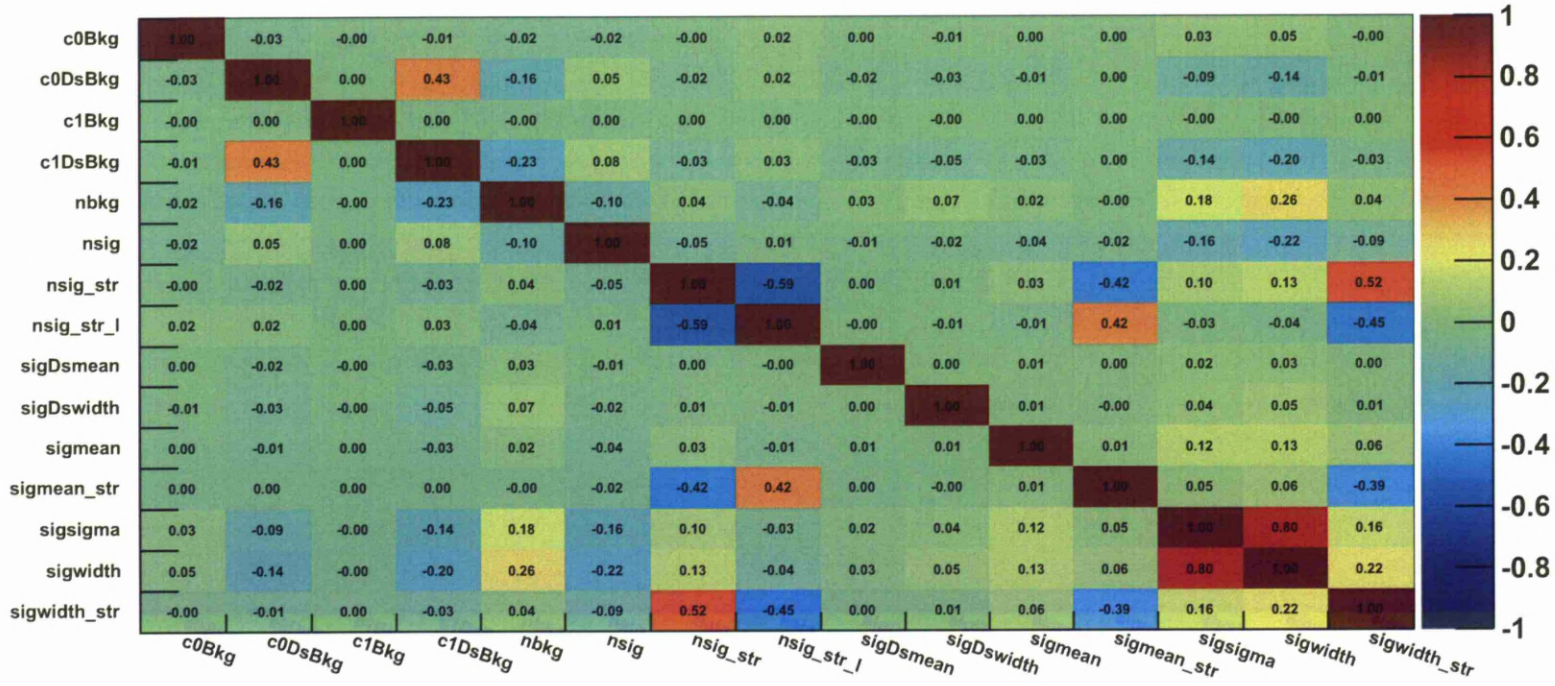

Figure 5.11: The correlation matrix for the fit to MC. The variables are described in table 5.4 along with their values.

Number	Parameter Name	Value	Error	Parameter Description
1	c0Bkg	0.94987	0.123	First Chebychev Parameter for B_s^0 particle
2	c0DsBkg	-0.16311	0.309	First Chebychev Parameter for $D_s^{\pm}$ particle
3	c1Bkg	0.86749	0.00000142	Second Chebychev Parameter for B_s^0 particle
4	c1DsBkg	-0.54929	0.382	Second Chebychev Parameter for $D_s^{\pm}$ particle
5	nbkg	25.872	6.12	Number of background events
6	nsig	309.23	18.4	Number of $B_s^0 \rightarrow D_s^{\pm} D_s^{\pm}$ decays
7	nsig_str	248.04	26.0	Number of $B_s^0 \rightarrow D_s^{\pm} D_s^{*\mp}$ decays
8	nsig_str_1	302.69	26.8	Number of $B_s^0 \rightarrow D_s^{*\pm} D_s^{*\mp}$ decays
9	sigDsmean	1968.9	0.130	Peak of the $D_s^{\pm}$ mass
10	sigDswidth	7.1726	0.235	Width of the $D_s^{\pm}$ mass peak
11	sigmean	5366.9	0.745	Peak from $B_s^0 \rightarrow D_s^{\pm} D_s^{\pm}$
12	sigmean_str	5186.2	5.45	Peak from $B_s^0 \rightarrow D_s^{\pm} D_s^{*\mp}$
13	sigsigma	10.798	1.07	Sigma of peak from $B_s^0 \rightarrow D_s^{\pm} D_s^{-}$
14	sigwidth	3.6004	2.09	Width of the Breit-Wigner from $B_s^0 \rightarrow D_s^{\pm} D_s^{-}$
15	sigwidth_str	50.890	4.96	Sigma of the Gaussian from $B_s^0 \rightarrow D_s^{\pm} D_s^{*\mp}$

Table 5.4: The parameter values for the full fit to MC.

5.9.2 Data Fit Results

Figure 5.9.2 shows the result of the fit to data. There is a larger contribution from background than in the MC. This is to be expected, as only a small fraction of the number of background events are generated. The peak from the decay $B_s^0 \rightarrow D_s^{\pm} D_s^{\mp}$ can be seen. The effect of the $D_s^{*\pm}$ modes can be observed by comparing the number of events of higher and lower mass than the B_s^0. It is difficult, from this amount of data, to conclude much about the shape in the lower part of the mass range. This will be improved by using data with a larger mass range. It will then be possible to model more accurately the low mass fall of the two $D_s^{*\pm}$peak.

Figure 5.13 shows the correlation between the parameters of the fit. There are a larger number of parameters with stronger correlations in the data fit than for the MC. This comes from the smearing of the peaks in the data. The effect of this is to merge the $B_s^0 \rightarrow D_s^{\pm} D_s^{\mp}$ peak with the $B_s^0 \rightarrow D_s^{\pm} D_s^{*\mp}$ peak, which results in additional correlations between some parameters. An example of this can be seen when comparing figures 5.9.1 and 5.9.2. There are strong anti-correlations between the number of $D_s^{\pm} D_s^{\mp}$ events and the width of the Gaussian of the $D_s^{\pm} D_s^{*\mp}$ peak. There is also a strong correlation between the number of $D_s^{*\pm} D_s^{*\mp}$ events and the width of the Gaussian of the $D_s^{\pm} D_s^{*\mp}$ peak. There is also a change from a small anti-correlation in MC, to a strong correlation in data for the parameters describing the width of the Voigtian peak and the number of signal events.

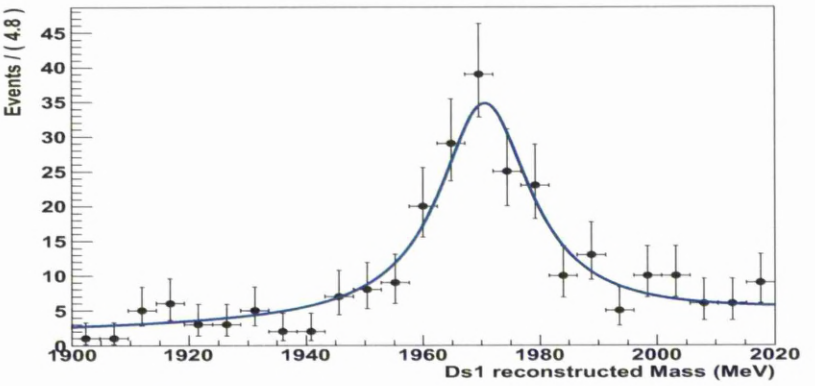

(a) Reconstructed D_s^+ mass peak from MC

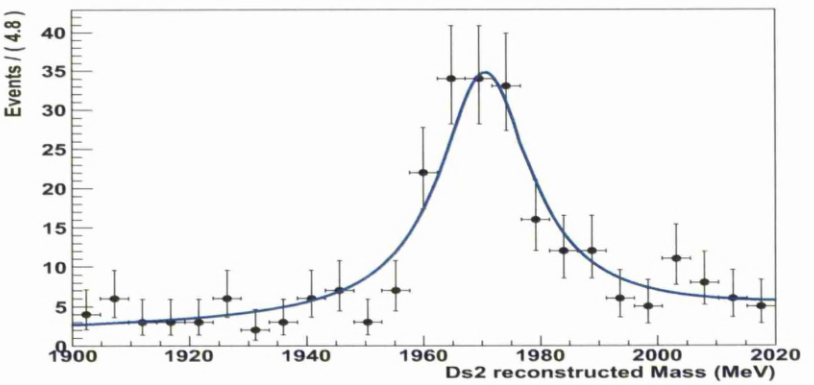

(b) Reconstructed D_s^- mass peak from MC

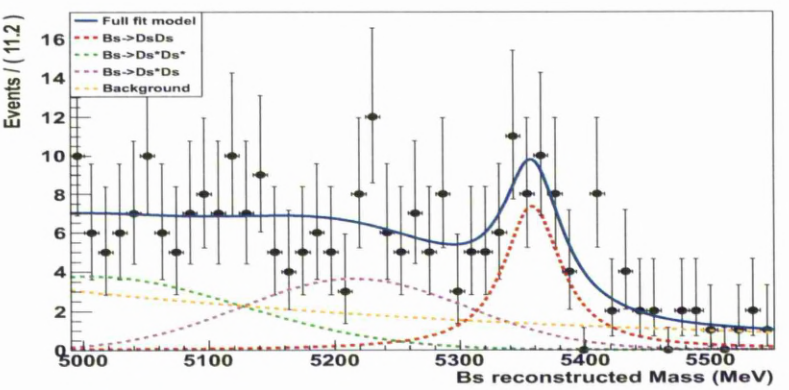

(c) Reconstructed B_s^0 mass peak from MC

Figure 5.12: Reconstructed B_s^0 and $D_s^\pm$ masses for data.

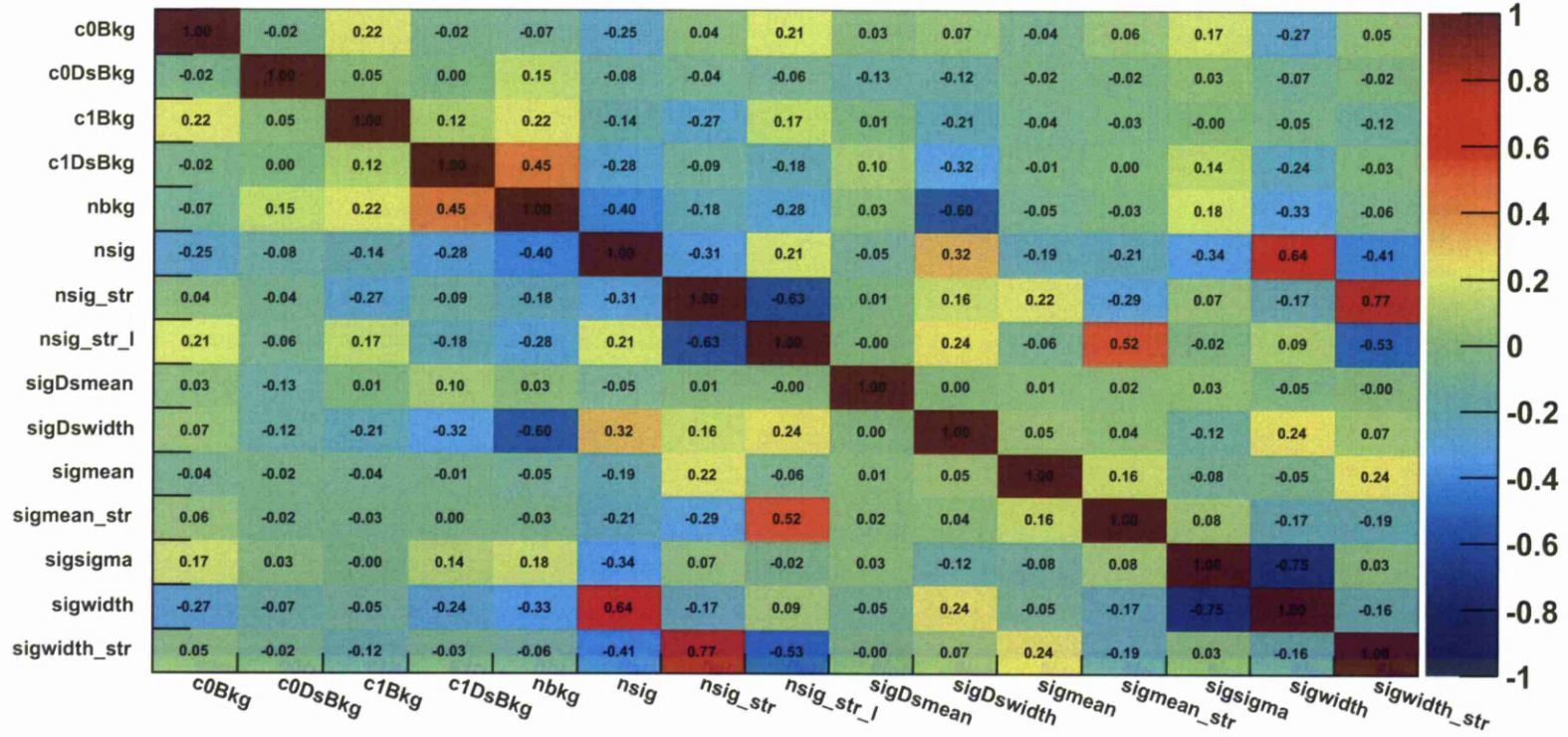

Figure 5.13: The correlation matrix for the fit to data. The variables are described in table 5.9.2 along with their values.

Number	Parameter Name	Value	Error	Parameter Description
1	c0Bkg	-0.51878	0.146	First Chebychev Parameter for B_s^0 particle
2	c0DsBkg	0.31310	0.0989	First Chebychev Parameter for $D_s^{\pm}$ particle
3	c1Bkg	0.0084317	0.147	Second Chebychev Parameter for B_s^0 particle
4	c1DsBkg	-0.093816	0.116	Second Chebychev Parameter for $D_s^{\pm}$ particle
5	nbkg	189.91	0.260	Number of background events
6	nsig	64.028	17.6	Number of $B_s^0 \rightarrow D_s^{\pm} D_s^{\pm}$ decays
7	nsig_str	71.367	27.7	Number of $B_s^0 \rightarrow D_s^{\pm} D_s^{*\mp}$ decays
8	nsig_str_1	69.673	23.9	Number of $B_s^0 \rightarrow D_s^{*\pm} D_s^{*\mp}$ decays
9	sigDsmean	1970.2	0.696	Peak of the $D_s^{\pm}$ mass
10	sigDswidth	18.726	2.36	Width of the $D_s^{\pm}$ mass peak
11	sigmean	5358.4	5.70	Peak from $B_s^0 \rightarrow D_s^{\pm} D_s^{\pm}$
12	sigmean_str	5194.7	24.3	Peak from $B_s^0 \rightarrow D_s^{\pm} D_s^{*\mp}$
13	sigsigma	8.2484	12.8	Sigma of peak from $B_s^0 \rightarrow D_s^{\pm} D_s^{-}$
14	sigwidth	44.595	24.8	Width of the Breit-Wigner from $B_s^0 \rightarrow D_s^{\pm} D_s^{-}$
15	sigwidth_str	74.299	38.3	Sigma of the Gaussian from $B_s^0 \rightarrow D_s^{\pm} D_s^{*\mp}$

Table 5.5: The parameter values for the full fit to data.

5.10 Systematic Errors

This section discusses the methods used to try to understand the systematic errors that are present and the errors have been assigned to measurements.

5.10.1 Validating the Fit

The first method used to validate the fit method was to change the model describing each of the parameters. Several different fit models were chosen for the peaks. Each of these models was then used to provide an understanding of the effect the model had on the number of events used to provide a systematic error. The peak shape for the $D_s^{\pm}D_s^{\mp}$ case and $D_s^{\pm}D_s^{*\mp}$ case was tested with three different models: Breit-Wigner, Voigtian and Gaussian. The $D_s^{*\pm}D_s^{*\mp}$ peak was modelled with a Gaussian, with a fixed peak position and sigma. Two different backgrounds were also considered: an exponential and a polynomial. The results are summarised in table 5.10.1. From this table the extremes of each fit model were taken, which gives systematics in each peak of ± 16, ± 21 and ± 31 events for $D_s^{\pm}D_s^{\pm}$, $D_s^{\pm}D_s^{*\mp}$ and $D_s^{*\pm}D_s^{*\mp}$ respectively.

Fit Models	No.$B_s^0 \to D_s^{\pm} D_s^{\pm}$	No.$B_s^0 \to D_s^{\pm} D_s^{*\mp}$	No.$B_s^0 \to D_s^{*\pm} D_s^{*\mp}$	Background	Log Likelihood
BW,G,G(f),Cb	66.29 ± 16.30	70.57 ± 27.28	69.81 ± 23.83	188.32 ± 25.35	4132.42
BW,G,G(f),E	67.09 ± 16.78	74.16 ± 27.49	68.90 ± 24.22	184.88 ± 24.27	4132.47
BW,V,G(f),Cb	62.91 ± 14.42	61.53 ± 16.48	82.07 ± 20.10	188.50 ± 25.77	4133.60
BW,V,G(f),E	64.78 ± 14.34	64.64 ± 16.12	81.68 ± 20.10	183.94 ± 24.81	4133.81
V,G,G(f),Cb	64.01 ± 17.62	71.48 ± 27.84	69.64 ± 24.00	189.90 ± 25.99	4132.37
V,G,G(f),E	64.64 ± 17.95	74.90 ± 28.11	68.50 ± 24.43	186.89 ± 24.87	4132.41
V,V,G(f),Cb	58.39 ± 15.55	62.80 ± 16.50	81.97 ± 19.71	191.85 ± 26.28	4133.44
V,V,G(f),E	60.21 ± 15.71	65.90 ± 16.14	81.80 ± 19.75	187.05 ± 25.42	4133.65
G,G,G(f),Cb	53.93 ± 17.47	82.44 ± 35.40	68.48 ± 26.89	190.11 ± 25.35	4133.87
G,G,G(f),E	54.02 ± 17.29	82.89 ± 34.52	68.20 ± 26.89	189.93 ± 23.72	4133.84
G,V,G(f),Cb	51.29 ± 15.07	67.94 ± 16.25	83.69 ± 19.41	192.08 ± 28.47	4134.71
G,V,G(f),E	53.61 ± 13.07	70.32 ± 15.76	83.51 ± 19.44	187.62 ± 25.37	4134.81

Table 5.6: The number of events for each decay type using different fit models is shown. The first column describes the fit model used. The parameters relate to the following decays; $D_s^{\pm} D_s^{-}$, $D_s^{\pm} D_s^{*\mp}$, $D_s^{*\pm} D_s^{*\mp}$ and background. Where the notation in the first column is: BW is a Breit-Wigner function, G is a Gaussian function, G(f) is a Gaussian function with a fixed width, V is a Voigtian function and Cb is a Chebychev polynomial and E is an exponential.

Voigtian function was chosen for the B_s^0 to $D_s^+ D_s^-$ peak. The other two peaks from the $D_s^{*\pm}$ were chosen to be modelled by Gaussian functions, while the background uses an Chebychev polynomial.

In order to validate the fit and to check for biases, a toy Monte Carlo was run. By using a toy Monte Carlo, it is possible to understand the stability of the fit and any biases introduced in the definition of parameters. This was done using the RooFit package and by generating 300 toy Monte Carlo samples, containing 300 signal and background events. The proportions of the $D_s^{\pm}$ and $D_s^{*\pm}$ were taken from data fits.

The plots in figure 5.14 come from the number of events found in the Voigtian peak. The pull parameter is small and with the error not far enough from zero to need any adjustments to the value. The error seems to be stable around 8 events. The number of events has a range of about 30 events from the central value.

The plots in figure 5.15 are from the number of events found in the Gaussian peak that represents the $B_s^0 \to D_s^{*\pm} D_s^{\mp}$ decay. The pull of the distribution is small and close to zero. There is a larger error on the number of events and also a larger range of values in the plot of the number of events.

Figure 5.16 comes from the part of the fit used to describe the $B_s^0 \to D_s^{*+} D_s^{*-}$ decays and uses a Gaussian function. This function has a fixed width and peak position. The value of the peak was taken from MC and the width, and has been scaled to account for the detector smearing. The smearing was taken to be the absolute smearing associated with the single $D_s^{*\pm}$ peak added in quadrature, with the absolute smearing from the $D_s^+ D_s^-$ peak.

5.10.2 Variation of Selection

By varying the selection by a small amount and by looking at how this effects the results compared to MC, it is possible to understand the reliability of assumptions made by using cuts on particular variables. This has been done by varying all cuts at once by 10 %, making them loser or tighter by this amount and by looking at how this affects the data and the MC. This gives a conservative estimate of the errors in the MC, the results of which have been summarised in tables 5.7, 5.8, 5.9 and 5.10, where a scaling of 1.1 corresponds to the loosening of cuts by ~10% and 0.9 tightening by ~10%. The errors on the number of events comes from the fit. The errors on the MC come from the square root of the number of MC events.

Cuts	No. Bs DsDs	MC Line Eff	Scaled No Bs DsDs
Cuts 1	64 ±18	0.70 ± 0.04	91± 26
Cuts 1 Scaled(0.9)	51±13	0.61 ± 0.04	84± 22
Cuts 1 Scaled(1.1)	65±16.30	0.70 ± 0.04	94± 24

Table 5.7: This table shows the number of reconstructed $B_s \rightarrow D_s D_s$ particles found using the cuts given in table 5.2, when these have all been adjusted by 10%. The number of events has also been scaled with the MC efficiency for easy comparison.

Cuts	No. Bs Ds*Ds	MC Line Eff	Scaled No Bs Ds*Ds
Cuts 1	71± 28	0.61 ± 0.03	111 ± 44
Cuts 1 Scaled(0.9)	63± 28	0.57 ± 0.03	109 ± 49
Cuts 1 Scaled(1.1)	90± 26	0.64 ± 0.04	141 ± 41

Table 5.8: This table shows the number of reconstructed $B_s \rightarrow D_s^* D_s$ particles found using the cuts given in table 5.2, when these have all been adjusted by 10%. The number of events has also been scaled with the MC efficiency for easy comparison.

All types of signal and background events give results which are within the errors of the fit. By considering the range of the values from the loose and tight cuts, a systematic error is estimated for each of the three signal decays.

Cuts	No. Bs Ds*Ds*	MC Line Eff	Scaled No Bs Ds*Ds*
Cuts 1	139± 48	0.71 ± 0.04	194 ± 67
Cuts 1 Scaled(0.9)	64± 31	0.44 ± 0.03	145 ± 70
Cuts 1 Scaled(1.1)	146± 42	0.73 ± 0.04	200 ± 58

Table 5.9: This table shows the number of reconstructed $B_s \rightarrow D_s^* D_s^*$ particles found using the cuts given in table 5.2, when these have all been adjusted by 10%. The number of events has also been scaled with the MC efficiency for easy comparison.

Cuts	No. Background	MC Line Eff	Scaled No Background
Cuts 1	190 ± 26	0.09± 0.034	2111± 292
Cuts 1 Scaled(0.9)	141± 19	0.08± 0.033	1763± 237
Cuts 1 Scaled(1.1)	293± 22.85	0.1 ± 0.035	2990± 235

Table 5.10: This table shows the number of reconstructed background events found using the cuts given in table 5.2, when these have all been adjusted by 10%. The number of events has also been scaled with the MC efficiency for easy comparison.

Table 5.7 gives a range of ~10 events for $B_s \rightarrow D_s D_s$ decays, corresponding to an error of ~10%. For $B_s \rightarrow D_s^* D_s$ decays, table 5.8 has a range of 30 events which need to be added to the final yield. $B_s \rightarrow D_s^* D_s$ decays give an error of 40, as seen in table 5.9. Each of these values is then scaled back, to using the efficiency of the MC to give the value of the systematic error added. The background is shown in table 5.10. When returned to the number of events seen, this gives an error of 40 events in the background.

5.11 Error Summary

Using the methods described in section (5.10.2) systematic errors have been assigned to the values obtained from the fit. These errors are combined with the errors for the Luminosity, branching ration, fraction of b quarks which become

Variable	Value	Statistical Error	Systematic Error
Luminosity (L_{int})	36.5	0.04	3.6
Cross-section ($\sigma_{b\bar{b}}$)	292	15	43
b quark fraction (f_b)	0.106	0.003	0.009
Total Branching ratio (BR_{tot})	4.5	0.4	1.0
Reconstruction Efficiency (ϵ_{rec}) D_sD_s ($\times 10^3$)	7.9	0.5	0.8
Reconstruction Efficiency (ϵ_{rec}) $D_s^*D_s$ ($\times 10^3$)	8.6	0.5	0.9
Reconstruction Efficiency (ϵ_{rec}) $D_s^*D_s^*$ ($\times 10^3$)	4.7	0.3	0.5
Reconstruction Efficiency (ϵ_{rec}) $D_s^{(*)}D_s^{(*)}$ ($\times 10^3$)	6.7	0.2	0.7
Generator Efficiency (ϵ_{gen}) ($\times 10^2$)	15	1.0	0.2
$BR(B_s^0 \to D_sD_s)$ ($\times 10^3$)	5.8	1.1	1.3
$BR(B_s^0 \to D_sD_s^*)$ ($\times 10^3$)	18	2	4
$BR(B_s^0 \to D_s^*D_s^*)$ ($\times 10^3$)	20	3	5
$BR(B_s^0 \to D_s^{(*)}D_s^{(*)})$ ($\times 10^3$)	43	4	10
$BR(D_s^- \to K^+K^-\pi^-)$ ($\times 10^3$)	55	2	2

Table 5.11: A summary of the errors contributing to the measurement of yield, branching ratio and $\frac{\Delta\Gamma}{\Gamma}$. The generator efficiency is taken to be the same for each of the decay modes.[14, 62]

B_s^0 particles, the cross section of $b\bar{b}$ decays at LHCb and the total efficiency for the generation and reconstruction of the decay. This gives the final errors in section 5.12. These errors are summarised in table 5.11.

5.12 Branching Fraction

The expected signal yield will be evaluated, as will how this relates to the observed result. Equation 5.8 shows how the signal yield has been calculated.

$$N = L_{int} \cdot \sigma_{b\bar{b}} \cdot 2 \cdot f_b \cdot BR_{tot} \cdot \epsilon_{tot} \tag{5.8}$$

L_{tot} is the integrated luminosity recorded by LHCb; $\sigma_{b\bar{b}}$ is the estimated cross-section for $b\bar{b}$ production at LHCb; the factor of 2 comes from the total number of

b type quarks produced; f_b is the fraction of b's which become a B_s^0, taken from LEP measurements and BR_{tot} is the branching fraction of $B_s \rightarrow D_s^+(K^+K^-\pi^+)D_s^-(K^+K^-\pi^-)$, which is calculated using equation 5.9. The values for all these parameters can be found in 5.11.

$$BR_{tot} = BR(B_s^0 \rightarrow D_s^+ D_s^-) \times BR(D_s^- \rightarrow K^+K^-\pi^-) \times BR(D_s^+ \rightarrow K^+K^-\pi^+) \quad (5.9)$$

The values for each of the different decay modes are shown in table 5.11. ϵ_{tot} is the total efficiency of the decay generation and reconstruction, which is calculated from equation 5.10.

$$\epsilon_{tot} = \epsilon_{gen} \times \epsilon_{rec} \quad (5.10)$$

ϵ_{gen}(=0.15) is the efficiency from the generation of the process and ϵ_{rec}(=0.007) is the efficiency for simulated events to pass the reconstruction and full selection. Both of these have a small statistical error and are given an error of 10% to account for the systematics.

Combining the efficiencies and equation 5.8, the yields can be predicted and then measured. This has been done for each of the decay modes and can be seen in table 5.12. The errors for the observed numbers come from the fit and the systematic error discussed earlier. This shows that, within the errors, the predicted and observed yields agree for D_sD_s, $D_s^*D_s$ and $D_s^{(*)}D_s^{(*)}$. In the case of $D_s^*D_s$ there is a slight disagreement but given the errors it is not possible to apply any significance to this. Some of this discrepancy could be explained by the way events are shared between the two peaks. To remove this problem it would be useful to have a larger range for the mass. As was previously mentioned, this line has been modified for 2011 data, so will allow a better description of the $D_s^*D_s^*$ peak.

Decay	Expected number of events	Observed number of events
D_sD_s	$52 \pm 12(stat) \pm 18(syst)$	$64 \pm 18(stat) \pm 17(syst)$
$D_s^*D_s$	$177 \pm 30(stat) \pm 62(syst)$	$71 \pm 28\ (stat) \pm 26(syst)$
$D_s^*D_s^*$	$107 \pm 22(stat) \pm 40(syst)$	$139 \pm 48\ (stat) \pm 43(syst)$
$D_s^{(*)}D_s^{(*)}$	$337 \pm 39(stat) \pm 76(syst)$	$275 \pm 58(stat) \pm 53(syst)$

Table 5.12: The expected yields for each of the different decay types quoted with their errors. The expected number uses LHCb efficiencies and luminosities with branching ratios from other experiments to predict a particle yield. The observed number is the number of each event type from the fit.

5.13 Branching Ratio

The branching ratio can also be measured using equation 5.11 with the values specified earlier.

$$BR(B_s \rightarrow D_sD_s) = \frac{N}{L_{int}\sigma_{b\bar{b}}2f_bBR(D_s \rightarrow KK\pi)BR(D_s \rightarrow KK\pi)\epsilon_{tot}} \tag{5.11}$$

Table 5.13 shows the branching ratios for each of the decays as for the yield. Again for $D_s^*D_s$, the number is lower than expected, most likely because of the reasons given earlier. When comparing table 5.13 and 5.12 it should be noted that table 5.12 includes errors on the values relevant to LHCb in the "expected number of events" and the "observed number of events" is the result of the fit to data. Table 5.13 shows the values obtained for the branching ration from previous experiments and compares these to values found at LHCb. The percentage errors on the values in table 5.13 increase in comparison to table 5.12. The difference in the calculation of the branching ratio and the yield comes from using the values from the fit for N and separating the branching ratio into parts so that the branching ratio for $B_s^0$to $D_s^{\pm}D_s^{\pm}$ can be found. The increase in the errors comes from the larger error on the values of N than there is on the value of the different branching ratios

taken from table 5.11.

Decay	BR previous measurements($\times 10^{-3}$)	Observed BR($\times 10^{-3}$)
D_sD_s	$5.8 \pm 1.1(stat) \pm 1.3(syst)$	$7.8 \pm 2.3(stat) \pm 3.2(syst)$
$D_s^*D_s$	$18 \pm 3(stat) \pm 4(syst)$	$7.9 \pm 3.2(stat) \pm 4.7(syst)$
$D_s^*D_s^*$	$20 \pm 3(stat) \pm 5(syst)$	$28 \pm 14(stat) \pm 15(syst)$
$D_s^{(*)}D_s^{(*)}$	$43 \pm 4(stat) \pm 10(syst)$	$39 \pm 12(stat) \pm 17(syst)$

Table 5.13: Shows the expected branching ratios for each of the different decay types quoted with their errors. The previous measurements come from [3] and the observed are those calculated from the fit to data.

5.14 $\Delta\Gamma_s/\Gamma_s$

Finally, using equation 5.12, $\Delta\Gamma_s/\Gamma_s$ has been calculated for the $D_s^{(*)}D_s^{(*)}$.

$$\frac{\Delta\Gamma_s}{\Gamma_s} \simeq \frac{2BR(B_s \rightarrow D_s^{(*)+}D_s^{(*)-})}{1 - BR(B_s \rightarrow D_s^{(*)+}D_s^{(*)-})} \tag{5.12}$$

$BR(B_s \rightarrow D_s^{(*)+}D_s^{(*)-})$ is the branching fraction for all three of the decay modes and is given in table 5.13. This result is in agreement with previous results summarised in table 5.14.

Experiment	$\Delta\Gamma_s/\Gamma_s \times 10^{-2}$
Dø	7.2 ± 3.0
CDF	12^{+9}_{-10}
Belle	$14.7^{3.6}_{-3.0}(stat.)^{+4.4}_{-4.2}(syst.)$
LHCb 2010 Data	8.1±2.5(stat.)±3.4(syst.)

Table 5.14: Summary of $\Delta\Gamma_s/\Gamma_s$ results from previous experiments.

5.15 Conclusion

This chapter has considered the decay of the B_s^0 meson to $D_s^{\pm}D_s^{\pm}$. Previous results have also been discussed and compared with those obtained from LHCb. The selections used to give a good signal and how this was then fitted have been discussed, as well as several methods used to validate the fit and provide systematic errors on the values obtained. This has led to measurements of the signal yield (see table 5.12) and branching ratio (see table 5.13), which are generally in agreement with recent results. The only difference comes from the $D_s^*D_s$ decay mode, where there is a strong anti-correlation with the $D_s^*D_s^*$ mode which needs to be further considered. The fit also has difficulty constraining the shape from the $D_s^*D_s^*$ decay mode, as half of the signal is lost due to the stripping line used. This stripping line has been updated for 2011 data and will be used when reprocessing the data. Another option would be to use an additional stripping line to give information on the background shape. One such option is the B2twobody line, which has wider mass windows, though this would require additional measurement of the efficiencies of the new line.

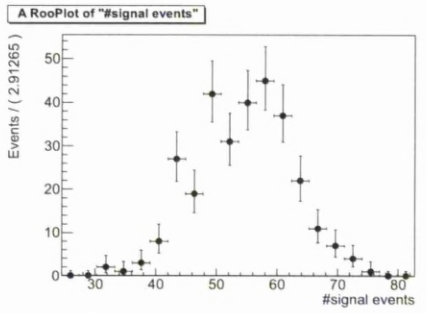

(a) Number of $B_s^0 \to D_s^{\pm} D_s^{\mp}$ events.

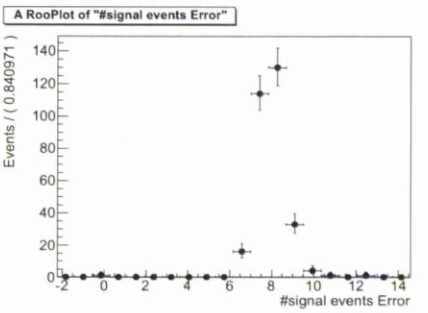

(b) Error on the number of $B_s^0 \to D_s^{\pm} D_s^{\mp}$ events.

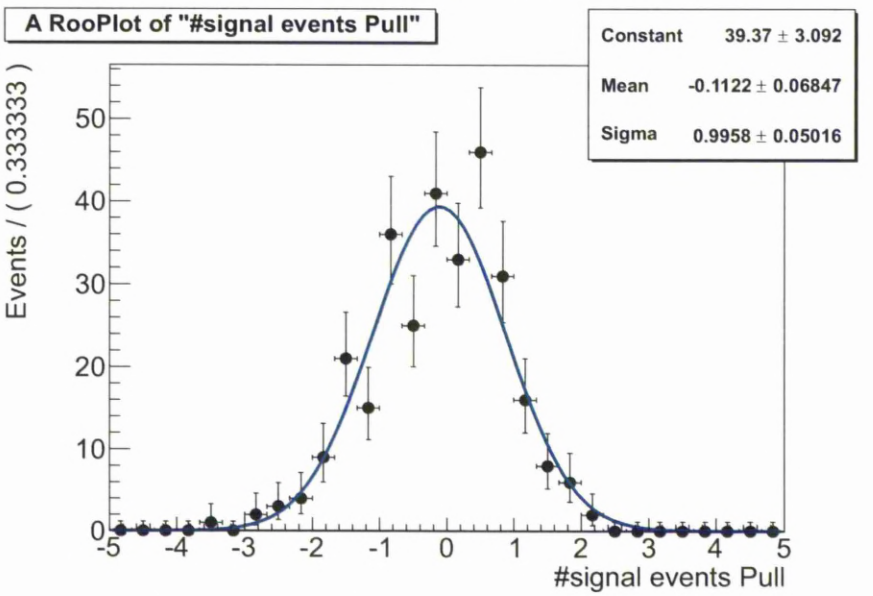

(c) Pull distribution from the number of $B_s^0 \to D_s^{\pm} D_s^{\mp}$ events.

Figure 5.14: a) The number of events. b) The error on the number of events. c) The pull for the number of events. These all come from $B_s^0 \to D_s^{\pm} D_s^{\mp}$ events.

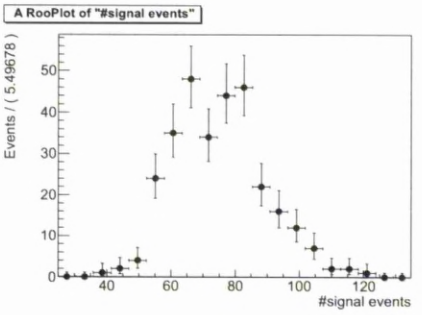

(a) Number of $B_s^0 \to D_s^{*\pm} D_s^{\mp}$ events.

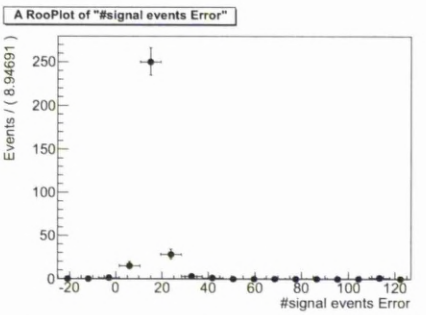

(b) Error on the number of $B_s^0 \to D_s^{*\pm} D_s^{\mp}$ events.

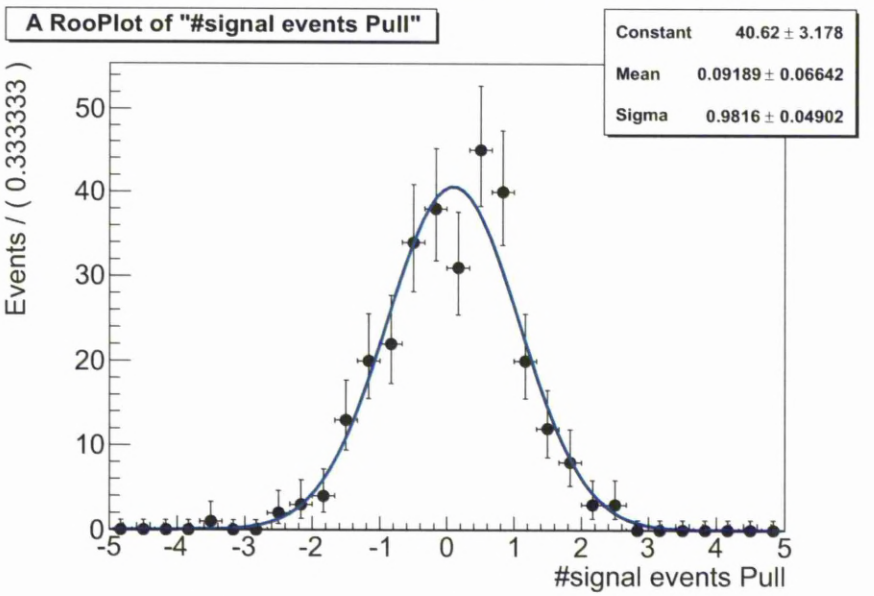

(c) Pull distribution from the number of $B_s^0 \to D_s^{*\pm} D_s^{\mp}$ events.

Figure 5.15: a) The number of events. b) The error on the number of events. c) The pull for the number of events. These all come from $B_s^0 \to D_s^{*\pm} D_s^{\mp}$ events.

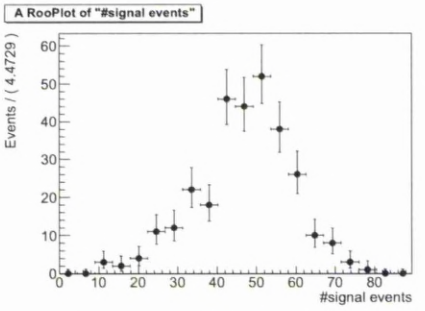

(a) Number of $B_s^0 \to D_s^{*\pm} D_s^{*\mp}$ events.

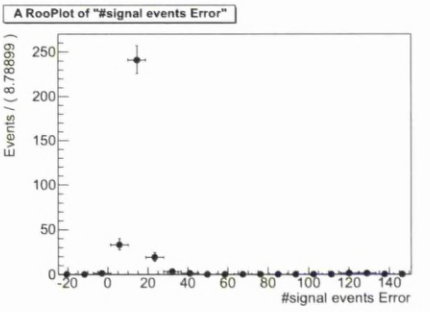

(b) Error on the number of $B_s^0 \to D_s^{*\pm} D_s^{*\mp}$ events.

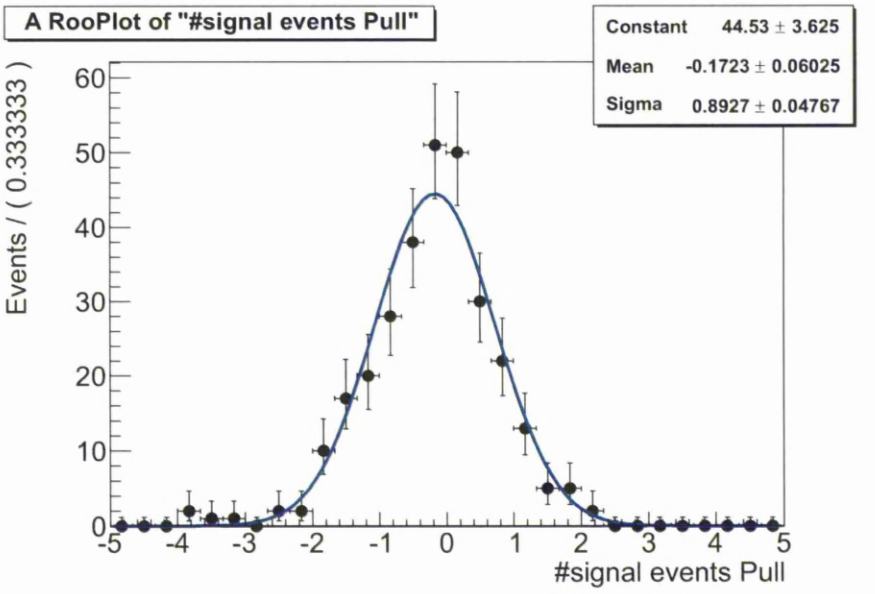

(c) Pull distribution from the number of $B_s^0 \to D_s^{*\pm} D_s^{*\mp}$ events.

Figure 5.16: a) The number of events. b) The error on the number of events. c) The pull for the number of events. These all come from $B_s^0 \to D_s^{*\pm} D_s^{*\mp}$ events.

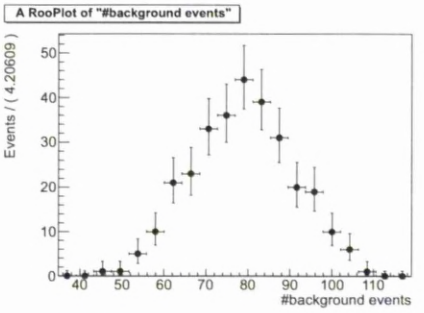

(a) Number of background events.

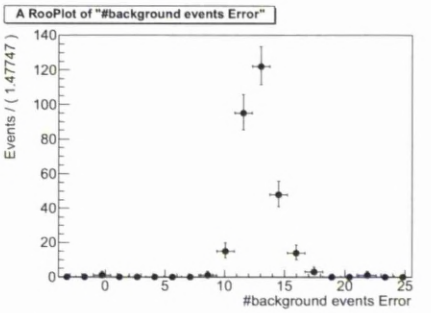

(b) Error on the number of background events.

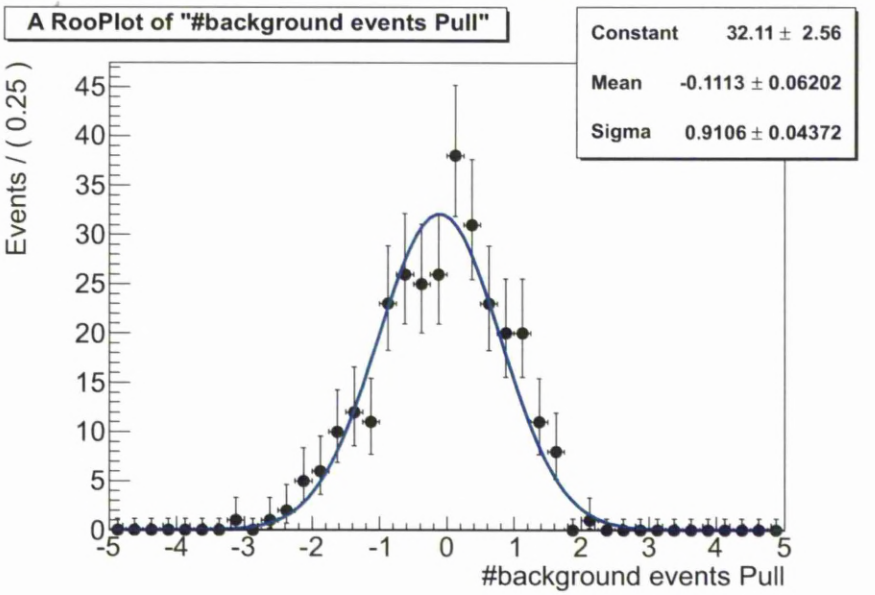

(c) Pull distribution from the number of background events.

Figure 5.17: a) The number of events. b) The error on the number of events. c) The pull for the number of events. These all come from background events.

Chapter 6

Summary

This thesis has used data taken at the LHC during 2010 to examine the performance of the vertex detector(VELO) of LHCb and to make an initial study of the decay of B_s^0 meson to $D_s^{\pm}D_s^{\pm}$.

In chapter 4, the VELO detector has been discussed and a comparison of different simulation and operational performance during 2010 has been made. From examination of the energy deposition, simulation has been shown to have greater agreement with experimental results from Gauss v25r9 to v35r0. There has been improvement for all particle types examined, though there is still some work required for the electron.

A comparison of the MPV and FWHM for MC and data has been shown for all the VELO sensors. This was shown to be in agreement at the level of ~5% with MC2010. Some of the reasons for discrepancies have been explained by known deficiencies in the simulation, which have been addressed for MC2011. The VELO has given consistent performance for all sensors and the shape of the

MPV and FWHM with sensor numbers has shown variations due to the type of clusters present.

The MPV has been shown to change when looking at one and two strip clusters. These changes have been compared with the simulation. This has shown that there are differences between MC and data, though these differences are small and come largely from the description of capacitance in the simulation. The changes in the R sensor are at the right level but show none of the fluctuations that the data do. The Phi sensors again show variations at the correct scale but fail to describe the effects of the routing line in the Phi sensors. All these effects are at a small level and do not represent significant deficiencies with the simulation.

The signal-to-noise has been measured in the R and Phi sensors, looking at one strip clusters. The results for each of the different regions confirm the previously measured effect, caused by the larger noise in the phi strips with routing lines. This is another parameter which needs to be further considered for the running of the detector, because signal decreases with radiation damage and noise also increases with radiation damage.

Chapter 5 considered the decay of the B_s^0 meson to $D_s^{\pm}D_s^{\pm}$ and previous results have been discussed and compared with those obtained from LHCb. The selections used have been discussed and shown to give a good signal. The fitting procedure has been discussed, including several methods used to validate the fit and provide systematic errors on the values obtained. This has led to measurements of the signal yield(see table 5.12) and branching ratio(see table 5.13), which are generally in agreement with recent results. The main discrepancy for the branching ratio and yields comes from the fit to the $D_s^*D_s$ decay mode and is related to the strong anti-correlation with the $D_s^*D_s^*$.

This chapter also gives a result for $\Delta\Gamma_s/\Gamma_s$, which is compared with current results in table 5.14 and is in agreement with these measurements. This measurement combines the different D_s^* decay types, so there is not the same observed discrepancy as in the branching ratios.

All the measurements in chapter 5 by be improved with the large amounts of data collected over 2011 and by improvements made to the stripping lines. At that point, understanding the systematics in the system will become of greater importance.

Bibliography

[1] Lisa Dwyer. *Testbeam studies on the LHCb Vertex Locator modules and a measurement of the mass of the reconstructed B_s meson.* PhD thesis, University of Liverpool, 2009.

[2] Aras Papadelis, MHM Merk, and E Jans. *Characterisation and commissioning of the LHCb VELO detector. oai:cds.cern.ch:1186697.* PhD thesis, Amsterdam, VU University, Amsterdam, 2009. Presented on 17 Jun 2009.

[3] K. Nakamura. Review of particle physics. *J. Phys.*, G37:075021, 2010.

[4] A. Augusto Alves et al. The LHCb Detector at the LHC. *JINST*, 3:S08005, 2008.

[5] Steven Weinberg. Mixing angle in renormalizable theories of weak and electromagnetic interactions. *Phys. Rev. D*, 5:1962–1967, Apr 1972.

[6] G. Arnison et al. Experimental observation of isolated large transverse energy electrons with associated missing energy at s**(1/2) = 540-GeV. *Phys. Lett.*, B122:103–116, 1983.

[7] G. Arnison et al. Experimental observation of lepton pairs of invariant mass around 95-GeV/c**2 at the CERN SPS collider. *Phys. Lett.*, B126:398–410, 1983.

[8] M. Banner et al. Observation of single isolated electrons of high transverse momentum in events with missing transverse energy at the CERN anti-p p collider. *Phys. Lett.*, B122:476–485, 1983.

[9] P. Bagnaia et al. Evidence for Z0 –¿ e+ e- at the CERN anti-p p collider. *Phys. Lett.*, B129:130–140, 1983.

[10] K. Abe et al. Observation of large CP violation in the neutral B meson system. *Phys.Rev.Lett.*, 87:091802, 2001.

[11] Bernard Aubert et al. Observation of CP violation in the B^0 meson system. *Phys.Rev.Lett.*, 87:091801, 2001.

[12] (ed.) Evans, Lyndon and (ed.) Bryant, Philip. LHC Machine. *JINST*, 3:S08001, 2008.

[13] Torbjorn Sjostrand, Leif Lonnblad, and Stephen Mrenna. PYTHIA 6.2: Physics and manual. 2001.

[14] M. Calvi et al. Measurements of B^0 mesons production cross-section in pp collisions at $\sqrt{s}$ = 7 TeV using $B^0 \to D^{*-}\mu^+\nu_\mu X$ decays. Oct 2010.

[15] D.J. Lange. The EvtGen particle decay simulation package. *Nucl.Instrum.Meth.*, A462:152–155, 2001.

[16] M. Agari et al. Test beam results of multi-geometry prototype sensors for the lhcb inner tracker. Technical Report LHCb-2002-058, CERN, Geneva, Nov 2002.

[17] J Gassner, F Lehner, and S Steiner. *The mechanical Design of the LHCb Silicon Trigger Tracker*. Number LHCb-2004-110. CERN-LHCb-2004-110. CERN, Geneva, Aug 2010.

[18] Barbosa-Marinho et al. *LHCb outer tracker: Technical Design Report.* Technical Design Report LHCb. CERN, Geneva, 2001.

[19] A Perieanu. Identification of ghost tracks using neural networks. Technical Report LHCb-2007-158. CERN-LHCb-2007-158, CERN, Geneva, Jan 2008.

[20] M Krasowski, M Kucharczyk, W Mnner, G Polok, and M Witek. Primary vertex reconstruction. Technical Report LHCb-2007-011. CERN-LHCb-2007-011, CERN, Geneva, Sep 2007.

[21] *Aproved plots for Velo colaberation.* https://lbtwiki.cern.ch/bin/view/VELO/VELOConferencePlots.

[22] A. Arefev et al. Beam test results of the lhcb electromagnetic calorimeter. Technical Report LHCb-2007-149. CERN-LHCb-2007-149, CERN, Geneva, May 2008. revised version submitted on 2008-05-15 09:09:53.

[23] C Coca, T Preda, A Rosca, I Ajinenko, A E Dorokhov, R I Dzhelyadin, A K Konoplyannikov, V Matveev, V Novikov, O P Yushchenko, and Y Ranyuk. The hadron calorimeter prototype beam-test results. Technical Report LHCb-2000-036, CERN, Geneva, Oct 2000.

[24] R W Forty and O Schneider. Rich pattern recognition. Technical Report LHCb-98-040, CERN, Geneva, Apr 1998.

[25] R Muresan. Cherenkov ring reconstruction methods. Technical Report LHCb-2007-121. CERN-LHCb-2007-121, CERN, Geneva, Sep 2007.

[26] L. J. R. Aitchison and A. J. G. Hey. *Gauge theories in particle physics. Volume 1: From Relativistic Quantum Mechanics to QED.* Number ISBN 0-7503-0864-8. 2003.

[27] L. J. R. Aitchison and A. J. G. Hey. *Gauge theories in particle physics. Volume 2: QCD and Electroweak Theory.* Number ISBN 0-7503-0950-4. 2004.

[28] Antonio Pich. The Standard model of electroweak interactions. 2007.

[29] *Quantum Field Theory.* John Wiley & Sons, 2006.

[30] R. Arnold, C. Augier, A.M. Bakalyarov, J. Baker, A. Barabash, et al. Technical design and performance of the NEMO 3 detector. *Nucl.Instrum.Meth.*, A536:79–122, 2005.

[31] J. Goldstone. Field Theories with Superconductor Solutions. *Nuovo Cim.*, 19:154–164, 1961.

[32] J.H. Christenson, J.W. Cronin, V.L. Fitch, and R. Turlay. Evidence for the 2π Decay of the K_2^0 Meson. *Phys.Rev.Lett.*, 13:138–140, 1964.

[33] J.H. Christenson, J.W. Cronin, V.L. Fitch, and R. Turlay. Evidence for the 2 pi Decay of the k(2)0 Meson. *Phys.Rev.Lett.*, 13:138–140, 1964.

[34] A. Abashian et al. Measurement of the CP violation parameter $\sin 2\phi_1$ in B_d^0 meson decays. *Phys.Rev.Lett.*, 86:2509–2514, 2001.

[35] Bernard Aubert et al. Measurement of CP violating asymmetries in B^0 decays to CP eigenstates. *Phys.Rev.Lett.*, 86:2515–2522, 2001. ¡a href=/slac/media-info/20010212/firstresults.html¿* Press Release *¡/a¿.

[36] Lincoln Wolfenstein. Parametrization of the kobayashi-maskawa matrix. *Phys.Rev.Lett.*, 51:1945, 1983.

[37] R. Aleksan, A. Le Yaouanc, L. Oliver, O. Pene, and J.C. Raynal. Estimation of Delta Gamma for the B(s) - anti-B(s) system: Exclusive decays and the parton model. *Phys.Lett.*, B316:567–577, 1993.

[38] S. Esen, A.J. Schwartz, I. Adachi, H. Aihara, K. Arinstein, et al. Observation of $B_s^0 \to D_s^{(*)+} D_s^{(*)-}$ using e^+e^- collisions and a determination of the $B_s - \overline{B}_s$ width difference $\Delta\Gamma_s$. *Phys.Rev.Lett.*, 105:201802, 2010.

[39] SungWoo Youn. *Measurement of $B(B_s^0 \to D_s^{(*)} D_s^{(*)})$*. PhD thesis, Northwestern University, 2009.

[40] R. Barate et al. A Study of the decay width difference in the $B_s^0 - \overline{B}_s^0$ system using $\phi\phi$ correlations. *Phys.Lett.*, B486:286–299, 2000.

[41] Sevda Esen. Updated Measurement of $\mathcal{B}(B_s \to D_s^{(*)+} D_s^{(*)-})$ and Determination of $\Delta\Gamma_s$. 2011.

[42] V. M. Abazov et al. Evidence for decay $B_s^0 \to D_s^{+(*)} D_s^{-(*)}$ and a measurement of $\Delta\Gamma_s^{CP}/\Gamma_s$. *Phys. Rev. Lett.*, 102:091801, 2009.

[43] T. Aaltonen et al. First Observation of the Decay $B_s^0 \to D_s^- D_s^+$ and Measurement of Its Branching Ratio. *Phys. Rev. Lett.*, 100:021803, 2008.

[44] L. Landau. On the energy loss of fast particles by ionization. *J.Phys.(USSR)*, 8:201–205, 1944.

[45] H. Bichsel. Straggling in thin silicon detectors. *Rev. Mod. Phys.*, 60:663–699, 1988.

[46] *Techniques for Nuclear and Particle Physics Experiments*. Springer, 1994.

[47] A Van Lysebetten, B Verlaat, and M van Beuzekom. Co2 cooling experience (lhcb). *PoS*, Vertex 2007:009, 2007.

[48] S Lchner and M Schmelling. The beetle reference manual - chip version 1.3, 1.4 and 1.5. Technical Report LHCb-2005-105. CERN-LHCb-2005-105, CERN, Geneva, Nov 2006.

[49] A Palacios, A Bates, J Buytaert, J Borel, P Collins, D Eckstein, L Eklund, M Ferro-Luzzi, E Jans, T Ketel, D Petrie, M Pivk, and M Tobin. Pulseshape characteristics of a 300 μm PR03 R-measuring VELO sensor read out with a Beetle 1.3 chip. Technical Report LHCb-2004-068. CERN-LHCb-2004-068, CERN, Geneva, Jan 2005.

[50] G Haefeli, A Bay, A Gong, H Gong, M Mcke, N Neufeld, and O Schneider. The lhcb daq interface board tell1. *Nucl. Instrum. Methods Phys. Res., A*, 560:494–502, 2006.

[51] G Haefeli. *Contribution to the development of the acquisition electronics for the LHCb experiment.* PhD thesis, EPFL Lausanne, Geneva, 2004.

[52] R. Antunes-Nobrega et al. *LHCb computing: Technical Design Report.* Technical Design Report LHCb. CERN, Geneva, 2005. Submitted on 11 May 2005.

[53] S. Agostinelli et al. Geant4–A simulation toolkit. *Nuclear Instruments and Methods in Physics Research Section A: Accelerators, Spectrometers, Detectors and Associated Equipment*, 506(3):250 – 303, 2003.

[54] J.F. Bak, A. Burenkov, J.B.B. Petersen, E. Uggerhoj, S.P. Moller, et al. Large departures from landau distributions for high-energy particles traversing thin Si and Ge targets. *Nucl.Phys.*, B288:681, 1987.

[55] S. Hancock, F. James, J. Movchet, P.G. Rancoita, and L. Van Rossum. Energy loss and energy straggling of protons and pions in the momentum range 0.7-GeV/c to 115-GeV/c. *Phys.Rev.*, A28:615, 1983.

[56] S. Hancock, F. James, J. Movchet, P.G. Rancoita, and L. Van Rossum. Energy loss distributions for single particles and several particles in a thin silicon absorber. *Nucl.Instrum.Meth.*, B1:16, 1984.

[57] *Semiconductor Detector Systems*. Oxford University Press, 2005.

[58] K Rinnert. Talk: News on noise monitoring.

[59] D. Buskulic et al. First measurement of the B_s meson mass. *Phys. Lett.*, B311:425–430, 1993.

[60] A. Abulencia et al. Observation of $B_s^0 - \overline{B_s^0}$ Oscillations. *Phys.Rev.Lett.*, 97:242003, 2006.

[61] Remi Louvot. B_s^0 Decays at Belle. *PoS*, FPCP2010:015, 2010.

[62] E. Barberio et al. Averages of b–hadron and c–hadron properties at the end of 2007. 2008.